Crystal plasticity applied to aggregates under non-symmetric cyclic loadings : Mechanical analysis and model order reduction

Harris Farooq

PSL UNIVERSITÉ PARIS

THÈSE DE DOCTORAT
DE L'UNIVERSITÉ PSL

Préparée à MINES ParisTech

Plasticité cristalline appliquée aux agrégats sous charges cycliques non symétriques: Analyse mécanique et réduction de modèles

Crystal plasticity applied to aggregates under non-symmetric cyclic loadings: Mechanical analysis and model order reduction

Soutenue par
Harris FAROOQ
Le 3 décembre 2019

École doctorale n°621
Ingénierie des Systèmes, Matériaux, Mécanique, Energétique

Spécialité
Mécanique

Composition du jury :

M. Nicolas SAINTIER Professeur, Arts et Métiers ParisTech	*Président*
Mme. Varvara KOUZNETSOVA Professeur, TU Eindhoven, Pays-Bas	*Rapporteur*
M. Franz ROTERS Privatdozent, MPIE, Allemagne	*Rapporteur*
M. David MCDOWELL Professeur, Georgia Tech, Etats-Unis	*Examinateur*
M. David RYCKELYNCK Professeur, Mines ParisTech	*Examinateur*
M. Samuel FOREST Directeur de Recherche, CNRS	*Directeur de thèse*
M. Georges CAILLETAUD Professeur, Mines ParisTech	*Invité*
Mme. Tonya ROSE Ingénieure, Safran-Tech, France	*Invité*

MINES ParisTech | PSL

This thesis is dedicated to my family!

Acknowledgement

My three year stay at the lab has been a wonderful learning experience both at a personal and a professional level. I want to start by thanking my supervisors Professors Georges Cailletaud, Samuel Forest and David Ryckelynck for offering me this PhD. Georges who has been a great mentor and has always been there for discussions and questions no matter how basic. The kind and encouraging attitude he shows towards his students is ever so humbling, and I feel extremely lucky to have been among his last three PhD students. David who has helped me build my numerical skills and has been patient with me throughout my PhD. Samuel who being the thesis director has shown great patience and helped me go though the PhD with ease.
I especially thank the PhD defence jury members Professors David McDowell, Varvara Kouznetsova, Franz Roters, Nicolas Santier, and engineer Tonya Rose for taking time out of their busy schedules, and coming to Paris. Their comments were extremely constructive and let me refine the contents of my work in a much better way.
At the lab, I would like to thank Djamel Missoum-Benziane who has been handling all my mechanics and software related questions and has helped me through all phases of my PhD; without his help it would have been very difficult. I would extend my gratitude to Jean-Michel Scherer who helped me implement an implicit version of the numerical model and understand various fundamental concepts in mechanics. Aron N'Semi-Noah for being there whenever I needed anything. Amar El Ouazaini Tuhami who helped me in general scientific questions. Aurélien Fouque, Clément Bertaux, Juan-Manuel Garcia, Yazid Madi, Eeva Mofakhami, Hugo Launay, Régis Clement, Laurent Aubanel, Vladislav Yastrebov, Ziradjoudine Akber, Anass Assadiki, Halyna Volkova and Youssef Hammadi for being there for social interactions. Nicolas Cliche for making funny jokes all the time. Xiang Kong, Raffaele Russo, Halyna Volkova, Julie Brun, Daniel Irmer, Vikram Phalke, Faisal Islam Simon Schmidt, Mohamed Abatour, Yohan Clement, Alexandre Portal and David Siedel for going to lunch with me. Nikolay Osipov, Stéphane Quilici, Cristian Ovalle Rodas, Basile Marchand, Kais Ammar and Vladislav Yastrebov who have helped me with problems related to Z-set and general mechanics. Grégory

Sainte-Luce for helping me recover my PhD data, which I once accidentally deleted from a non-backed-uped hard-disk. Anne-Françoise Gourgues-Lorenzon, Jacques Besson and Henry Proudhon, for all the scientific discussions. Tonya Rose for her contribution to the implementation of the numerical model as well as editing my research articles. Arjen Roos for being the nice guy he is and being patient with me during my industrial visits. I wish the very best to everyone at Centre des Matériaux.

Jeudi 22 décembre 2019
Paris, France

Résumé en Français

Le domaine de la mécanique, en particulier de la micromécanique, a connu de grands développements. Il est bien connu que l'écoulement plastique dans un monocristal est anisotrope, ce qui peut être modélisé à l'aide de lois de comportement phénoménologiques à l'échelle moyenne. Le développement de lois micromécaniques a pour objectif de relier le comportement de chaque grain, de prédire l'évolution de la plasticité et, à son tour, de rendre compte des propriétés macroscopiques de la structure. Cette thèse a porté sur deux problèmes physiques, à savoir le comportement des matériaux soumis à un chargement asymétrique dans des conditions limites fondées soit sur des contraintes cycliques soit sur des déplacements cycliques. Ces chargements entraînent une accumulation de contrainte supplémentaire ou une relaxation de contrainte moyenne à l'échelle macroscopique. Les modèles numériques conventionnels donnent un excès des deux quantités. Dans ce travail, il est montré qu'une approche par éléments finis de plasticité cristalline de mésoéchelle peut répondre à ces deux problèmes. Différents états mécaniques existant dans des structures chargées cycliquement sont examinés et une interprétation micromécanique est donnée concernant leur comportement macroscopique caractéristique. Les résultats statistiques de différentes quantités constitutives au sein d'un polycristal sont également analysés, ce qui permet de mieux comprendre ce qui se passe au niveau local.
L'autre partie de la thèse concerne le traitement de données volumineuses dans le domaine de la science des matériaux informatique. Tout en résolvant des problèmes d'éléments finis à grande échelle, de grandes quantités de ressources de calcul sont utilisées et souvent les résultats au cours du temps sont ignorés après les études et ne sont utilisés pour les prévisions futures. Dans ce travail, il est montré qu'en utilisant des données déjà générées, de nouveaux cas de test peuvent être prédits à partir de simulations précédentes. La méthode utilisée est appelée hyper-réduction hybride. Elle utilise un protocole d'apprentissage automatique non supervisé associé à la technique gappy POD pour exécuter des simulations aux éléments finis réduits. Ces simulations réduites aident à capturer les valeurs extrêmes de plasticité. Des résultats de fatigue à faible nombre de cycles dans un superalliage à base de fer et de nickel (Inconel 718) sont utilisés comme test.

Abstract

The field of mechanics, particularly micromechanics, has undergone great developments. It is well known that plastic flow in a single crystal is anisotropic which may be modeled using phenomenological constitutive laws at the mesoscale. The idea behind the development of micromechanical laws is to relate the behavior of each individual element of the geometry, predict evolving plasticity, and in turn account for the macroscopic properties of the structure.
Two physical problems have been considered is this thesis i.e. the behavior of materials when they are asymmetrically loaded under cyclic stress or strain based boundary conditions. These loadings cause incremental strain accumulation or mean stress relaxation at the macroscopic scale. Conventional numerical models give an excess of both quantities. In this work it is shown that a mesoscale crystal plasticity finite element approach can give an answer to both problems. Different mechanical states existing in cyclically loaded structures are scrutinized and a micromechanical interpretation is given about their characteristic macroscopic behavior. Statistical results of different constitutive quantities within a polycrystal are also analyzed which give a new insight into what is happening at a local level.
The other part of the thesis pertains to big data problems in computational materials science. While solving large scale finite element problems, vast amounts of computational resources are utilized and many a times the evolving results are discarded after studying; not using them for future predictions. In this work it is shown that by utilizing already generated data, new test cases may be predicted from previous simulations. The method employed is called hybrid hyper-reduction which uses an unsupervised machine learning protocol coupled with the gappy proper orthogonal decomposition technique to run reduced finite element simulations. These reduced simulations help in capturing extreme values of plasticity. Low cycle fatigue in a nickel iron based super alloy (Inconel 718) is taken as a test case.

Notations and abbreviations

In this thesis, vectors are underlined once, second order tensors twice and fourth order tensors four times. For instance "$\underline{A}$" represents a vector, whereas "$\underline{\underline{A}}$" is a second order tensor. The transpose of a tensor is denoted by a superscipt "T" ($\underline{\underline{A}}^T$), whereas the inverse is portrayed by a superscipt of "-1" ($\underline{\underline{A}}^{-1}$). The term ":" denotes the inner product of two tensors, and "$\otimes$" denotes the tensor or dyadic product between tensors. Other notations are defined as needed along the way. The following are some of the abbreviations used:

CPFEM	Crystal plasticity finite element method
RVE, VE	Representative volume element, volume element
POD	Proper orthogonal decomposition
FCC	Face centered cubic
RAM	Random-access memory
LK, HK	Low kinematic, high kinematic
RB	Reduced basis
FOM	Full order model
ROM	Reduced order model
DOFs	Degrees of freedom
PCA	Principal component analysis
DEIM	Discrete empirical interpolation method
HROM	Hyper-reduced order model
RID	Reduced integration domain

Contents

Chapter 1

Introduction

Introduction

Depuis des temps immémoriaux, les matériaux sont développés pour répondre aux besoins de l'humanité. Ces besoins évoluent avec le temps et, aujourd'hui plus que jamais, il est nécessaire de comprendre les mécanismes fondamentaux qui régissent la réponse mécanique des matériaux. Plus important encore, au cours de leur durée de vie, les matériaux d'ingénierie devaient répondre à certains critères de performance. On s'attend à ce que ces matériaux résistent à différents scénarios de charge associés à des conditions thermiques ou mécaniques en service. Par exemple, dans les moteurs d'avion à turbine à gaz, l'efficacité du moteur augmente avec l'augmentation de la température de fonctionnement. Il en résulte une réduction de la consommation de carburant, ce qui réduit les coûts d'exploitation, mais limite le choix des matériaux qui peuvent être utilisés dans le moteur à turbine à gaz. Par conséquent, la réponse mécanique de ces matériaux doit être caractérisée en ce qu'ils peuvent être utilisés efficacement comme matériaux d'ingénierie.

Un autre problème, en particulier dans les moteurs d'avion, est que les différents composants sont soumis à un chargement cyclique qui réduit la durée de vie de ces composants par de nombreux plis. L'un de ces composants est l'aube de turbine, qui est souvent le composant limitant d'un moteur à réaction. En effet, dans un environnement d'ingénierie, ces pales doivent subir plusieurs types de chargements externes dont l'amplitude et la fréquence varient. De plus, comme différentes conditions de charge sont appliquées, c.-à-d. une contrainte ou une déformation

contrôlée, ces composants présentent des réponses mécaniques complètement différentes. Il est important de comprendre les limites auxquelles un matériau peut être soumis, car cela permettra d'obtenir une meilleure estimation de sa durée de vie. Par conséquent, la caractérisation de ces réponses est cruciale pour l'industrie et la communauté scientifique. Ce qui est encore plus important, c'est que dans le matériau, la plasticité se localise aux endroits préférés et que l'identification de ces points critiques est importante pour une meilleure compréhension de la réponse des matériaux hétérogènes. Pour ce faire, une approche numérique a été prise en compte dans ce travail.

Le but de ce travail est d'utiliser une description mathématique du matériau communément appelée modèle de matériau constitutif pour souligner les effets physiques. En d'autres termes, les modèles matériels sont une tentative d'incarner les mécanismes et les comportements fondamentaux des systèmes au moyen d'un ensemble d'équations mathématiques, et ce type d'approche a fait l'objet d'un battage publicitaire important au cours des dernières décennies. Les techniques numériques ont été développées à tel point que des conclusions rationnelles peuvent être tirées de ces modèles. Il faut également comprendre que le concept de modélisation des matériaux n'est pas une idée récente. Certaines des définitions de modélisation utilisées aujourd'hui ont été postulées il y a de nombreuses années, par exemple le critère de Tresca pour la production (Tresca, 1864), encore largement utilisé dans diverses définitions de matériaux, a été proposé pour la première fois au milieu du XVIIIème siècle.

Pour commencer par la modélisation des matériaux, la réponse d'un système peut être mathématiquement caractérisée sous différentes formes. Une des approches est la modélisation empirique, qui est entièrement fondée sur des données expérimentales, de sorte que ces modèles ne sont pas basés sur des données hypothèses et approximations dans le contexte de différents principes physiques. Par contre, les modèles empiriques ne sont applicables que dans la gamme de données dont ils sont issus et sont peu utiles dans le domaine de la déformation plastique des matériaux. Cette approche n'est, en général, valable que lorsque de nouveaux matériaux sont manipulés et que leurs réponses ne sont pas pleinement réalisées.

L'approche phénoménologique est une autre voie pour la modélisation des matériaux. Ces modèles ne tiennent pas explicitement compte des détails d'un matériau, mais émettent plutôt l'hypothèse d'une réponse matérielle au moyen d'un cadre mathématique prédéfini. Ces cadres mathématiques se présenteront sous la forme de paramètres indéterminés et ces paramètres peuvent être uniques pour chaque matériau à une température donnée. Ces modèles phénoménologiques peuvent être

utilisés en association avec des équations directrices en mécanique des milieux continus et, contrairement aux modèles empiriques, les modèles phénoménologiques peuvent donner un aperçu du comportement de déformation d'un matériau. La plasticité ainsi que les différents mécanismes de déformation peuvent être caractérisés comme une variable dans les modèles phénoménologiques et comme les déformations du matériau, l'évolution de ces variables peut être suivie. Des conditions aux limites appropriées ainsi que des équations directrices sont ensuite utilisées dans les modèles phénoménologiques. Les équations déterminantes peuvent être résolues en utilisant des méthodes de discrétisation comme les éléments finis ou la transformée de Fourier rapide. Par conséquent, la réponse prévue peut être comparée aux résultats expérimentaux et le modèle est étalonné en conséquence.

La modélisation des matériaux des chercheurs incorporent plusieurs théories dans leurs modèles, en ce qui concerne le comportement des matériaux. Les trois plus courantes sont les théories de l'élasticité, de (visco)plasticité et de la déformation des dommages. Les théories élastiques s'appliquent généralement aux matériaux qui subissent de petites déformations et reviennent à leur état initial une fois la charge enlevée. Un exemple est la loi de Hookes, qui n'est applicable que dans la région élastique. Les modèles classiques de plasticité intègrent la notion selon laquelle le matériau se déforme d'abord élastiquement, mais commence à se déformer lorsqu'il dépasse sa limite élastique. Un exemple commun pour un modèle de plasticité est Tresca (1864). Une autre approche comprend des modèles d'endommagement qui tiennent compte de la dégradation de la charge appliquée supportable du matériau, et un exemple commun est le modèle de Gurson pour la rupture ductile.

Une autre sous-classification de la modélisation des matériaux est qu'elle peut être divisée en différentes échelles de longueur dont les trois plus communes sont macro, méso et micro. La macro-échelle décrit le comportement général d'un matériau en tant que partie intégrante du matériau dans son ensemble, c'est-à-dire dans le sens d'une structure de laboratoire. La micro-échelle décrit le comportement de base d'un matériau comme les grains, les dislocations, etc. A cette échelle, la description moyenne des matériaux comme à l'échelle macro devient invalide. La méso-échelle est un niveau d'échelle intermédiaire, qui est habituellement décrit par l'approche de la mécanique des milieux continus. Dans ce contexte, microscopique se réfère aux défauts de réseau sous l'échelle du grain, mésoscopique se réfère aux défauts à l'échelle du grain et macroscopique à l'échelle de la géométrie de l'échantillon. Les travaux de cette thèse portent sur des modèles définis au niveau du système de glissement.

1.1 Introduction

Since time immemorial materials are being developed to suit mankind's needs. These needs change with time and today more than ever before there is a need to understand fundamental mechanisms governing the mechanical response of materials. More importantly, during their lifetime, engineering materials are anticipated to meet certain performance benchmarks. These materials are expected to withstand different loading scenarios coupled with thermal or mechanical in-service conditions. For instance, in gas turbine aircraft engines see figure 1.1, the efficiency of the engine increases with an increase in the operation temperature. This causes less fuel to be consumed which lowers operation costs but limits the choice of materials which can be used in the gas turbine engine. Hence, the mechanical response of such materials needs to be characterized so that they can be effectively used as engineering materials.

Figure 1.1: Gas turbine engine (Safran M88-2, manufactured by Safran Aircraft Engines) which has components subjected to complex loadings[1]

Another problem especially in aircraft engines is that various components are subjected to a cyclic load environment which reduces the lifetime of such components by many folds. One such component is the turbine blade as shown in figure 1.2, which is often the limiting component of a jet engine. This is because in an engineering environment, these blades have to go through several types of external loading conditions which vary in amplitude and frequency. Complimenting that, as different loading conditions are applied i.e. stress or strain controlled, these

[1]Picture taken by Matthieu Sontag at Paris Air Show 2007

components exhibit completely different mechanical responses. Understanding the limits to which a material can be put through is important because it will lead to a better lifetime estimation. Hence, the characterization of such responses is crucial for the industry as well as the scientific community. Even more important is the fact that within the material, plasticity localizes at preferred locations and the identification of such hot-spots is important for a better understanding of the response of heterogeneous materials. To cater for this, a numerical approach has been considered in this work.

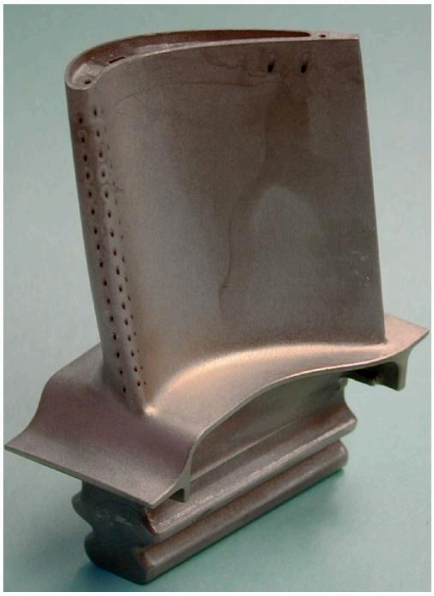

Figure 1.2: High pressure turbine blade which is usually the limiting component of a jet engine

The intent of this work is to use a mathematical description of the material response, commonly known as a constitutive material model (Lemaitre and Chaboche, 1994) to underline physical effects. In other words, material models are an attempt to embody fundamental mechanisms and behaviors of systems through a set of mathematical equations, and this type of an approach has gained significant hype in the last few decades. Numerical techniques have been developed to such an extent that rational conclusions can be derived from such models. It should also be appreciated that the concept of material modeling is not a recent idea. Some of the modeling definitions being used today were postulated many years ago, for example the Tresca criterion for yielding (Tresca, 1864), still widely being used in various material definitions was first proposed in the mid eighteenth century.

To start with material modelling, the response of a system can be mathematically

characterized in various forms. One approach is empirical modeling, which bases its postulations entirely on experimental data such that these models are not based on assumptions and approximations in context to different physical principles. On the downside, empirical models are applicable only within the range of data from which they have been derived, and are of little use in the realm of plastic deformation of materials. This approach is, in general, only valid when new materials are being handled and their responses are not fully realized (Rao and Deshpande, 2014).

A different path for material modeling is the phenomenological approach. These models do not explicitly consider the details of a material but rather hypothesize material response through a predefined mathematical framework. These mathematical frameworks will be in the form of undetermined parameters and these parameters may be unique for every material at a given temperature. These phenomenological models can be used in association with governing equations in continuum mechanics and unlike empirical models, phenomenological models can give insight into the deformation behavior of a material. Plasticity as well as different deformation mechanisms can be characterized as a variable in phenomenological models and as the material deforms, the evolution of these variables can be monitored. Appropriate boundary conditions as well as governing equations are then used in phenomenological models. The governing equations can be solved by using discretization methods like finite elements or fast Fourier transform. As a result, the predicted response may be compared with experimental results and the model is calibrated accordingly (Morgeneyer et al., 2009).

Researchers modeling materials incorporate several theories into their models, regarding material behavior. The three most common are elastic, (visco)plastic and damage deformation theories. Elastic theories are usually applicable for materials which undergo small deformations and return to their original state once the load is removed. An example is the Hookes law, which is only applicable in the elastic region (Slaughter, 2002). Classical plasticity models incorporate the notion that first the material deforms elastically, but starts plastic deformation upon exceeding its yield stress (Besson et al., 2009; Soutis and Beaumont, 2005). A common example for a plasticity model is Tresca (1864). Another approach includes damage models which consider the degradation in the bearable applied load of the material, and a common example is the Gurson model for ductile fracture(Zhang et al., 2000).

Another sub-classification of material modeling is that it can be divided into different length scales of which the three most common are macro, meso and micro. Macro scale describes the general behavior of a material as part of the material

as a whole i.e. in the sense of a laboratory framework. Microscale describes the basic behavior of a material such as grains, dislocations, etc. At this scale, the average material description as in the macro scale becomes invalid. The mesoscale is an intermediate scale level, which is usually described by continuum mechanics approaches (Bull, 2012). In this context, microscopic refers to lattice defect assemblies below the grain scale, mesoscopic refers to defects at the grain scale and macroscopic points to the scale of sample geometry (Raabe, 2004). The work in this thesis pertains to models defined on the slip system level (Rice, 1971; Méric et al., 1991).

1.2 Crystal plasticity finite element method

It is well known that metallic alloys have an inherent substructure which defines their macroscopic properties. Earlier advancements to describe anisotropic crystalline materials did not consider the mechanical interactions among different crystals nor did they consider external or internal boundary conditions (Roters et al., 2011). That is why variational methods in the form of finite element approximations have become popular in this field. These methods are known as crystal plasticity finite element methods.

The crystal plasticity finite element method is an approach that uses finite element calculations to describe the time and crystal orientation dependent deformation of crystalline materials. A weak form of the principle of virtual work, in a given finite volume element, is used to support the variational solution of force equilibrium. It is hence appropriate to say that CPFEM approaches can be used as constitutive material models and consequently may be used into finite element programs to solve industrial, large scale problems.

Deforming microstructures often show multiple deformation mechanisms taking place simultaneously. Speaking in terms of material modeling, this requires multiple sub-models to describe the evolution of these interactions at the same material point, and this need is catered for by CPFE. Figure 1.3 simplifies this point even further where figure 1.3 (a) shows just one type of deformation mechanism and one phase at one integration point, while figure 1.3 (b) shows multiple deformation mechanics taking place at a single point.

Among the many advantages of CPFE models, one is that it has the ability to solve crystal mechanical problems under internal or external boundary conditions. This

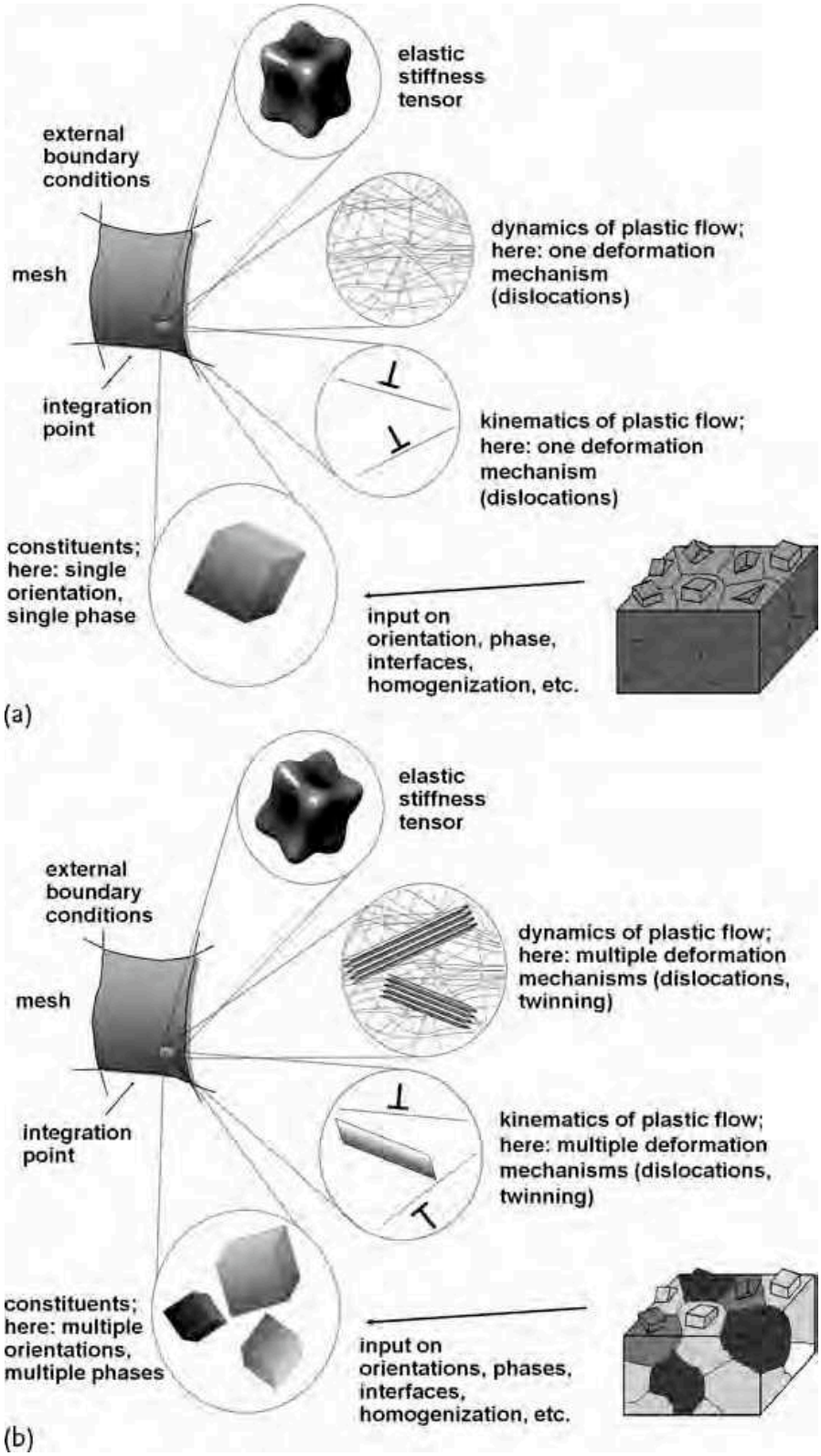

Figure 1.3: Constituents in CPFE. (a) Scenario with just one type of deformation mechanisms and one phase. (b) Scenario showing the case of multiple deformations mechanics and phases taken at a single integration point (Roters et al., 2010).

is an imperative part of crystal mechanics because CPFE takes into account different inter and intra micromechanical grain interactions (Sachtleber et al., 2002). As shown by Arsenlis et al. (2004), and Arsenlis and Parks (1999) CPFE methods give an edge to incorporate constitutive formulations for hardening and plastic flow at elementary slip system levels.

CPFE simulations have the capability of being used both at mesoscopic and macroscopic levels (Raabe et al., 2002). At mesoscopic levels, CPFE is gaining momentum because of the difficulty to control experimental boundary conditions, which in a numerical context can be given by the user with ease. At small scales, CPFE applications range from nano-indentation simulations (Wang et al., 2004) to mechanics at interfaces (Clark et al., 1992) to damage initiation (Bieler et al., 2009), fatigue behaviour (McDowell and Dunne, 2010) etc. Macroscopic applications of CPFE include forming and texture simulations (Kraska et al., 2009) where the primary concern is to predict the precise product shape, material failure, thickness distribution and material flow of the formed product.

Since the foundations of CPFE were first laid by Asaro and Rice (1977) and then further elaborated by Peirce et al. (1982), this method has been improved into a whole framework of constitutive formulations. These simulations started off for single crystals but were later utilized for polycrystalline materials (Harren et al., 1988) in a two dimensional setup using only two to three slip systems. Later, Becker et al. (1991) became the first to simulate a three dimensional model for a twelve slip system FCC crystal lattice. Increases in computational power have further eased these CPFE simulations. More recently, in the realm of grain boundary mechanics, recent advances have allowed researchers to simulate polycrystal behavior with great efficiency (Barbe et al., 2001; Ma et al., 2006).

In context to fatigue, several authors have used crystal plasticity approaches to model the cyclic response of metallic materials (Goh et al., 2006; Morrissey et al., 2003; Bennett and McDowell, 2003; Goh et al., 2001; Ozturk et al., 2016; Dunne et al., 2007a; Li et al., 2015).

This is a crucial couple because fatigue is extremely sensitive to microstructural features, especially as the number of cycles progresses, plasticity segregates at certain local locations. If these locations can be pinpointed, predictions of fatigue crack initiation become easier (Proudhon et al., 2016). Also, understanding how local non-linearities emerge to give a certain cyclic response is a topic which can lead to an effective design of engineering components. More light will be shed on this in chapter 2 of the thesis.

1.3 Reduced order modeling

When material microstructures are under consideration, continuum models can be an attractive approach to assess mechanical properties. Coupling micro-mechanical laws with complex geometries has in present times gained massive popularity (Gérard et al., 2013; Gu et al., 2019). One way to do this is to use the concept of a representative volume elements (RVE) where a virtual microstructural realization is generated and appropriate boundary conditions are prescribed (Prithivirajan and Sangid, 2018; Zhang et al., 2016; Kotha et al., 2019; Sun et al., 2018). These boundary conditions usually represent an average stress or strain state of the material which conforms to the macroscopic averaged response of the material. This is followed by a numerical procedure to solve the boundary value problem. One of the most popular methods to discretize the weak form of the constitutive equations is the Finite Element method, which is also employed in this article. Using this method, the constitutive equations can be integrated at each material point and huge insight can be gained as to what is happening locally at certain geometric locations. This requires considerable computational resources for direct numerical simulations. Although the current state of computer science is considerably advanced, with numerous parallel as well as high performance computing strategies available (Shantsev et al., 2017; Yagawa and Shioya, 1993), full resolution simulations are still not optimal because of their high computational costs. Model order reduction techniques pertain to problems where the order of the model depends on the number of independent state variables. Several authors (Matouš et al., 2017) have proposed model reduction techniques for the approximation of plasticity problems. For instance Pelle and Ryckelynck (2000) proposed to use the LATIN method to iteratively approximate the solution. Fritzen and Hassani (2018) use a space-time technique where a low number of nonlinear equations is solved in the reduced setting but full spatial information can be recovered at any given time. Michel and Suquet (2003) have proposed to use the nonuniform transformation field analysis (NTFA) approach where they consider nonuniform plastic strain fields with the aim of reducing the number of macroscopic internal variables. Another model order reduction technique used frequently is proper orthogonal decomposition (POD), first proposed by Karhunen (1946) and Loève (1963) developed initially for statistical analyses. This POD basis comprises of the state subspace which is made of different time steps of a simulation or even different mechanical problems altogether. Using POD bases to predict mechanical models was first done by N. Lorenz (1956) for weather forecasts. In the context of RVE homogenization Yvonnet and He (2007) have already used a POD based technique for hyper-elastic materials whereas Hernàndez et al. (2014) used a hyper-reduced POD procedure to reduced the order of the model. The size of the full

order model is proportional to the number of discrete unknowns. To counter this, the technique used in this thesis is to restrict the solution space to a significantly smaller subspace obtained using the reduced basis (Almroth et al., 1978b). Projecting the initial partial differential equation on the reduced basis then gives a projection based reduced order model.

In this work, model order reduction is discussed in the realm of the crystal plasticity finite element method. Figure 1.4 shows how several computational constraints affect the size of the full field model, which include but are not limited to the mesh density, size of the volume element (VE) and the complex constitutive laws being integrated at each material point. It is also being explicitly mentioned that the concept of a Representative VE is not necessary for application of the model order reduction techniques applied and developed here. On top of that, the current study pertains to cyclic loadings which make CPFEM computations even more expensive.

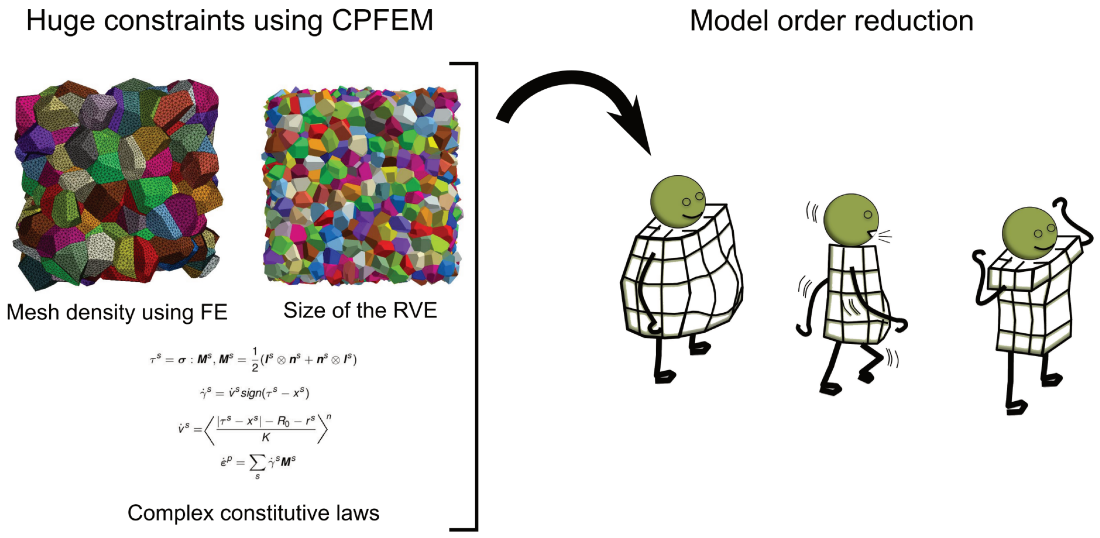

Figure 1.4: The need for reduced order modeling in CPFEM where the high fidelity is computationally extremely heavy. The model order reduction approach aims at reducing the size of the model.

1.4 Objectives

Modern analysis techniques use a combination of simulation and experiments to reduce manpower as well as expenses. Recent advances in science have compelled

the engineering world to develop numerical tools for the understanding of the local nature of plasticity. In this context, a topic understudied is of non symmetric cyclic loadings in metallic materials. In such a setting polycrystalline materials give differing mechanical responses which lead to a decrease in lifetime as well as an early onset of failure. Very few studies have been done to model this type of behavior at the microstructure level. The first objective of this work is to model non symmetric cyclic loadings using the crystal plasticity finite element approach. Characterization has to be done based on both the macroscopic as well as the mesoscopic response of the microstructure. The main idea is then to correlate the results at both scales and give a physical interpretation for such complex phenomena. This will lead to a better understanding of the evolution of plasticity and will shed light on how local hardening combines to give heterogeneous materials their characteristic mechanical properties. It is also known that different crystal plasticity parameters can result in similar mechanical responses. The objective of this work is also to scrutinize different parameter sets and characterize how varying hardening parameters govern the cyclic properties of polycrystalline materials.

The crystal plasticity finite element method has complex phenomenological laws associated to it and integrating them at each time step leads to extremely heavy computations. The second objective of this work is to couple model order reduction approaches with crystal plasticity finite element simulations. A benefit of this is the acceleration of computationally intensive simulations, which can lead to an estimate of the nonlinear development of plasticity.

Reduced order models are valid for a certain parameter space which means that conventionally they should be used within certain limits. An objective is also to understand these limits in the context of CPFEM. The hybrid hyper-reduction method will be employed as the model order reduction technique. The resulting combination of numerical modeling with reduced order approximations are topics under scrutiny by the scientific community and hold great value for the engineering world.

1.5 Outline

The main content of this work is split into three different chapters:

- In Chapter 2 non symmetric cyclic loadings are modeled using CPFEM. A detailed characterization is done for both single as well as polycrystals.

The mechanical states at cyclic stability are characterized using elaborate diagrams. Details on the nonlinear evolution of hardening are presented and the factors affecting their macroscopic behavior are discussed. It is also shown how different regions in the microstructure accommodate each other and this local rearrangement in hypothesized as the origin of a particular macroscopic response.

- Chapter 3 starts by giving a brief introduction of the model reduction approach pertaining to crystal plasticity finite element simulations adopted in this work. Hyper-reduction is compared with hybrid hyper-reduction and the superiority of the later is shown numerically. As a test case, strain ratcheting predictions are done on a large finite element mesh. Macroscopic as well as local statistics are presented on different constitutive variables and errors on each variable are elaborated. Computational times for using the model order reduction procedure are also shown and compared with the full field estimation.

- Chapter 4 presents how model order reduction can be used for parametric simulations in crystal plasticity. Characterization of the parameter space is done by taking some numerical examples, and finally the limits to which the ROM can be used, as observed by the authors, are elaborated.

Conclusions and future work are proposed in Chapter 5.

Chapter 2

Crystal plasticity modeling of the cyclic behavior of polycrystalline aggregates under non-symmetric uniaxial loading

Résumé

Lorsqu'un échantillon est soumis à une charge cyclique sous une contrainte ou une déformation moyenne, on observe généralement un rochet incrémentiel de contrainte ou des phénomènes de relaxation de contrainte moyenne. Les expériences montrent que pour les matériaux métalliques, il n'y a généralement pas de relaxation complète des contraintes moyennes, ni de saturation du rochet macroscopique de déformation. Peu d'attention a été accordée à la modélisation de ces phénomènes à l'aide d'agrégats polycristallins, en particulier en ce qui concerne le régime de stabilité mécanique cyclique. Dans ce travail basé sur un modèle élémentaire de plasticité cristalline pour les cristaux FCC et des simulations à grande échelle par éléments finis, il est démontré que l'interaction entre différents grains est suffisante pour prédire des phénomènes aussi complexes. Il est mis en évidence

A part of this chapter has been submitted to a journal

comment différentes régions du polycristal s'accommodent les unes aux autres et comment la définition classique du rochet de déformation à vitesse constante ou d'une contrainte moyenne nulle est presque impossible à appliquer à un agrégat polycristallin. De plus, il est démontré que même si une boucle d'hystérésis de contrainte macroscopique stable est observée, des phénomènes de rochet peuvent encore être observés à l'échelle locale. Les distributions de différentes quantités constitutives à l'intérieur d'un polycristal sont également analysées, ce qui donne une nouvelle idée de ce qui se passe à l'intérieur d'un polycristal en termes de redistribution des contraintes et des déformations. En particulier, l'existence de distributions bimodales évolutives des contraintes et des déformations plastiques accumulées est mise en évidence et liée à l'apparition de secousses plastiques et à une relaxation moyenne incomplète des contraintes. Deux critères numériques de détection du phénomène de rochet sont finalement proposés et discutés.

2.1 Introduction

Most metallic materials have a heterogeneous microstructure, and this local disorder results in specific mechanical properties. Several studies have already been undertaken to link micro-macro properties of metals (Barbe et al., 2001; Dunne et al., 2007b; Zhang et al., 2007, 2016; Guilhem et al., 2018), but how local properties affect macroscopic properties is still not fully understood. In particular, the behavior of metallic materials under cyclic loading conditions (Ghorbanpour et al., 2017; Smith et al., 2018; Yu et al., 2013) is still the subject of considerable attention. This chapter explores two topics, namely ratcheting and mean stress relaxation in polycrystal aggregates under cyclic loading. Both phenomena are controlled by exactly the same physical processes form the crystallographic slip perspective, differing only by virtue of the applied boundary conditions. For example, asymmetric stress-controlled uniaxial cyclic loading can result in strain ratcheting, i.e. a progressive, incremental inelastic deformation leading to a shift of the stress-strain hysteresis loop along the strain axis (Kang et al., 2010; Fournier and Pineau, 1977; Ohno et al., 1998; Jiang and Sehitoglu, 1994; Hassan and Kyriakides, 1994a; Portier et al., 2000; Hassan and Kyriakides, 1994b). Mean stress in this article is defined as $(\Sigma_{\max} + \Sigma_{\min})/2$ where $\Sigma_{\max}$ and $\Sigma_{\min}$ are the maximum and minimum stresses in a cyclically loaded component. On the other hand stress amplitude is defined as $(\Sigma_{\max} - \Sigma_{\min})/2$. With regards to asymmetric strain controlled cyclic loadings, it is also known that under a given stress amplitude, increasing the stress amplitude under a constant non zero mean stress or increasing the applied mean stress, both increase the rate of ratcheting (Goodman, 1984). On

the other hand, experimental observations indicate levels of mean stress for which there is very low ratcheting and the mechanical state of the material converges towards plastic shakedown (Pellissier-Tanon et al., 1982). Similarly, for asymmetric strain controlled loading conditions, a cyclic mean stress is observed, and several experimental studies (Wehner and Fatemi, 1991; Nikulin et al., 2019; Prithivirajan and Sangid, 2018) have deciphered the corresponding physical mechanisms. These observations show that for a given positive mean strain, and a low strain amplitude, the mean stress does not completely relax to zero. Also, increasing the strain amplitude leads to a nonlinear decrease of the mean stress until it finally vanishes (Arcari et al., 2009). From a modeling perspective, the mechanical cyclic response is sensitive to the strain path and is driven by the Bauschinger effect, as modeled by Chaboche (1986, 1989). Classical macroscopic models (Chaboche, 1989) predict an excess of strain ratcheting as well as mean stress. Some researchers have proposed to introduce additional kinematic and isotropic hardening terms (Chaboche et al., 2012), resulting in numerous material parameters to be calibrated. Any change in the material requires recalibration of parameters. Also, no microstructural characteristics of the underlying material are captured by such phenomenological models, which inhibits further inspection of the physics of deformation of the material. Crystal plasticity models coupled with computational homogenization, on the other hand, offer a way to link cyclic micro-macro properties of metallic materials (Shenoy et al., 2008). The deformation behavior of a single crystal at the slip system level is used to determine the properties of polycrystalline aggregates using representative volume elements. This procedure, although phenomenological at constitutive single crystal level, provides a realistic insight into what is happening within a polycrystal as shown by comparison between simulations and strain field measurements (Zhao et al., 2008; Zaafarani et al., 2006).

For strain ratcheting studies, Morrissey et al. (2003) were first to show using crystal plasticity that the transition to void formation and growth failure mode at high R ratios in Ti-64 were due to a transition to cyclic ratcheting, and discussed this a breach of the percolation limit for ratchet strain. Goh et al. (2006) studied ratcheting and shakedown under fretting fatigue. Shenoy et al. (2008) used experiments and full field CPFEM simulations to train an artificial neural network for notch root responses with ratcheting for Ni-base superalloy IN100. Zhang et al. (2007) used CPFEM to model response of polycrystals under mean stress, with unloading and large ratchet strains. Zhang et al. (2009) used CPFEM to model ratchetting under fretting contacts. Xie et al. (2004) and Sinha and Ghosh (2006), followed by Dingreville et al. (2010), were among the first authors to use polycrystalline aggre-

gates coupled with CPFEM to model ratcheting. These researchers simulated the first few cycles and then extrapolated their results to larger cycle numbers. More recently, Hennessey et al. (2017) and Cruzado et al. (2017) proposed to change the kinematic hardening law from an Frederick and Armstrong (2007) formulation to a modified Ohno and Wang (1993) type law. Hennessey et al. use an accelerated simulation and run the simulation for a hundred cycles, while Cruzado et al. resort to a cycle jump technique (Cruzado et al., 2012; Azzouz et al., 2010; Mary and Fouvry, 2007) to extrapolate the constitutive response. Both groups focus on the macroscopic properties of the aggregate rather than on local stress and strain distributions. The main limitations of all the conducted studies are that local heterogeneities and the physics behind these phenomena are neglected in favor of focusing on the macroscopic stability of the stress-strain hysteresis loop. Attention is paid essentially to matching simulation and experimental results at the macroscopic level. In a recent contribution by Colas et al. (2019) the authors evidence local ratcheting phenomena in a polycrystalline aggregate under symmetric strain loading conditions. Local ratcheting phenomena are found to be more pronounced at a free surface than in the bulk. The analysis is however limited to one single realization, without statistical considerations. The objective of the present work is to show that simulations of polycrystalline aggregates based on the most simple crystal plasticity laws can reproduce the main phenomenological features of asymmetric cyclic uniaxial plasticity and to correlate them with the stress and strain distributions inside the aggregates.

As stated earlier, the driving force for strain ratcheting and cyclic mean stress relaxation is the Bauschinger effect, which in a modeling perspective is governed by kinematic hardening. Kinematic hardening controls the ratcheting behavior as well as mean stress relaxation in structural components. Isotropic hardening, on the other hand, decreases the rate of plastic strain evolution per cycle. Single crystal behavior exhibits isotropic hardening effects due to multiplication and interaction of dislocations, as well as kinematic hardening as a result of polarization of dislocation structures Méric et al. (1994). In a polycrystal, the cyclic response results from these two hardening components inside the grains and from the intergranular interactions. Hence, to assess these complex mechanisms, a very simple constitutive law is retained at the single crystal level for the systematic study of the present work. It is first limited to purely kinematic hardening. This is a simplification which complies with usual observations that isotropic hardening remains very limited in metallic materials used for engineering purposes such as nickel-based superalloys under cyclic loading, which is the target material class of the present work (Chaboche et al., 2012). A rate–independent crystal plasticity model formulation is used to avoid the contamination of the final results by viscosity ef-

fects. The selected crystal plasticity model by (Forest and Rubin, 2016) exhibits a smooth elasto-plastic transition and is strictly rate-independent. In what follows, finite element simulations of polycrystalline aggregates will be shown to provide a realistic description of ratcheting and mean stress relaxation in face centered cubic (FCC) metals, without resorting to complex memory variables in contrast to macroscopic approaches. Two types of materials are taken into account, one with a low hardening limit and high yield strength similar to Nickel base superalloys, and a second one with stronger hardening and a low yield strength as seen in copper based alloys as a reference (Siska et al., 2007). Finally, the results are analyzed along two lines, i.e. at the macroscopic scale first and then at the local scale looking at field variables influencing the phenomena.

In this article it is shown that without changing the constitutive equation, a polycrystal can mimic experimental response. Macroscopic averaged results are shown to reproduced different regimes observed while asymmetrically cycling a metallic material. Diagrams are also built to characterize ratcheting and cyclic mean stress relaxation both in single as well as polycrystals. Local analyses of the results then sheds light on the microstructural response of the polycrystal. More specifically, trends in the evolution of plasticity are shown in the entire microstructure with the help of probability density plots. These plots are then analyzed and concrete statistical conclusions are drawn for the first time to answer why a polycrystal stops ratcheting or retains a cyclic mean stress.

The chapter is organized in the following manner. In Section 2.2 the crystal plasticity material model is formulated. Section 2.3 presents the finite element model, material parameters, as well as the physical aspects of the microstructure. Results and discussions are provided in Sections 2.4, regarding macroscopic aspects, and 2.5, regarding local stress and strain fields. A long cyclic simulation is presented in Section 2.6. Discussion about the obtained results and their qualitative comparison with experimental findings is done in Section 2.7. This is followed by the conclusions in Section 2.8.

2.2 Crystal plasticity model

In the present work a small strain crystal plasticity formulation is used for the computation as most local strains remain below 5%. Each grain is considered as an initially homogeneous single crystal. To ease the interpretation of the numerical results, a rate–independent formulation is selected, using the single crystal

plasticity model recently proposed by Forest and Rubin (2016). An advantage of using a rate–independent model coupled with a small strain assumption is the numerical efficiency which is crucial when simulating hundreds of cycles under various load amplitudes. In addition, it has been decided to use exclusively kinematic hardening because it governs ratcheting and mean stress relaxation. Face centered cubic (fcc) single crystal metallic materials comprising n plastic slip systems, each having a slip system direction $\underline{\underline{\ell}}^s$ and a normal to the slip plane $\underline{\underline{n}}^s$ are considered. The partition of the strain tensor introduces elastic and plastic parts:

$$\underline{\underline{\varepsilon}} = \underline{\underline{\varepsilon}}^e + \underline{\underline{\varepsilon}}^p \tag{2.1}$$

The Hooke law relates the stress tensor to the elastic strain tensor. For cubic elasticity, a fourth rank tensor of elastic moduli $\underline{\underline{\underline{\underline{C}}}}$, involving three independent parameters, governs the elastic behavior:

$$\underline{\underline{\sigma}} = \underline{\underline{\underline{\underline{C}}}}\,\underline{\underline{\varepsilon}}^e \tag{2.2}$$

The plastic strain rate results from the slip processes with respect to all active slip systems,

$$\dot{\underline{\underline{\varepsilon}}}^p = \sum_{s=1}^{n} \dot{\gamma}^s \underline{\underline{m}}^s \tag{2.3}$$

with $\underline{\underline{m}}^s$ being the Schmid orientation tensor defined as

$$\underline{\underline{m}}^s = \frac{1}{2}\left(\underline{\ell} \otimes \underline{n}^s + \underline{n} \otimes \underline{\ell}^s\right) \tag{2.4}$$

The amount of slip on each slip system is denoted by the variable γ^s. The driving force for plastic slip on slip system s is the resolved shear stress, computed using the Cauchy stress tensor ($\underline{\underline{\sigma}}$) according to:

$$\tau^s = \underline{\underline{\sigma}} : \underline{\underline{m}}^s = \sigma_{ij} m_{ij}^s \tag{2.5}$$

The yield criterion is a generalization of Schmid's law involving scalar hardening variables r^s and x^s according to Méric et al. (1991).

$$f^s(\underline{\underline{\sigma}}, x^s, r^s) = |\tau^s - x^s| - r^s \tag{2.6}$$

Here, r^s denotes the radius of the elastic domain and x^s is a scalar back-stress characterizing the center of the elastic range in the one-dimensional space of resolved shear stresses. In slip based crystal plasticity, there are n such elastic ranges. Plastic slip can occur only if the function f^s becomes positive. The viscoplastic

flow rule given by Cailletaud et al. (1991), is proposed in terms of the viscosity parameters, K and n:

$$\dot{\gamma}^s = \left\langle \frac{f^s}{K} \right\rangle^n \text{sign}(\tau^s - x^s) \tag{2.7}$$

with the Macaulay brackets $< x >= \text{Max}(x, 0)$. In the present work following Forest and Rubin (2016), the rate of slip on each slip system is replaced by a rate-independent formulation of the form:

$$\dot{\gamma}^s = \dot{\varepsilon} \left\langle \frac{f^s}{K} \right\rangle \text{sign}(\tau^s - x^s) \tag{2.8}$$

where K is a positive constant having now the unit of stress and $\dot{\underline{\underline{\varepsilon}}}$ is a non-negative homogeneous function of order one in the total strain rate. In this model, $\dot{\underline{\underline{\varepsilon}}}$ is taken to be the total equivalent distortional strain rate:

$$\dot{\varepsilon} = \sqrt{\frac{2}{3}\dot{\underline{\underline{\varepsilon}}}' : \dot{\underline{\underline{\varepsilon}}}'}, \quad \dot{\underline{\underline{\varepsilon}}}' = \dot{\underline{\underline{\varepsilon}}} - \frac{1}{3}(trace(\dot{\underline{\underline{\varepsilon}}}))\underline{\underline{1}} \tag{2.9}$$

where $\underline{\underline{\varepsilon}}'$ is the deviatoric part of the total strain rate tensor $\dot{\underline{\underline{\varepsilon}}}$ and $\underline{\underline{1}}$ the unit. Since the rate of inelasticity is linear in the total equivalent strain rate $\dot{\underline{\underline{\varepsilon}}}$, all the evolution equations in the proposed theory are homogeneous of order one in time, characterizing a rate-independent response. Also, the rate of inelasticity is used for all states entailing no need for special treatment of loading and unloading conditions. In particular no consistency condition is needed in contrast to standard rate–independent plasticity. The amplitude of the overstress is controlled by the value of parameter K. It tends to zero for vanishing values of K. There is no indeterminacy in the selection of active slip systems according to the present model. The functional form of f and the evolution equations for isotropic (r^s) as well as kinematic (x^s) hardening remain unchanged compared to the original model (Cailletaud et al., 1991). The accumulated slip variable v^s is defined for each slip system by the following evolution equation:

$$\dot{v}^s = |\dot{\gamma}^s| \tag{2.10}$$

The evolution equations for the kinematic hardening variable is taken from Méric et al. (1991) and Busso and Cailletaud (2005) without modification. The nonlinear kinematic hardening evolution law

$$\dot{x}^s = C\dot{\gamma}^s - D\dot{v}^s x^s \tag{2.11}$$

depends on two material parameters, C and D. In the present chapter, there is no isotropic hardening so that the variable r^s has a constant value r_0, which corresponds to the initial resolved shear stress.

Two crystal plasticity parameter sets were chosen, as stated in table 2.2, where the saturated resolved shear stress is the same (i.e. $r_0 + C/D = 420$ MPa for both parameter sets); The difference however lies in the flipping of kinematic hardening and initial critical resolved shear stress. Parameter set 'LK' has a low kinematic hardening but a high initial critical resolved shear stress resembling aerospace alloys such as Inconel where the saturated value of the kinematic hardening variable is around one third of the initial yield stress. Parameter set 'HK' resembles an alloy with a low yield stress and a strong hardening such as copper where the saturated value of the kinematic hardening variable is three times that of the initial yield stress (Siska et al., 2007). Both parameter sets pertain to unit cells made of FCC crystals deforming plastically on octahedral slip systems $\{111\}\langle 110\rangle$. The slip systems, as ordered in the implicit simulation software Z–set package (2013), are given in table 2.1.

Slip system	Slip plane normal	Slip direction
1	(111)	$[\bar{1}01]$
2	(111)	$[0\bar{1}1]$
3	(111)	$[\bar{1}10]$
4	$(1\bar{1}1)$	$[\bar{1}01]$
5	$(1\bar{1}1)$	$[011]$
6	$(1\bar{1}1)$	$[110]$
7	$(\bar{1}11)$	$[0\bar{1}1]$
8	$(\bar{1}11)$	$[110]$
9	$(\bar{1}11)$	$[101]$
10	$(11\bar{1})$	$[\bar{1}10]$
11	$(11\bar{1})$	$[101]$
12	$(11\bar{1})$	$[011]$

Table 2.1: The 12 octahedral FCC slip systems numbered in the same order as they are defined in the code

2.3 FE model description

The numerical model was implemented in the implicit finite element solver Z–set package (2013). Literature findings show that the macroscopic representation of a micro-heterogeneous metallic material can be achieved with as few as one hundred grains (Barbe et al., 2001; Kanit et al., 2003), but matching macroscopic properties is not the goal. The goal here is to have a large enough statistical database so that local material response can be analyzed. Of course computational limitations

have to be acknowledged and extremely large polycrystals cannot be used. For this reason the microstructure generated is called a volume element (VE) as opposed to representative volume element (RVE). Two aggregates containing equiaxed grains, respectively called VE1 and VE2, were generated using the Voronoi tessellation technique with the help of the software VORO++ (Rycroft, 2009). A periodicity constraint was applied to obtain periodic microstructures. The software Gmsh was used to mesh both geometries, enforcing conditions of periodicity for the obtained meshes. Both aggregates contain 300 grains and reduced quadratic tetrahedral elements C3D10. The mesh of VE1 contains 194903 nodes and 130171 elements whereas the mesh of VE2 is made of 192042 nodes and 128166 elements (see figure 2.1 (a) and (d)). Each tetrahedral finite element has 10 nodes and 4 Gauss points.

The grain sizes in both VEs (as seen in figure 2.1 (b) and (e)), have a normal distribution with the crystal orientations uniformly distributed in the polycrystal (figure 2.1 (c) and (f)).

-	Parameter set LK	Parameter set HK
Cubic elasticity	C_{1111} = 259600 MPa C_{1122} = 179000 MPa C_{1212} = 109600 MPa	C_{1111} = 259600 MPa C_{1122} = 179000 MPa C_{1212} = 109600 MPa
Critical resolved shear stress	r_0 = 320 MPa	r_0 = 100 MPa
Kinematic hardening	C = 100000 MPa D = 1000	C = 320000 MPa D = 1000
Overstress	K = 9 MPa	K = 9 MPa

Table 2.2: Crystal plasticity parameters used for both parameter sets. The saturated resolved shear stress is the same for both parameter sets; The difference being that parameter set LK has a low kinematic hardening and high critical resolved shear stress and vice versa.

Computational requirements

The implicit finite element code (Z–set package, 2013) is used to solve the problem. The global equilibrium is solved using a Newton-Raphson algorithm. Integration of constitutive equations at the Gauss points is performed using the second order Runge-Kutta method with automatic time stepping (Besson et al., 2009). For a crystal plasticity simulation, loading one job of the present size requires 31.5 gigabytes RAM. The MPI parallel computing algorithm implemented in Zebulon

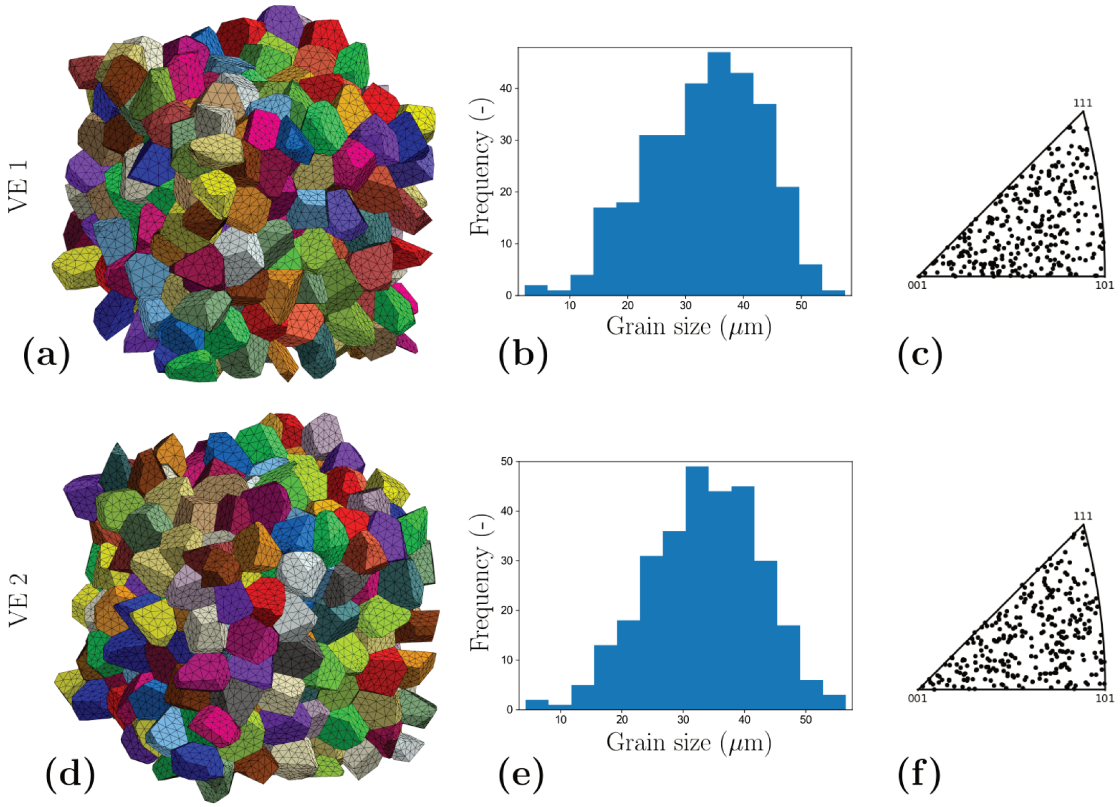

Figure 2.1: 300 grain polycrystals for the FE simulations, along with the inverse pole figures of the crystallographic orientations used in the VEs

is used with 4 processors for each job. Each job requires around 24 hours to complete one cycle and to run one hundred cycles, it required 100 days each. More than 320 simulations are being post-processed for this chapter, while the actual number of calculated test cases is at least fifty times more than this. Given the number of DOFs of each mesh and the cyclic nature of the problem, data of more than 20 TBytes were generated.

Boundary conditions

In the article, $\underline{\underline{\varepsilon}}$ will be used to refer to the local strain tensor, and $\underline{\underline{E}}$ will point to the macroscopic symmetric second-rank strain tensor defined as the average strain over the whole volume:

$$< \underline{\underline{\varepsilon}} >= \frac{1}{V} \int_V \underline{\underline{\varepsilon}} dV = \underline{\underline{E}} \tag{2.12}$$

Similarly, $\underline{\underline{\sigma}}$ will be the local stress tensor and the macroscopic stress $\underline{\underline{\Sigma}}$ will be defined as its spatial average as follows:

$$< \underline{\underline{\sigma}} >= \frac{1}{V} \int_V \underline{\underline{\sigma}} dV = \underline{\underline{\Sigma}} \tag{2.13}$$

Periodic boundary conditions were prescribed on the VEs such that the displacement vector field $\underline{u}$ over the entire volume takes the form:

$$\underline{u} = \underline{\underline{E}}.\underline{x} + \underline{v} \quad \forall \underline{x} \in V \tag{2.14}$$

where the fluctuation $\underline{v}$ is periodic. This fluctuation takes the same value for each pair of homologous points at ∂V. Anti-periodic boundary conditions are prescribed to the traction vector $\underline{\underline{\sigma}}.\underline{n}$ where $\underline{n}$ is the outer normal to ∂V at $\underline{x}$. The displacement and traction vectors are assumed to be continuous at the grain boundaries. For strain ratcheting, the macroscopic stress component Σ_{11} was imposed, whereas for mean stress relaxation the macroscopic strain component E_{11} was controlled. In both cases, all remaining volume averaged stress components are fixed to zero i.e. $\Sigma_{22}, \Sigma_{33}, \Sigma_{12}, \Sigma_{23}, \Sigma_{31} = 0$.

2.4 Results at macroscopic scale

This section presents the results obtained at a global level by averaging the stress and strain fields on the whole aggregate. Two loading types are investigated leading to ratcheting and mean stress relaxation respectively. In each case, the response obtained with a single crystal is given as an elementary reference.

2.4.1 Ratcheting in single crystals

The simulations of this subsection are performed at the material point level assuming homogeneous deformation. A uniaxial cyclic stress was imposed on the material element. Depending on the stress amplitude ($\Delta\Sigma/2$) and the mean stress $\bar{\Sigma}$, the resulting cyclic behavior can be broken down into three distinct responses i.e. elasticity, elastic shakedown and ratcheting. Figure 2.2 depicts these regimes in a stress amplitude ($\Delta\Sigma/2 = (\Sigma_{\max} - \Sigma_{\min})/2$) vs mean stress ($\bar{\Sigma} = (\Sigma_{\max} + \Sigma_{\min})/2$) diagram. From figure 2.2, it can be seen that elastic shakedown refers to the material deforming plastically during the first few cycles and the subsequent response being elastic. Ratcheting in a single crystal is the progressive accumulation of strain per cycle without stopping, as signified by the red region. So depending on the loading type, a single crystal is bound to either ratchet or elastically shakedown. A missing region, as opposed to experimental observations, is that of plastic shakedown, which refers to an open stress-strain hysteresis loop which does not move forward on the strain axis. These three regimes can be classified as follows:

- Elastic if $\Delta\Sigma/2$ is smaller than the yield strength
- Shakedown if $\Delta\Sigma/2$ is smaller than the combination of the yield strength and the saturated isotropic hardening
- Ratcheting if $\Delta\Sigma/2$ is greater than the combination of the yield strength and the saturated isotropic hardening

Two single crystal response have been shown in 2.3 using the parameter set LK, where (a) and (b) show the responses of the orientation [001] and [111]. It can be seen that the regions which ratchet and shakedown preserve a constant ratio among each other, while the size of the whole diagram changes depending on the crystallographic orientation.

2.4.2 Ratcheting in polycrystals

In this section simulations were run on polycrystal aggregates as shown in figure 2.1. A periodic macroscopic stress (Σ_{11}) was imposed on polycrystalline volume element periodic boundary conditions. Two stress strain curves pertaining to the two parameter sets are shown in figure 2.4. The boundary conditions for both

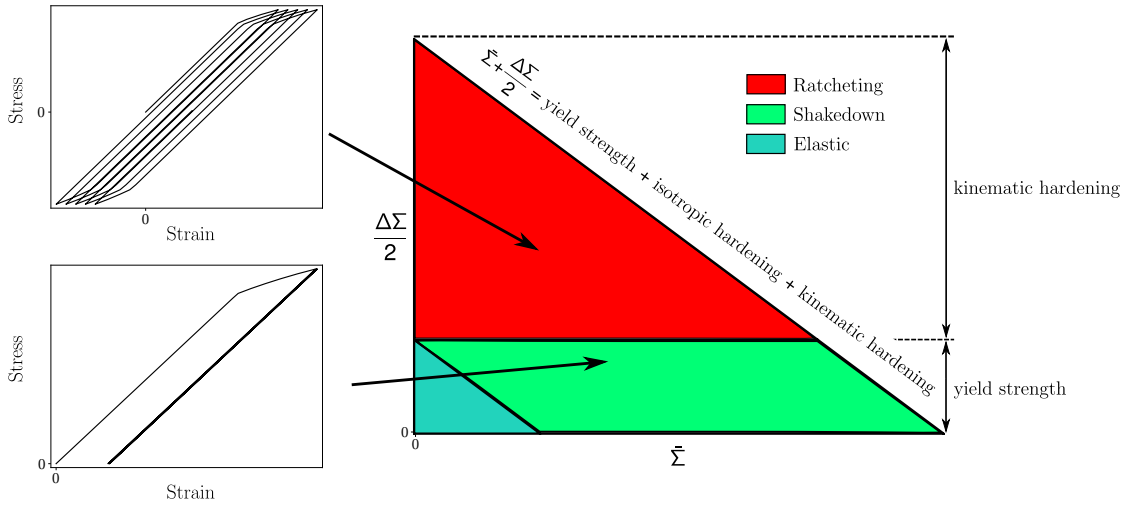

Figure 2.2: Under asymmetric load control, the single crystal response which shows three distinct regions i.e. elastic, shakedown and ratcheting

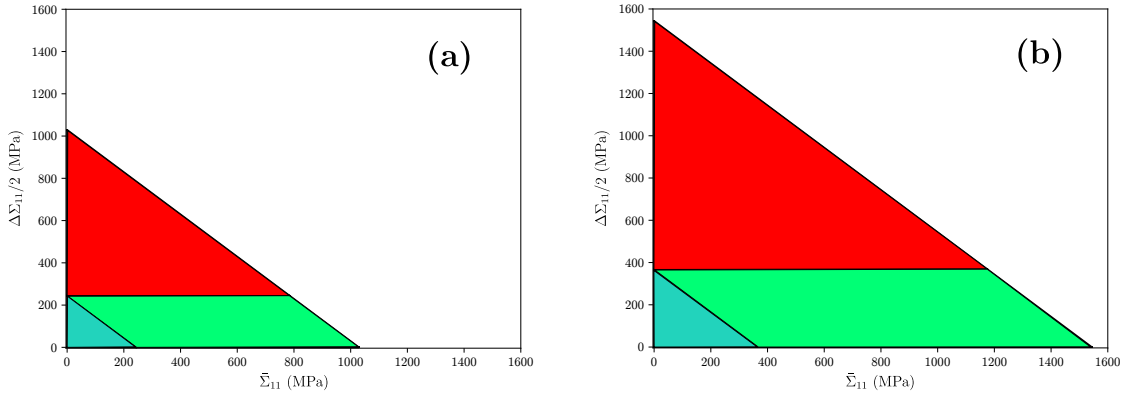

Figure 2.3: Under asymmetric load control, using parameter set LK, a single crystal response for crystallographic orientations: (a) [001] (b) [111]

simulations are kept the same where $\Sigma_{\max} = 1020$ MPa and $R_\Sigma = -0.7$ ($R_\Sigma = \Sigma_{\min}/\Sigma_{\max}$) and the first ten cycles are plotted for both simulations. From the plot it can be seen that the curve for parameter set HK ratchets much more than the curve for parameter set LK because of the presence of a much higher kinematic hardening in the former.

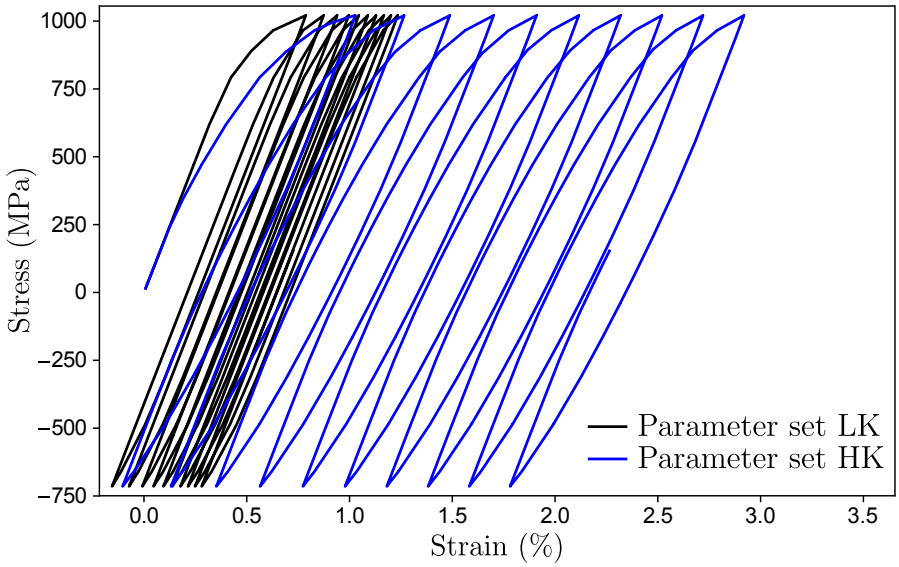

Figure 2.4: For an asymmetric load controlled test, stress (Σ_{11}) vs strain (E_{11}) curves for both parameter sets. The loading conditions are kept the same for both i.e. $\Sigma_{\max} = 1020$MPa and $R_\Sigma = -0.7$. Only the first ten cycles are plotted in each case.

Both simulations ratchet at a different rate and comparing the accumulated axial strain can give a misleading estimation of what is ratcheting and what is shakedown. The same argument is valid for tests done at different amplitudes or loading ratios. Also, for a polycrystal, no matter how high the applied loading, the increment in accumulated strain $\Delta E = E_{n+1} - E_n$ always tends to decrease. This calls for the formulation of a robust test for discriminating ratcheting from shakedown. A test is proposed such that the delta accumulated strain per cycle is plotted (ΔE_{11}) against the number of cycles and identified with a power law series in the form:

$$E_{11}(N) = A \sum_{n=1}^{N} \frac{1}{n^\alpha} \tag{2.15}$$

where α is the slope of the series. The condition $\alpha > 1$ is required for the power

law series to converge. It follows that

$$\text{the test series} \begin{cases} converges, & \text{if } \alpha > 1. \\ diverges, & \text{if } \alpha \leq 1. \end{cases} \tag{2.16}$$

The left plot in figure 2.5 shows 3 simulations that were run for parameter set LK for three different stress amplitudes. For comparison, a slope of -1 is also plotted on the left corner. The series test was performed after running the simulations for a hundred cycles each. There is a clear difference between a curve that will converge (shakedown) or one that will diverge (ratchet). As a second criterion, the second derivative at cycle 100 is also computed for all curves which indicates the convexity (ratcheting) or concavity (shakedown) of the curves. After applying the convergence or divergence criteria, the converging test cases are broken into two parts depending on whether or not the width of the stress strain loop is open or closed at cycle 100. An open loop signifies that there is plastic shakedown, whereas a closed loop points to elastic shakedown. A small offset of tolerance is needed to establish what is meant by a closed loop. In the present work, the tolerance for the width of the loop at its mean stress is set to be $\delta = 1.0 \times 10^{-6}$. The right hand plot in figure 2.5 shows the macroscopic stress vs strain response for three selected cases at the first and at the hundredth cycle. It can already be established that the red curves are diverging while the green and blue curves are converging. Multiple simulations are run, on the polycrystal aggregates, at various load amplitudes and mean stresses for a hundred cycles each. Then the evolution of macroscopic strain in each simulation is assessed using the series comparison test, and a diagram similar to that of figure 2.2 is drawn for four cases i.e. for both VEs and for both parameter sets. Figure 2.6 shows that this diagram differs from the single crystal case. Four regions can be seen i.e. elastic, elastic shakedown, plastic shakedown and ratcheting instead of three in the single crystal case. The elastic region is determined using the plasticity criterion for metals of a yield strength of 0.2% plastic strain E^p, and is characterized by the gray region. The maximum stress limit for the polycrystal is computed by applying a macroscopic strain of 4%, the resulting stress being taken to be the limit above which the material cannot be loaded i.e. the top and bottom right corner of each plot in figure 2.6. In the same figure, the dots are found to concentrate into three regions, namely elastic shakedown, plastic shakedown and ratcheting respectively. For parameter set LK, the region in which ratcheting and plastic shakedown occur is very small because of the low kinematic hardening. Parameter set HK, on the other hand, leads to a much larger region for plastic shakedown and ratcheting. It should however be noted that the diagrams of figure 2.6 (a) and (b), as well as (c) and (d) are very similar signifying that it is both VEs can be regarded as representative microstructures capable of reproducing the typical cyclic mechanical behavior of

the material.

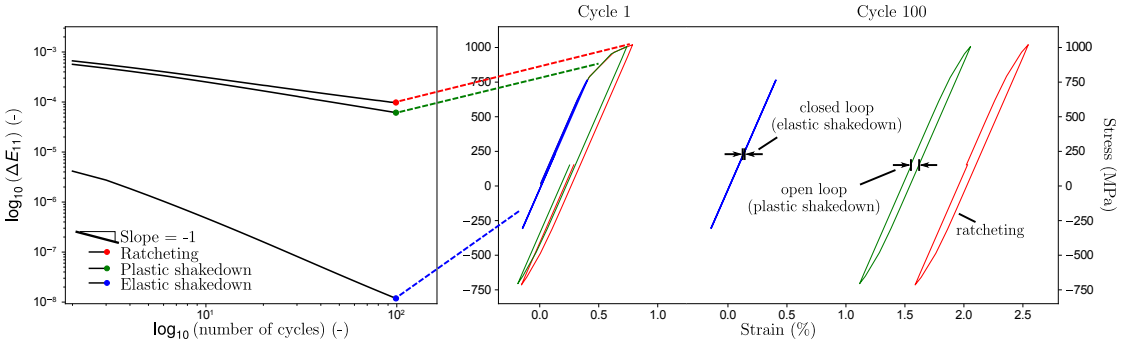

Figure 2.5: For asymmetric load controlled tests, the left figure shows the evolution of the ratcheting strain increment as a function of cycle number for 3 polycrystal simulations using parameter set LK, with three different stress amplitudes. The macroscopic stress (Σ_{11}) vs strain (E_{11}) plot is shown on the right for three simulations showing the cyclic response at cycles 1 and 100. The simulations selected illustrate the elastic shakedown, plastic shakedown and ratcheting phenomena.

2.4.3 Mean stress relaxation in single crystals

Under asymmetric cyclic strain control, the mean stress relaxes to a certain value when increasing the cycle number. At the macroscopic level, this mean stress $\bar{\Sigma}_{11}$, defined as $(\Sigma_{\max} + \Sigma_{\min})/2$, where $\Sigma_{\max}$ and $\Sigma_{\min}$ are the maximum and minimum stresses under peak strains. In this case, a single crystal cyclic response can be broken down into three distinct scenarios which are represented in figure 2.7 (a) and (b). Focusing on figure 2.7 (a), the first scenario shows the elastic regime where cyclic loading will have no effect on the cyclic mean stress redistribution. To remain in this regime plasticity has to be avoided i.e. the applied maximum strain ($E_{\max}$) should be:

$$E_{\max} < \frac{\Sigma_y}{Y}, \tag{2.17}$$

where Σ_y is the stress at which yielding starts and Y is the Young's modulus of the single crystal in the loading direction. Next, in the second scenario plasticity is observed only during the first tensile loading but upon unloading immediately after, elastic response is observed in the following cycles. To characterize the second scenario, the loading ratio R_E is defined as:

$$R_E = \frac{E_{\min}}{E_{\max}}, \tag{2.18}$$

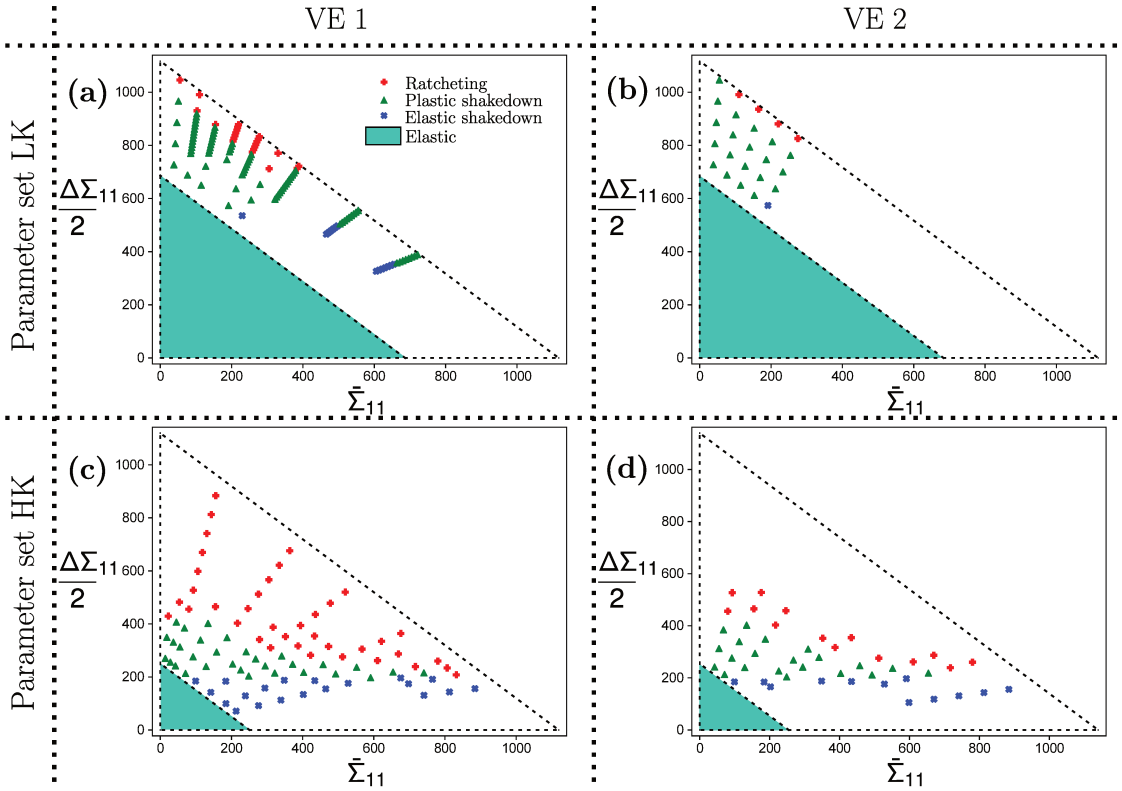

Figure 2.6: Ratcheting in polycrystals (a) VE 1 and parameter set LK, (b) VE 2 and parameter set LK, (c) VE 1 and parameter set HK, (d) VE 2 and parameter set HK. All values are in MPa

where $E_{\min}$ is the minimum applied strain. Then, the maximum applied strain $E_{\max}$ in the second regime should be in the following interval:

$$\frac{\Sigma_y}{Y} < E_{\max} < \frac{2\Sigma_y}{Y(1-R_E)}, \tag{2.19}$$

in the absence of isotropic hardening. Finally in the last regime, the mean stress relaxes to zero and the maximum applied strain should be:

$$E_{\max} > \frac{2\Sigma_y}{Y(1-R_E)}. \tag{2.20}$$

Fig. 2.7 (b) then depicts the curve of the mean stress at saturation vs maximum applied axial strain. The first scenario corresponds to the initial straight line with a slope of $Y(1-R_E)/2$; The second scenario depends on the type of kinematic hardening, and finally in the third scenario, a zero mean stress is found.

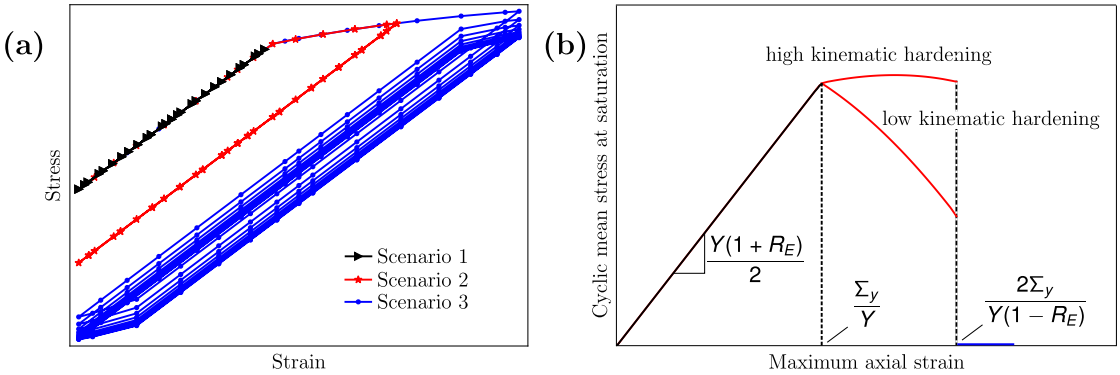

Figure 2.7: For a single crystal under asymmetric strain controlled loading, (a) stress vs strain plot showing the three scenarios of cyclic mean stress relaxation, and (b) mean stress at saturation vs maximum axial strain plot.

Example: analytic computation of mean stress relaxation in a single crystal

The following example pertains to FCC single crystals where the goal is to impose a strain based cyclic load and calculate the stress at the peak and valley of each cycle. For ease of analytic computation a purely elasto-plastic model is formulated as follows. The total applied strain (ε_{total}) can be broken down into its elastic (ε^e) and plastic (ε^p) part:

$$\varepsilon_{total} = \varepsilon^e + \varepsilon^p \tag{2.21}$$

and the elastic strain can be substituted by the macroscopic stress (σ) as follows:

$$\varepsilon_{total} = \frac{\sigma}{E} + \varepsilon^p \tag{2.22}$$

Speaking in terms of the slip rate ($\dot{\gamma}$), the plastic strain is defined as:

$$\varepsilon^p = \sum_{s}^{n} \gamma^s m^s \tag{2.23}$$

where n is the number of slip systems, and m^s is the Schmid factor for an individual slip system. For an FCC single crystal oriented at [001], eight octahedral slip systems are active, each having an identical Schmid factor of "$\sqrt{6}$", which gives a plastic strain of:

$$\varepsilon^p = 8 \times \frac{\gamma}{\sqrt{6}} \tag{2.24}$$

It is also known that the macroscopic stress is equal to:

$$\sigma = \tau^s \times m^s, \tag{2.25}$$

where τ^s is the resolved shear stress for any arbitrary slip system s. Substituting equations 2.24 and 2.25 into equation 2.22, the following is obtained:

$$\varepsilon_{total} = \frac{\sqrt{6}\tau}{E} + \frac{8\gamma}{\sqrt{6}} \tag{2.26}$$

Here, the path breaks into two routes: *tension* and *compression.*

Tension

For the tensile case, the kinematic hardening state variable (α) evolves as follows:

$$\dot{\alpha^s} = (1 - D\alpha^s)\dot{\gamma} \tag{2.27}$$

where D is the kinematic hardening material parameter. Integrating this relation, the following is obtained:

$$\alpha_f = \frac{(D\alpha_i - 1)\exp[D(\gamma_i - \gamma_f)] + 1}{D} \tag{2.28}$$

where the subscripts f and i are short for final and initial state. The evolution of the resolved shear stress for the *tensile* case will be as follows:

$$\tau = C\alpha + \tau_y \tag{2.29}$$

where C is the kinematic hardening material parameter, and τ_y is the critical resolved shear stress. Rearranging 2.26 and substituting it and equation 2.28 into equation 2.29, the following is obtained:

$$\tau_f = \frac{C}{D}\left[(D\alpha_i - 1)\exp\left[D\left(\gamma_i - \left(\frac{\sqrt{6}\varepsilon_{max}}{8} - \frac{3\tau_f}{4E}\right)\right)\right] + 1\right] + \tau_y \tag{2.30}$$

τ_f is then solved iteratively using the Newton-Raphson algorithm.

Compression

For the compressive case, the kinematic hardening state variable (α) evolves as follows:

$$\dot{\alpha^s} = (1 + D\alpha^s)\dot{\gamma} \tag{2.31}$$

where D is the kinematic hardening material parameter. Integrating this relation will result in:

$$\alpha_f = \frac{(D\alpha_i + 1)\exp[D(\gamma_f - \gamma_i)] - 1}{D} \tag{2.32}$$

The evolution of the resolved shear stress for the *compressive* case will be as follows:

$$\tau = C\alpha - \tau_y \tag{2.33}$$

Rearranging equation 2.26 and substituting it and equation 2.32 into equation 2.33:

$$\tau_f = \frac{C}{D}\left[(D\alpha_i + 1)\exp\left[D\left(-\gamma_i + \left(\frac{\sqrt{6}\varepsilon_{max}}{8} - \frac{3\tau_f}{4E}\right)\right)\right] - 1\right] - \tau_y \tag{2.34}$$

τ_f is then solved iteratively using the Newton-Raphson algorithm.

For a single crystal, the three regimes in asymmetric cyclic loadings can be quantified in terms of maximum strain amplitude as follows:

Regime 1
Regardless of the loading ratio, the maximum applied strain should be:

$$\begin{aligned}\varepsilon_{\max} &< \frac{\sqrt{6}\tau_y}{E} \\ &< \frac{\sqrt{6.00} \times 320.00}{113494.12} \\ &< 0.69\%\end{aligned}$$

Regime 3
The maximum strain needed for redistribution depends on the loading ratio and in this a loading ration of $R = -0.2$ has been selected. Hence, $\varepsilon_{\max}$ should be:

$$\begin{aligned}\varepsilon_{\max} &> \frac{2\sqrt{6}\tau_y}{E(1-R)} \\ &> \frac{2.00\sqrt{6.00} \times 320.00}{113494.12(1.00-(-0.20))} \\ &> 1.15\%\end{aligned}$$

Regime 2
In this regime, $\varepsilon_{\max}$ should be between that calculated for the first and third regime i.e.

$$0.69\% < \varepsilon_{\max} < 1.15\%$$

Figure 2.8 shows the analytic solution after solving the constitutive equations to stabilization. It can be seen that as predicted, the limit maximum strains come out to be exactly the same as the ones coming from the approximation of the differential equations (0.69% and 1.15%).

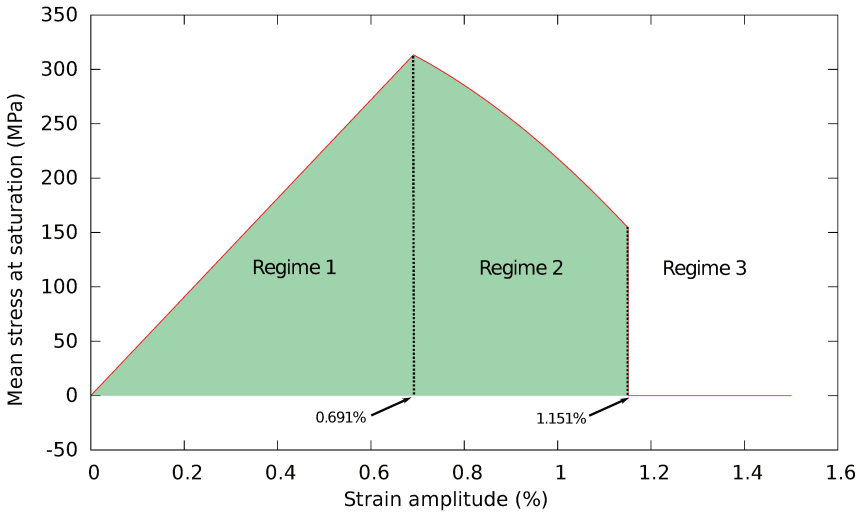

Figure 2.8: For single crystals, stabilized mean stress vs strain amplitude using the analytic scheme

To test this analytic solution, several finite element computations were also run. Figure 2.9 shows the comparison between the FE and analytic solution where almost an exact match between the two curves can be seen. The slight mismatch stems from the reason that in the analytic solution considered uses an elasto-plastic material model, while the FE computation considers a rate independent (Rubix) material model with an overstress, which slows down the mean stress saturation rate.

2.4.4 Mean stress relaxation in polycrystals

The boundary conditions applied to the meshes of figure 2.1 were periodic with a periodic strain E_{11} imposed on all elements. Figure 2.10 shows the stress (Σ_{11}) vs strain (E_{11}) response for the two parameter sets on VE 1. Both VEs were submitted to the same loading conditions $E_{11} = 0.85\%$ and R_E = -0.2. It can be seen that at cycle 100, the curve for parameter set LK stabilizes to a mean stress of 40 MPa, whereas the curve for parameter set HK relaxes to less than 0.5 MPa.

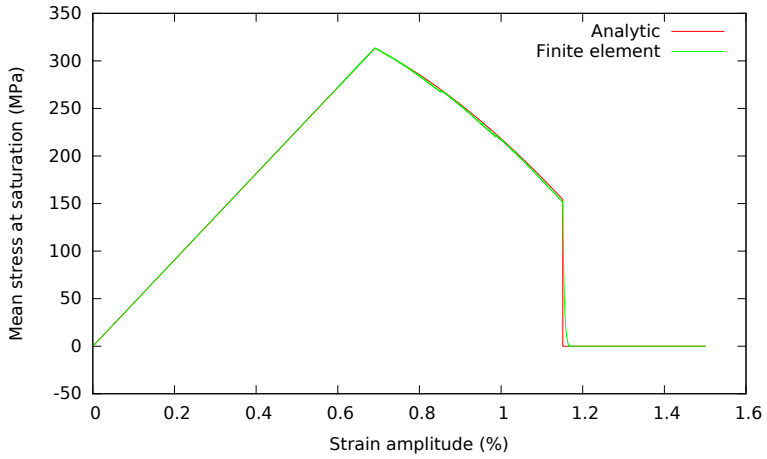

Figure 2.9: Comparison of the saturated mean stress between the analytic and finite element solution for a single crystal oriented at [001]

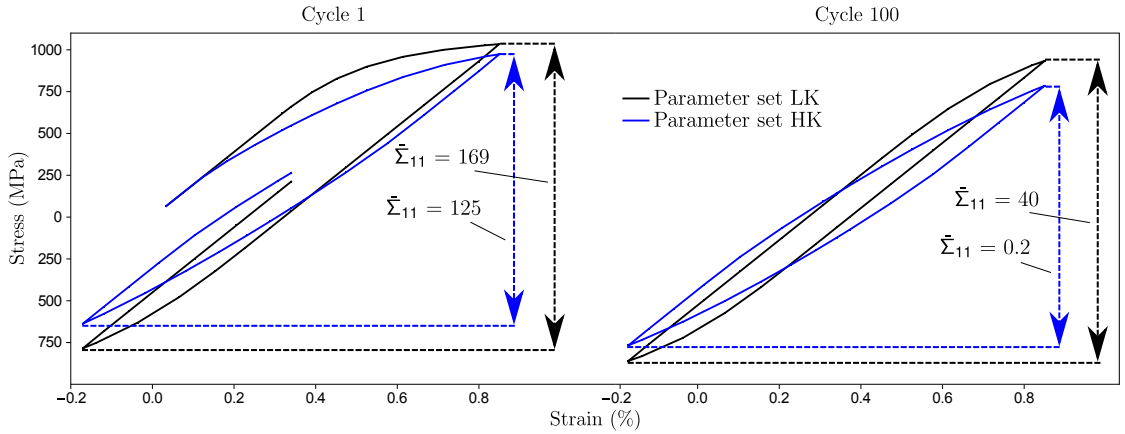

Figure 2.10: Under asymmetric strain controlled boundary conditions on VE 1, stress (Σ_{11}) vs strain (E_{11}) plot for both parameter sets with R_E = -0.2, and E_{11} = 0.85%. Responses were extracted at cycles 1 and 100 for both parameter sets. Cyclic mean stresses ($\bar{\Sigma}_{11}$) are also given for each case respectively.

According to Fig. 2.11, the response of the polycrystal can be characterized by the mean stress vs maximum axial strain diagram. Each point represents one simulation, with 100 cycles each, and a total of 21 simulations were run ranging from $E_{11} = 0.3\%$ to 1.3% with R $= -0.2$ for parameter set LK and VE 1. Similarly, 21 simulations ranging from $E_{11} = 0.11\%$ to 1.31% with R $= -0.2$ were performed for parameter set HK and VE 1. Figure 2.11 (a) and (b) show the response for parameters set LK and HK. It can be seen how the cyclic mean stress relaxes with the number of cycles. The response of a single crystal oriented at $\langle 001 \rangle$ is also plotted for both parameter sets for comparison. For both parameter sets, it was found that a steady state was achieved at cycle 100. Figure 2.11 (c) and (d) shows the response of both VEs for each parameter set at cycle 1 and 100. It can be seen that parameter set LK does not lead to mean stress relaxation to zero even at a high maximum axial strain. In contrast the material with parameter set HK relaxes to zero for $E_{11} = 0.5\%$. It can be seen that, when compared to a single crystal, the polycrystal response displays a smooth transition between the three scenarios which conforms to experimental findings (Chaboche et al., 2012). In addition, both VEs produce a similar response suggesting that the considered volume elements are representative with respect to this macroscopic response.

2.5 Analysis of local results

Attention is now focused on intragranular response of the material. Two types of local results are considered here, namely contour plots of stress and plane strain fields, as well as Gauss point statistics. For the contour plots, VE 1 and 2 are sliced at x = 0.5, as depicted in figure 2.12.

2.5.1 Local ratcheting behavior

The results of one stress controlled simulation up to 100 cycles with $\Sigma_{11} = 1021$ MPa and $R_\Sigma = -0.7$ for both VE 1 and 2 are analyzed. They are plotted in figure 2.13 at the time step corresponding to the tensile peak of the one hundredth cycle. An overlay of the grain boundaries is also superimposed on top of each contour map to make the observations easier to interpret. Eight contour plots are shown for the following field variables:

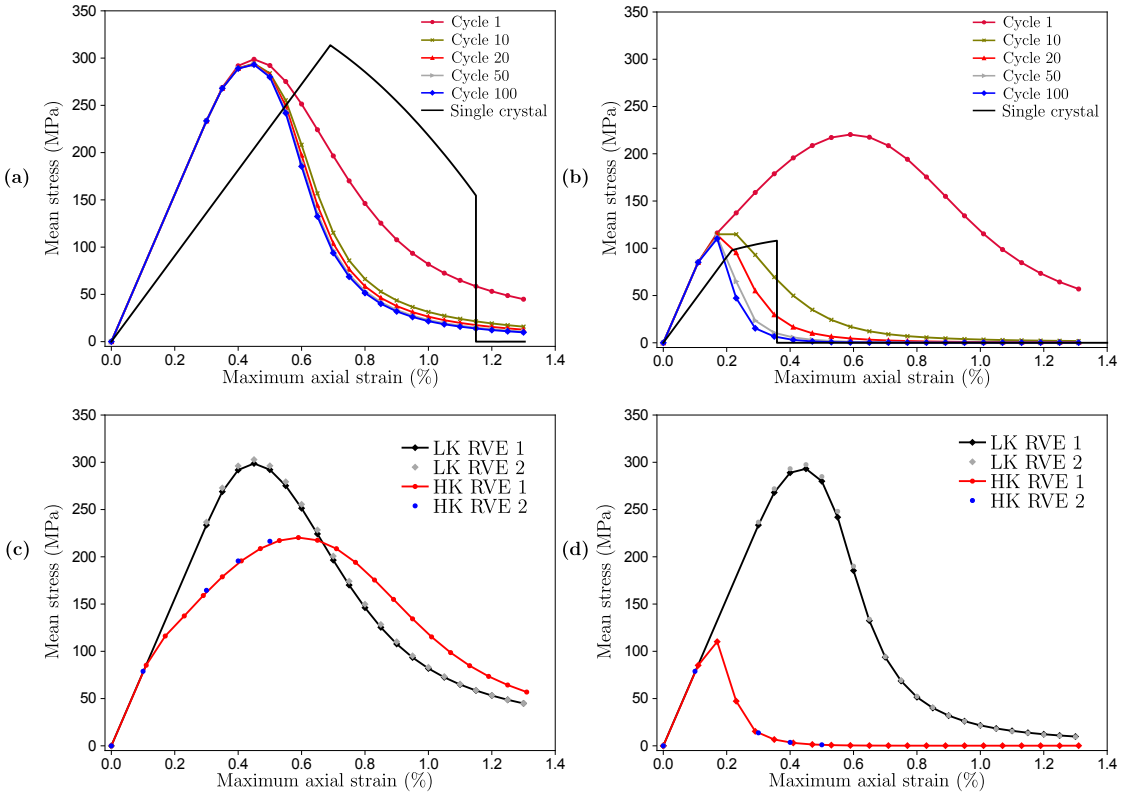

Figure 2.11: Mean stress relaxation in polycrystals (a) VE 1, parameter set LK, (b) VE 1 parameter set HK, (c) comparison of VE 1 and 2 for parameter set LK and HK at cycle 1, (d) comparison of VE 1 and 2 for parameter set LK and HK at cycle 100. Comparison with single crystal response with lattice orientation $< 001 >$, for figures (a) and (b).

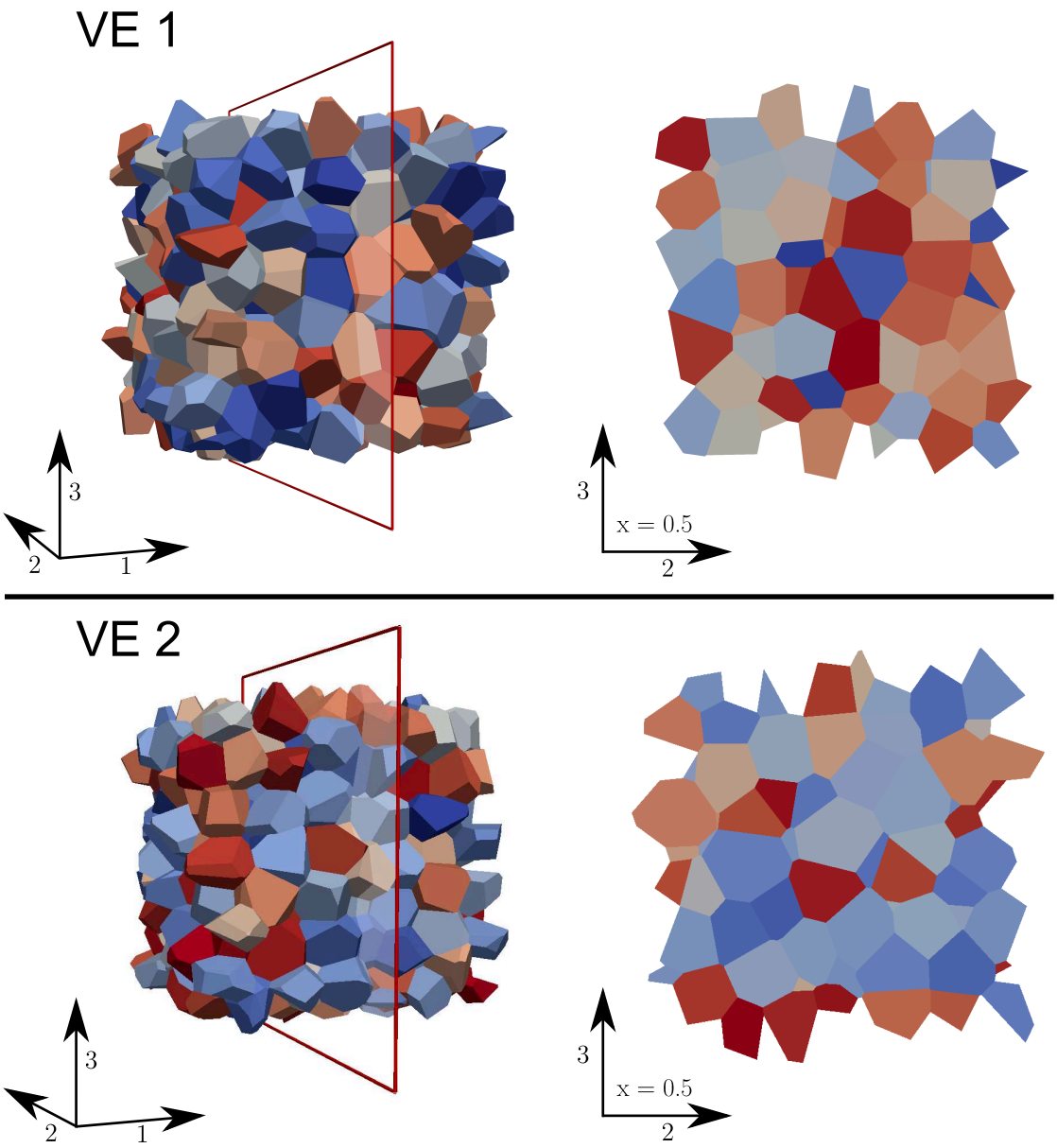

Figure 2.12: A slice of VE 1 and 2 along the 2-3 plane, at x = 0.5

- von Mises strain $\varepsilon_{vM} = \sqrt{\frac{2}{3}\underline{\underline{\varepsilon}}'_{ij}\underline{\underline{\varepsilon}}'_{ij}}$, where $\underline{\underline{\varepsilon}}'$ is the deviatoric part of the local strain tensor,
- equivalent plastic strain $\varepsilon^p_{eq} = \sqrt{\frac{2}{3}\underline{\underline{\varepsilon}}^p_{ij}\underline{\underline{\varepsilon}}^p_{ij}}$
- accumulated plastic strain $\varepsilon_{acc} = \int_0^t \sqrt{\frac{2}{3}\dot{\underline{\underline{\varepsilon}}}_{ij}\dot{\underline{\underline{\varepsilon}}}_{ij}}dt$,
- von Mises stress $\sigma_{vM} = \sqrt{\frac{3}{2}\underline{\underline{\sigma}}'_{ij}\underline{\underline{\sigma}}'_{ij}}$, where $\underline{\underline{\sigma}}'$ is the deviatoric part of the local stress tensor,
- stress triaxiality $\sigma_{tri} = \frac{\underline{\underline{\sigma}}_{ii}/3}{\sqrt{\frac{3}{2}\underline{\underline{\sigma}}'_{ij}\underline{\underline{\sigma}}'_{ij}}}$,
- number of active slip systems: $\left(\sum_{s=1}^{N}|\gamma^s|\right) / \max_{s=1,N}(|\gamma^s|)$, where s is the slip system,
- maximum axial Schmid factor per grain $m_{\max} = \max_{s=1,N}(|m^s|)$, where $m^s = (\underline{n}^s.\underline{t})(\underline{l}^s.\underline{t})$, $\underline{t}$ being the tensile direction and s the slip system. This factor is computed assuming uniaxial tension.
- total axial Schmid factor per grain $m_{total} = \sum_{s=1}^{N}|m^s|$.

For both VEs, the von Mises strain and equivalent plastic strain maps in Fig. 2.13 show that both quantities have very similar maps and it can be seen that they concentrate in some regions of the microstructure. These regions do not specifically conform to any specific grain or orientation. Similar observation is made for the accumulated plastic strain map. One important feature from the accumulated plastic strain map is the extreme heterogeneity with locations experiencing very little plastic strain accumulation, and regions of accumulated plastic activity as high as 55%. Looking at the von Mises stress plot, it can be seen that there is much less heterogeneity, at least when compared to the strain plots. The von Mises stress scale begins at 800 MPa and even at this scale, not many regions can be seen to have such low stresses. Nonetheless, the von Mises stress seems to obey morphological constraints such as grains and grain boundaries, in contrast to other quantities. The same holds for the stress triaxiality plot. The map of the number

of active slip systems is also given in Fig. 2.13. This variable ranges in principle from 1 to 12. However, it can be seen that the estimated number of activated slip systems does not reach such large values but mostly remains between 1 and 3. The plot shows that a value of 1 is observed mostly at the core of the grains where a single slip system is active. On the other hand, darker regions of the active slip system plot exist at the grain boundaries where different grains interact and multislip is likely. Lastly, two plots for the Schmid factors are provided in Fig. 2.13: the maximum axial Schmid factor $m_{\max}$ and the total axial Schmid factor m_{total}. A high value of $m_{\max}$ indicates that the grains are rather soft, meaning that they experience low stress values. No clear correlation can be seen between the $m_{\max}$ map and the previous stress and strain maps. In contrast, interesting observations can be made from the m_{total} map. The variable m_{total} is the sum of all Schmid factors for unixial tensile direction. This quantity, is another indicator of multislip activity. A clear correlation can be seen between the m_{total} map and the field of von Mises stress. Wherever there is a high value of the von Mises stress, m_{total} is low and vice versa.

Observation of local ratcheting phenomena

Up till now the series comparison test to detect ratcheting or shakedown has been applied to the macroscopic averaged results. In this section the test is applied to each element of the finite element mesh in order to detect local ratcheting phenomenon. The elements which ratchet are then displayed in red while those which exhibit shakedown are shown in blue. For the application of this test, three simulations are selected for from the asymmetric stress controlled batch (VE 1, parameter set LK) after running 100 cycles. All three have the same loading ratio of R_Σ = -0.7 while the maximum applied stress varies as follows:

1. Σ_{11} = 849 MPa, macroscopic shakedown, 1.9% of ratcheting volume
2. Σ_{11} = 983 MPa, macroscopic shakedown, 29.0% of ratcheting volume
3. Σ_{11} = 1021 MPa, macroscopic ratcheting, 53.8% of ratcheting volume

Using the series comparison test for ratcheting and shakedown, the first two cases display macroscopic shakedown while the third exhibits macroscopic ratcheting. Figure 2.14 elaborates this further where the three aforementioned cases are shown. The first line shows the whole VE. In the second line of the figure, only the finite

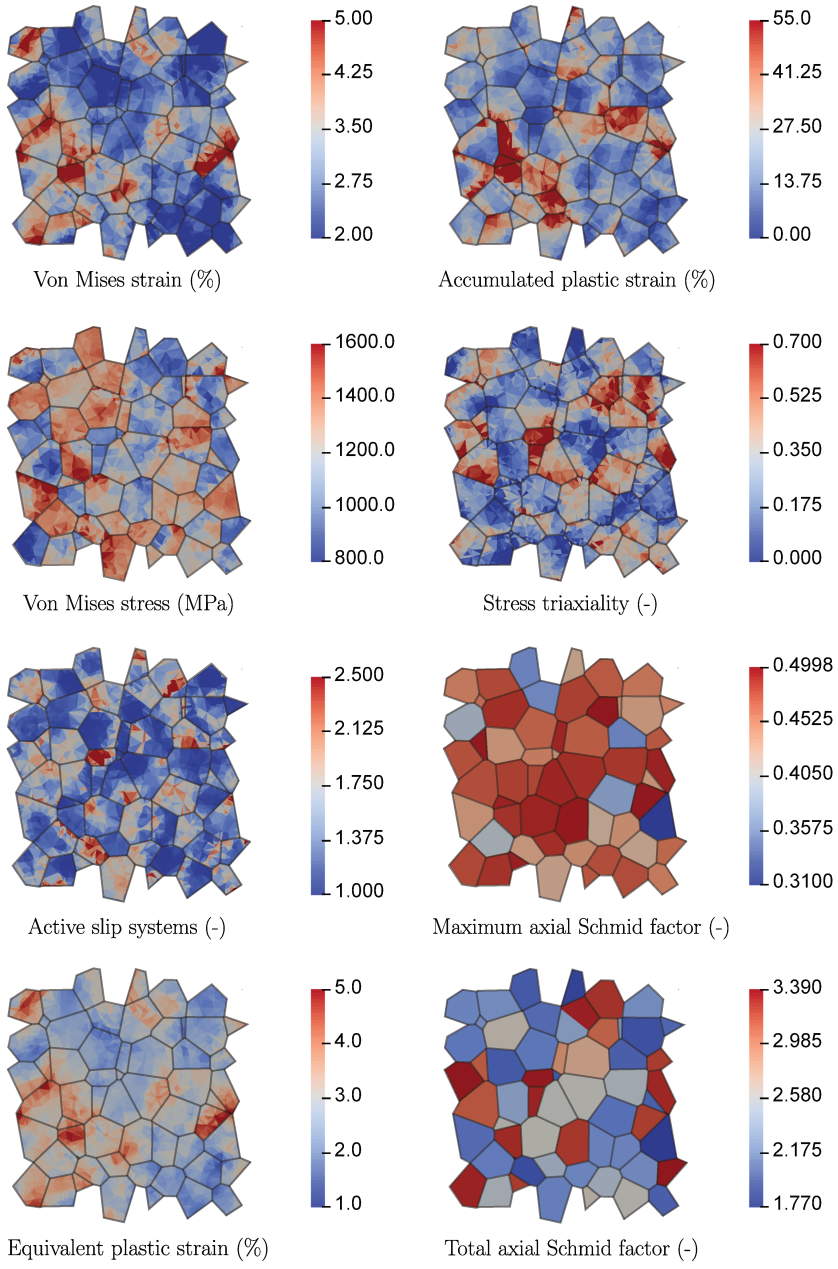

Figure 2.13: (a) For VE 1, contour plots of a simulation with $\Sigma_{11} = 1021$ MPa, and asymmetric load with $R_\Sigma = -0.7$ after running one hundred cycles, extracted at the maximum stress of the one hundredth cycle. The contour plots show the von Mises strain, accumulated plastic strain, von Mises stress, stress triaxaility, maximum slip divided by total slip, and the axial highest Schmid factor, and the total Schmid factor.

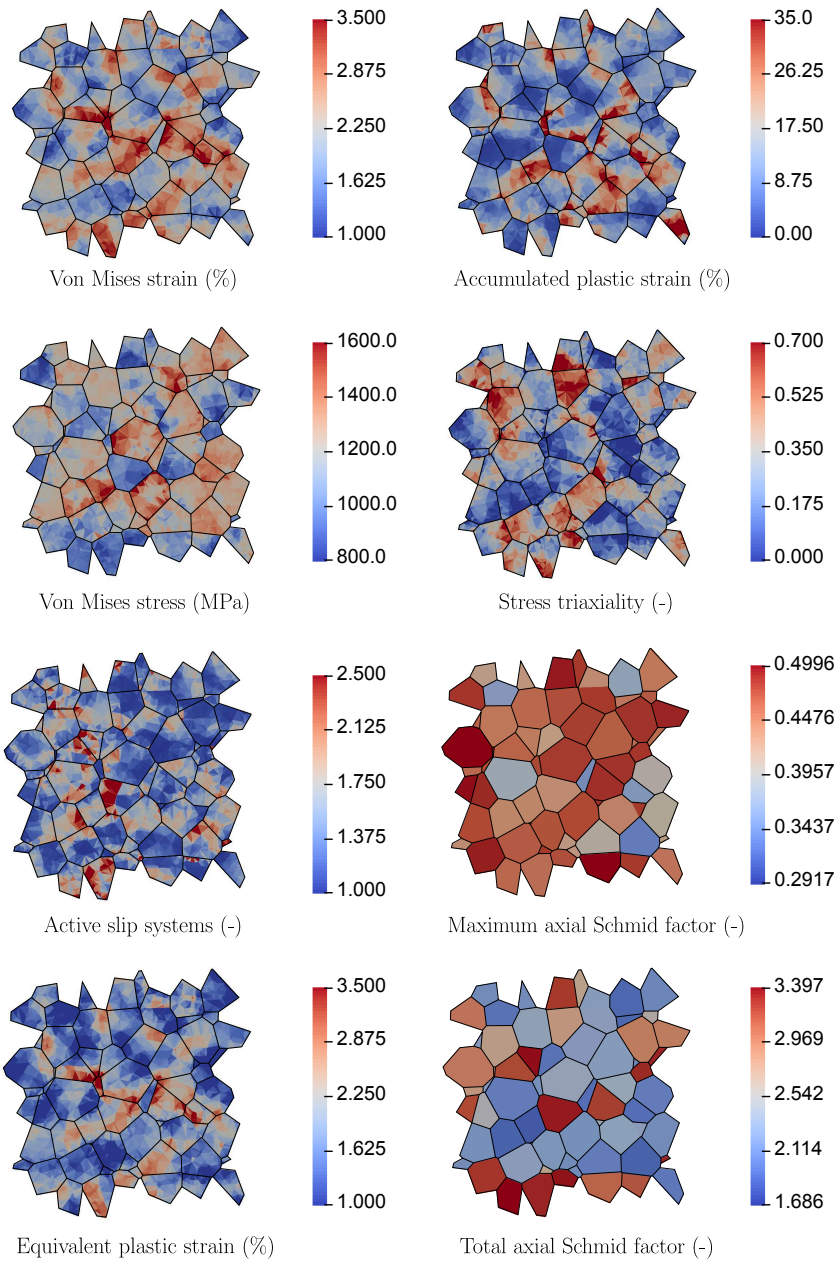

Figure 2.13: (b) For VE 2, contour plots of a simulation with $\Sigma_{11} = 1021$ MPa, and asymmetric load with $R_\Sigma = -0.7$ after running one hundred cycles, extracted at the maximum stress of the one hundredth cycle. The contour plots show the von Mises strain, accumulated plastic strain, von Mises stress, stress triaxaility, maximum slip divided by total slip, and the axial highest Schmid factor, and the total Schmid factor.

elements of the volume which undergo ratcheting can be seen for all three loads. The third line shows a 2D slice with the ratcheting and shakedown regions. It seems that the regions that ratchet do not conform to grain morphology or any particular locations and are rather random in nature.

It can be seen that the ratcheting zones of the polycrystal tend to percolate to form a connected ratcheting domain when increasing the applied stress and before macroscopic ratcheting is observed. The volume fraction of the percolating ratcheting zone has been determined following the method proposed in Kanit et al. (2006) and was found to reach full percolation for the two higher loads illustrated in Fig. 2.14. In contrast, in the left column of Fig. 2.14 for lower load values, isolated islands of ratcheting are observed. No direct link could be derived between the corresponding percolation threshold and the occurrence of plastic shakedown or ratcheting.

Probability density distributions

Figure 2.15 presents Gauss point distribution plots for Σ_{11} = 1021 MPa, and R_Σ = -0.7. Both VEs are considered: The solid line represents VE 1, while the dotted line represents VE 2. To show the evolution of each variable with respect to cycle number, the statistics are collected at the tension peak of cycles 1, 10 and 100. In figure 2.15(a), the histogram plot of von Mises stress shows a multi-modal distribution where the peaks can be seen to progressively split as the number of simulated cycles increases. This point will be analyzed in the next paragraph and in the next two figures. With regards to the accumulated plastic strain according to Fig. 2.15(c), it can be seen that for the first cycle, the distributions are first unimodal but as the cycle number increases, a hump is produced in the left part of the curves. This will be characterized later in this article. Looking at the von Mises strain distribution, it can be seen that, with an increase in the number of cycles, the curves translate along the strain axis, as a result of the ratcheting phenomenon. The standard deviation of von Mises strain is found to increase with the cycle number. Regarding the stress triaxiality, the standard deviation similarly increases with the cycle number. Lastly, the number of active slip systems can be seen to be less than six and with the progression of cycles, single slip starts to dominate. The representativity of the results is confirmed by the fact that all the dotted and solid lines corresponding to VE 1 and 2 are close to each other. An exception is the von Mises strain distribution plots for which slight deviations are observed, which shows a slightly different ratcheting intensity of each volume. The intensity of ratcheting surely is a very sensitive result of polycrystalline material

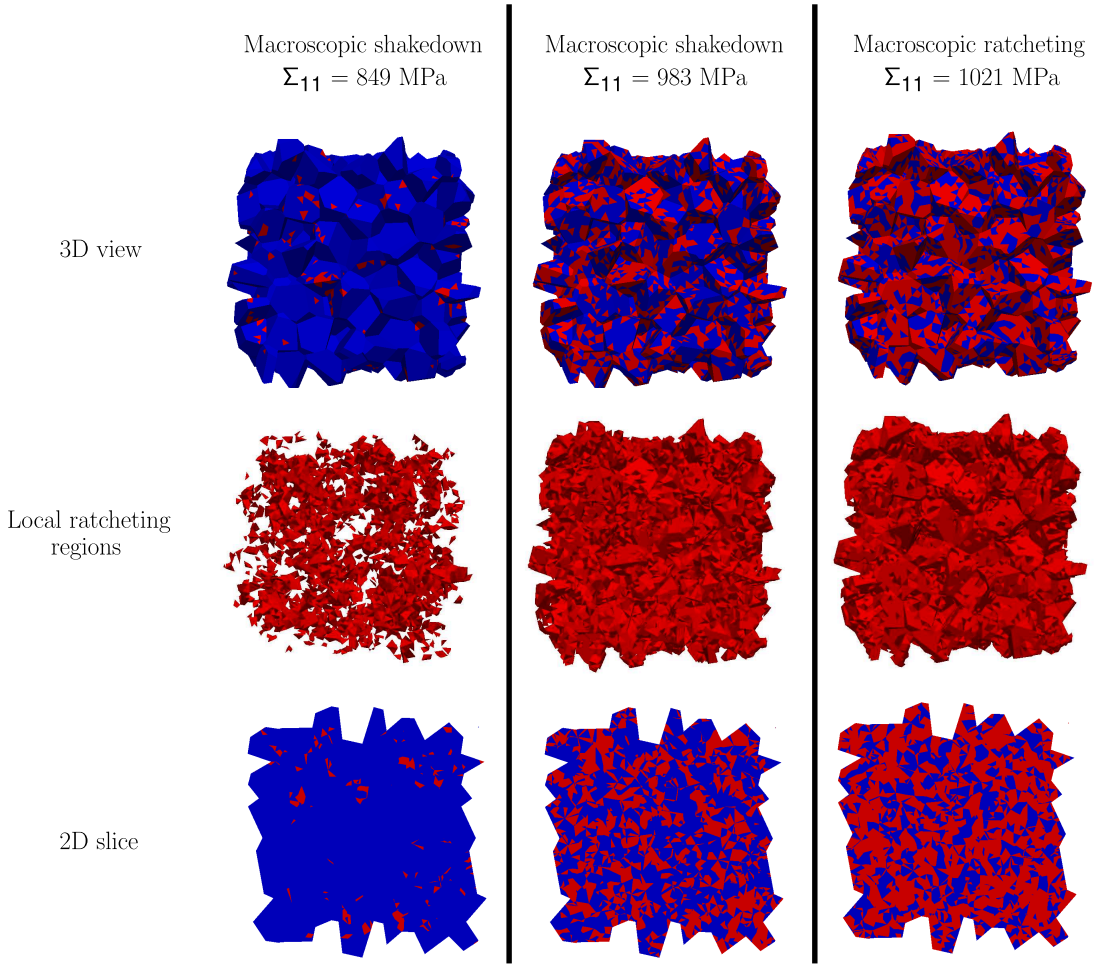

Figure 2.14: Three different asymmetric stress controlled simulations with Σ_{11} = 849 MPa, Σ_{11} = 983 MPa, and Σ_{11} = 1021 MPa, and R_Σ = -0.7 for all cases (VE 1, parameter set LK). Macroscopically, the first and second shakedown while the third ratchets. Local regions for ratcheting and shakedown (per finite element) are respectively shown in red and blue for each case.

response. More precise estimates would require the consideration of additional volume elements.

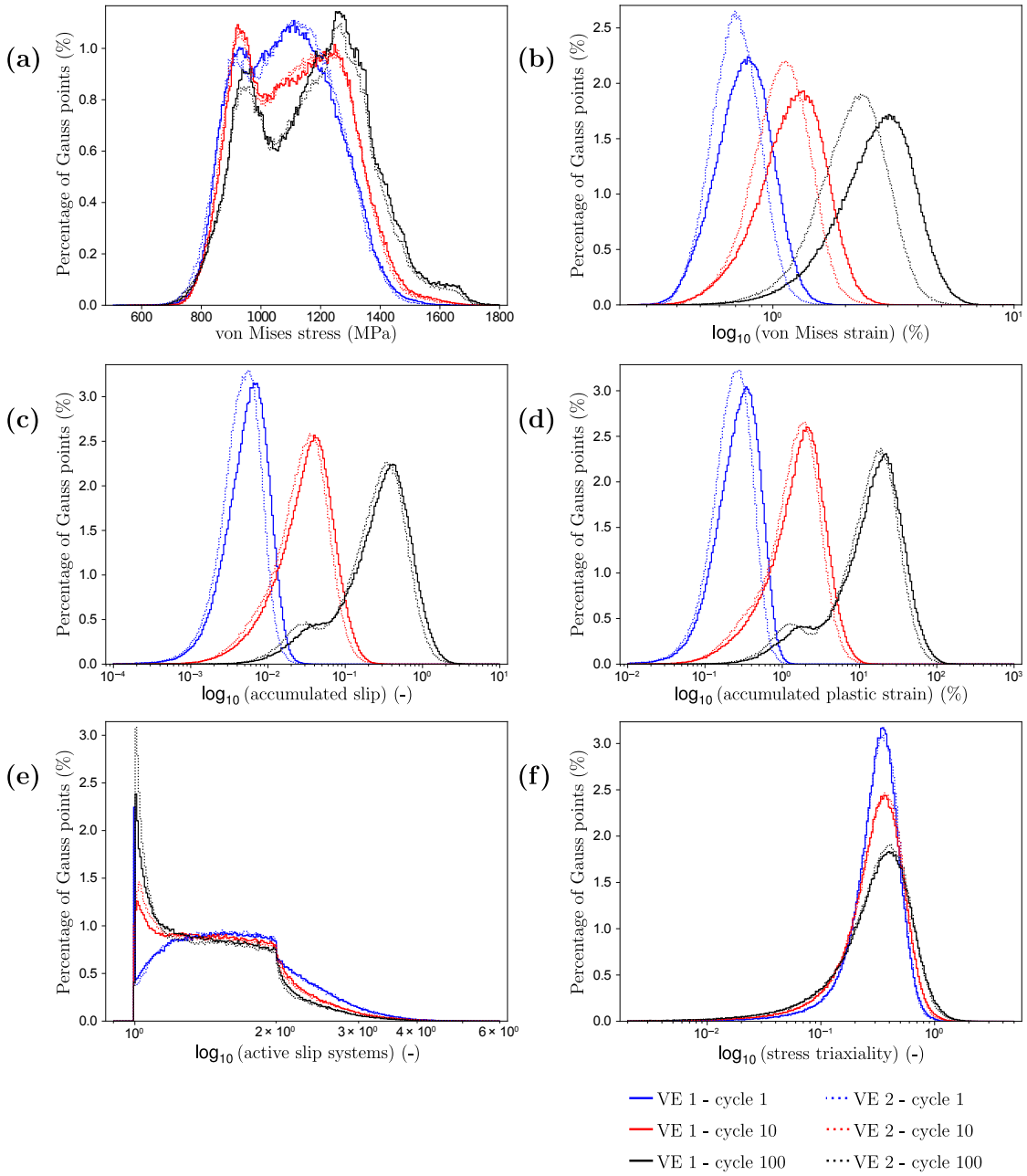

Figure 2.15: Distribution curves of Gauss point variables for an asymmetric stress controlled test using parameter set 1, R_Σ = -0.7 and Σ_{11} = 1021 MPa. The variables shown are (a) von Mises stress (b) von Mises strain, (c) accumulated slip, (d) accumulated plastic strain, and (e) stress triaxiality.

Evidence of bimodal stress distribution

As seen in figure 2.15, the von Mises stress probability distribution curves exhibit a multimodal distribution. This fact has already been observed by several authors using crystal plasticity simulations (Osipov et al., 2008; Schwartz et al., 2013; Lee et al., 2011; Choi et al., 2012). What is missing is a detailed analysis showing the origin of this phenomenon. Figure 2.16 shows the von Mises stress distribution curve taken at the tensile peak of the 100th cycle for Σ_{11} = 1021 MPa and R_Σ = -0.7. Two distinct peaks can be seen in the distribution arbitrarily separated by a dashed line. This separation makes it possible to split the polycrystalline volume into two parts, the first (resp. second) one containing the Gauss point displaying a von Mises equivalent stress lower (resp. larger) than this separation value. The volume fractions in each peak are then shown in the 3D and 2D views of Fig. 2.16, with a gray (resp. black) color corresponding to the first (resp. second) peak. It can be noted that the black and grey regions contain mostly full grains, i.e. each grain is either completely black or grey. Of course there are some exceptions where some grains are split into grey and black zones. They reflect the fact that the distribution curve of von Mises stress was split arbitrarily and the region between the two black dotted lines in the histogram of figure 2.16 has overlapping points. The observation of the total axial Schmid factors plot of figure 2.13 indicates that the black regions correspond to hard grains, and the grey regions correspond to soft grains. It is concluded that the polycrystal aggregate progressively splits into main regions of high and low stresses strongly correlated with the hard/soft character of the grains.

Evidence of bimodal accumulated plastic strain distribution

Bimodality is also observed in the distribution of accumulated plastic strain or accumulated slip in figure 2.15(c,d), when the number of simulated cycles increases. This is not always the case. Figure 2.17 shows the Gauss point results from five simulations. These simulations pertain to parameter set HK, Σ_{11} = 284, 368, 452, 536, 620 MPa, and $R_\Sigma = 0$. The trend that can be seen in log accumulated plastic strain plot distribution curves of these plots is that the first and last plots (Σ_{11} = 284 and 620 MPa) are unimodal regardless of the number of simulated cycles while the other three plots start with one peak and then split into two peaks. This bimodality represents two regions that develop inside the polycrystal: a first where shakedown occurs and the second where ratcheting takes place. It can also be seen that the volume of these regions depends on the applied load.

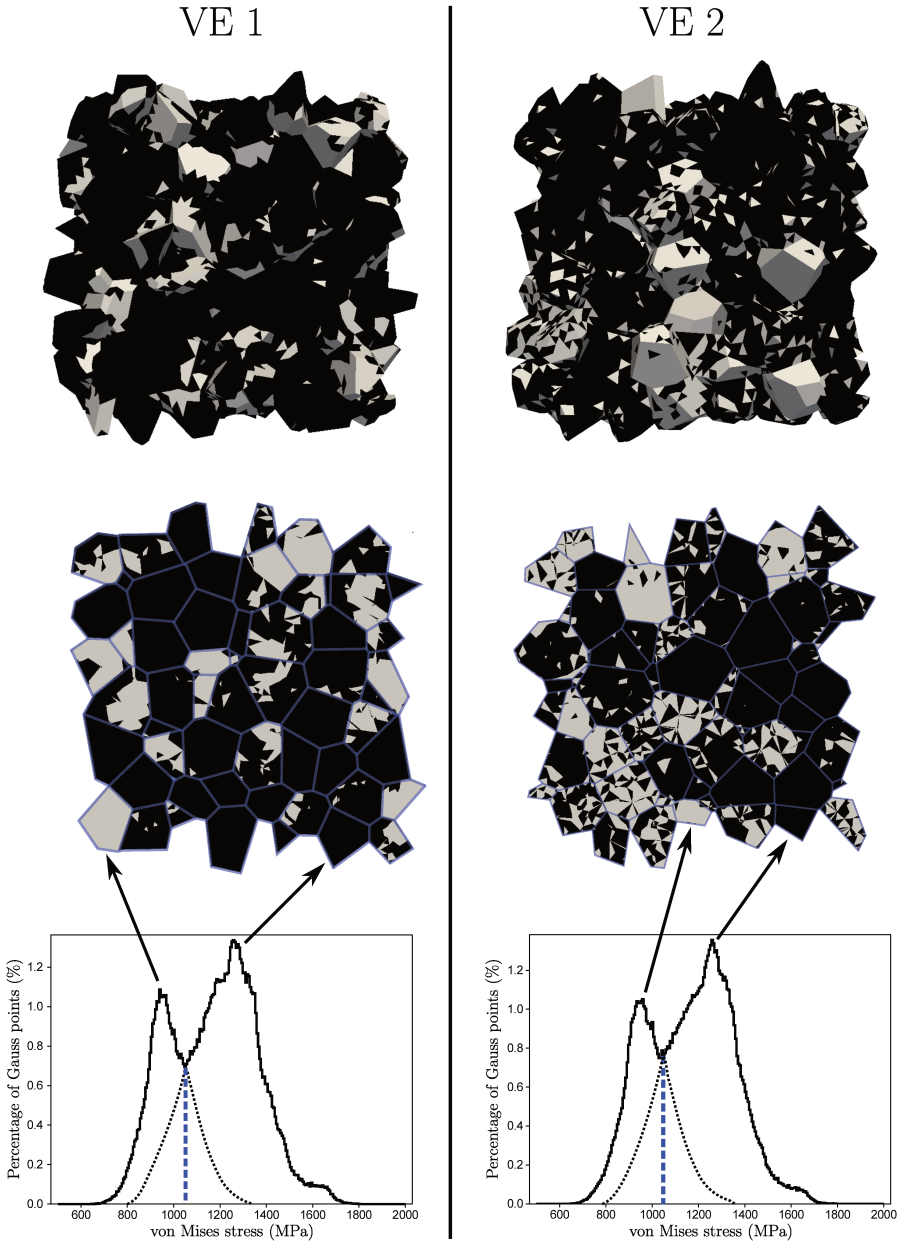

Figure 2.16: For both VE 1 and 2, von Mises stress distribution at the tensile peak of the 100th cycle for Σ_{11} = 1021 MPa and R_Σ = -0.7. The distribution curve has been broken down into two parts and the associated regions are shown in the microstructure respectively. All Gauss points in the first part of the distribution curve are colored gray in the microstructure, while all Gauss points in the second part of the distribution curve are colored black.

Most importantly, it is noted that this bimodality does not always appear. It is therefore possible to draw a diagram of the existence of bimodal accumulated plastic strain distribution depending on the applied stress amplitude and mean stress. This is done in Fig. 2.18 taking the already performed simulations for VE 1 and parameter set HK. The obtained modality diagram of Fig. 2.18 can be compared to the ratcheting diagram of Fig. 2.6 based on the series criterion. It is remarkable that the domain of bimodality is found to almost coincide with the domain of plastic shakedown. This major finding suggests that stable bimodal plastic strain distributions correspond to a transition regime between shakedown (elastic or plastic) and ratcheting material response. This feature can be also be used as a criterion for the detection of plastic shakedown replacing or in addition to the series convergence criterion. This conclusion is confirmed by the results of VE 2 (modality map not provided here for conciseness).

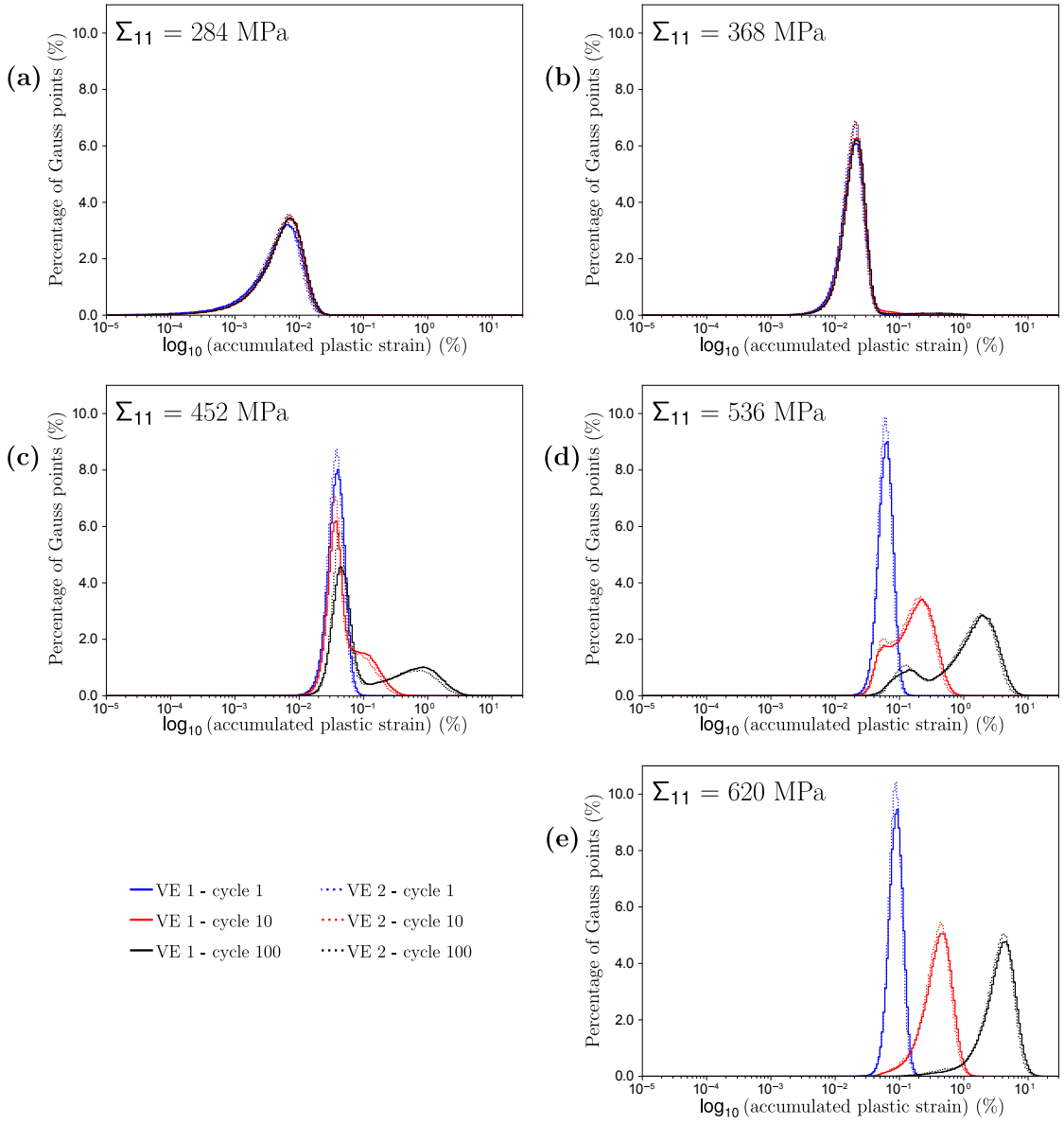

Figure 2.17: Probability distribution curves for the accumulated plastic strain in five simulations with $R_\Sigma = 0$ and $\Sigma_{11} = 284$ - 620 MPa, using parameter set HK.

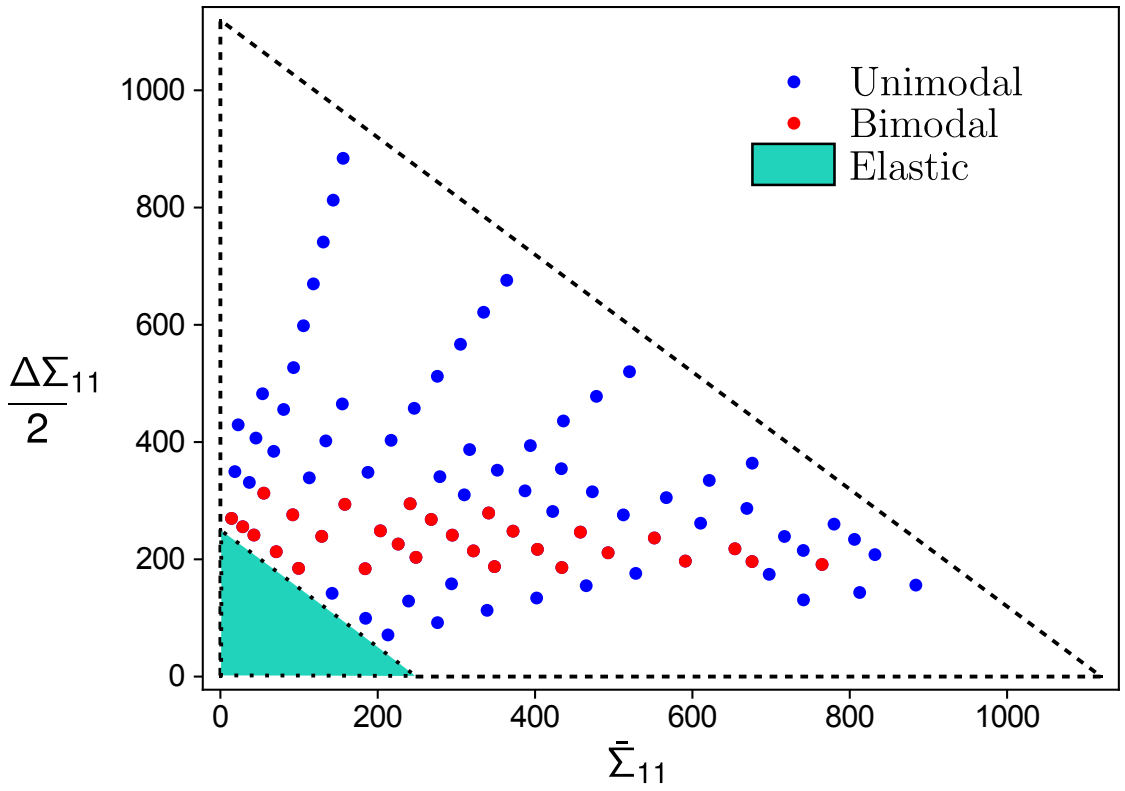

Figure 2.18: Modality diagram for parameter set HK, VE 1. It characterizes the existence of unimodal or bimodal distributions of accumulated plastic strain. All values are in MPa

2.5.2 Mean stress relaxation

The analysis of the local results must also be performed for other loading conditions. Such an analysis is performed in this section in the case of strain controlled tests in order to characterize some microstructural features associated with mean stress relaxation. For the next three figures a strain controlled simulation for VE 1 with parameter set LK and R_E = -0.2 and $E_{11} = 0.85\%$ is considered. The results plotted pertain to the tensile peak of the 100th cycle. The contour plots of figure 2.19 can be compared with those of figure 2.13 (a) (stress controlled compared to strain controlled). It can be seen that both are very similar. In particular, the map of the von Mises strain shows that the most deformed grains are almost the same for both simulations, except that the strain controlled simulation leads to much lower strain values. The following definition of a local mean stress is proposed:

$$((\sigma_{11}^t + \sigma_{22}^t + \sigma_{33}^t) + (\sigma_{11}^c + \sigma_{22}^c + \sigma_{33}^c))/2 \tag{2.35}$$

where the subscripts t ans c indicate that the variables were collected at the macroscopic tensile or compressive peak of their cycle. The observation of the mean stress plot indicates that it concentrates at the grain boundaries or at triple junctions, and is less prone to be high within the grains. It is hypothesized that this intergranular interaction prevents the mean stress from relaxing to zero in a polycrystal.

Next, in table 2.3 a quantitative analysis of the interdependence of some constitutive variables is done using the Pearson correlation coefficient (ρ[1]) (Rodgers and Nicewander, 1988). This table is symmetric and only the upper half is presented while labeling the lower half as "sym". The values of this coefficient range from -1 (negatively correlated) to +1 (positively correlated), where attention should be paid to the magnitude of the coefficient; a high magnitude signifies correlation while low means no linear correlation. Also, figure 2.20 shows six selected scatter plots for the relationship between these variables. Judging from these results, the mean stress is strongly related to the stress triaxiality ($\rho = 0.73$) which is also, to some extent, visible in the contour plots of figure 2.19. It can be argued that this interdependence is because both quantities are stress measures, but this argument is not valid when σ_{vM} is compared to σ_{mean} which gives a very weak interdependence (ρ = -0.08). When comparing the von Mises stress with the maximum axial Schmid and the total axial Schmid factor, a strong negative relationship can be seen for both quantities but m_{total} is dominant (ρ = -0.69) which postulates

[1] $\rho_{X,Y} = \frac{cov(X,Y)}{S_X S_Y}$ where cov is the covariance between two random variables X and Y, S_X is the standard deviation of X, and S_Y is the standard deviation of Y.

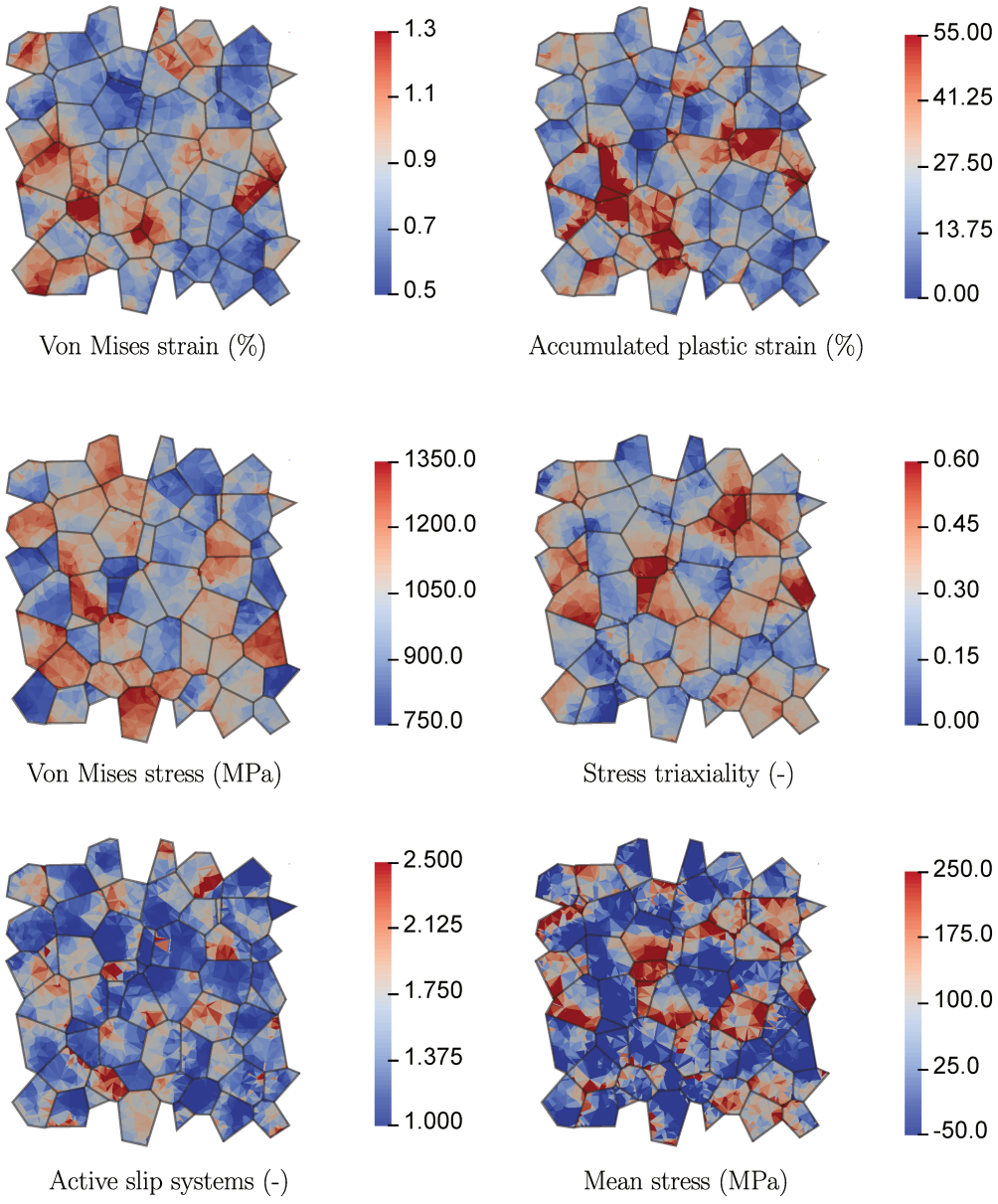

Figure 2.19: Contour plots of a simulation with asymmetric strain of $E_{11} = 0.85\%$ and $R_E = -0.2$ after running one hundred cycles, extracted at the maximum strain of the one hundredth cycle (VE 1, parameter set LK). The contour plots show the von Mises strain, accumulated plastic strain, von Mises stress, stress triaxaility, maximum slip divided by total slip, and the local mean stress.

that slip does not just depend on the softest slip system, rather it depends on the combination of multiple slip systems. The triaxial stress is weakly negatively correlated to the von Mises stress (ρ = -0.31) which to some extent makes sense because both quantities are stress measures and they must have a mutual dependence. The strongest relationship of all variables is of the von Mises strain with the accumulated plastic strain ($\rho = 0.70$), which is also obvious from the contour plots.

	σ_{mean}	σ_{vM}	σ_{tri}	ε_{vM}	ε^{p}_{acc}	$m_{\max}$	m_{total}
σ_{mean}	1.00	-0.08	0.73	-0.14	-0.13	0.00	-0.01
σ_{vM}	sym	1.00	-0.31	-0.03	0.38	-0.41	-0.69
σ_{tri}	sym	sym	1.00	-0.07	-0.12	0.11	0.18
ε_{vM}	sym	sym	sym	1.00	0.70	0.32	0.40
ε^{p}_{acc}	sym	sym	sym	sym	1.00	0.16	-0.08
$m_{\max}$	sym	sym	sym	sym	sym	1.00	0.62
m_{total}	sym	sym	sym	sym	sym	sym	1.00

Table 2.3: Pearson correlation coefficient matrix for a simulation with $E_{11} = 0.85\%$ and $R_E = -0.2$ after running one hundred cycles, extracted at the maximum strain of the one hundredth cycle.

It is well documented in literature that tensile mean stress decreases fatigue life by increasing crack openings, whereas compressive mean stress inhibits fatigue cracks because of the contrary (Morrow et al., 1974; Kwofie and Chandler, 2001; Christ et al., 1997; Xia et al., 1996; Yuan et al., 2016). This is nonetheless a hypothesis and is better explored in figure 2.19 which shows the interdependence of different variables especially the mean stress, using scatter plots, for the same simulation. Because the number of points is huge (0.5 million), to avoid clutter only 8000 points are shown in the scatter plot. The plot for mean stress vs stress triaxiality in figure 2.20 (c), shows a high correlation but this result is trivial because both quantities are stress measures and are bound to give such a result. On the other hand, rather curiously, as seen in (a) the von Mises stress does not correlate to the mean stress. Another interesting finding is that as seen in (b), von Mises stress and von Mises strain do not have a direct correlation, pointing to the notion that highly stressed regions need not necessarily have high strains. Similar findings have been reported for the scatter plot between stress and strain inside the polycrystal using finite element crystal plasticity by Flipon et al. (2019) signifying that the scatter plot, although seeming uncorrelated to the naked eye, has in fact some underlying physical reason behind it, and it might be interesting to work on why such a relationship exists. The Pearson correlation coeffecient

fails to see a connection because it only gives linear correlations among different variables. Next, the von Mises strain and the accumulated plastic strain are highly correlated; this of course signifies that the regions which are highly strained will produce the most plasticity but it also points to the fact that the instantaneous value of the strain tensor is highly (but not completely) correlated to the plasticity which has been accumulated up to this point. It may be interesting to find the regions in which the remaining plasticity has dissipated.

The distribution curves for Gauss point variables are plotted in figure 2.21. The solid lines represent VE 1 while dotted lines represent VE 2. Both VEs exhibit a matching response which signifies good representativity of the material. The von Mises stress plot shows the distributions curves translating back on the stress axis which reflects the decrease of the average mean stress per cycle. Again, multimodality is observed for the strain based loading conditions as it was observed for stress control in the previous section with regards to ratcheting. Von Mises strain and stress triaxiality plots display somewhat similar distributions. The plot of the number of active slips systems indicates that single slip gets more dominant as the number of cycles increases. Accumulated slip and accumulated plastic strain exhibit bimodal distributions as in the stress controlled case. The next figure sheds some light on the development of bimodality in the context of mean stress relaxation test. Figure 2.22 shows the breakdown of bimodality in accumulated plastic strain for parameter set LK, VE 1 and 2. It can be seen that for the first two cases (a) and (b), the curves start as a unimodal distribution but then split into bimodal distributions. Just like in the stress controlled case, these curves indicate that a hundred cycles are not enough to reach a saturated response, as the bimodal peaks are still splitting. The two peaks that form imply that the microstructure splits into two regions, one in which plastic activity stops after some cycles (the first stagnant peak), and the other accommodating all plastic deformation (the second peak which keeps moving forward). At high strains, as shown in figure 2.22 (d), the whole microstructure undergoes plastic activity resulting in a unimodal distribution. It is hypothesized from the present observations that when the plasticity distribution becomes unimodal, mean stress will relax to zero.

2.6 Simulations at high cycle numbers

The previous observations have been made from the hundred cycle response of the polycrystalline aggregates. The objective of this last section is to check the validity of the drawn conclusions at higher cycle numbers. Using crystal plasticity

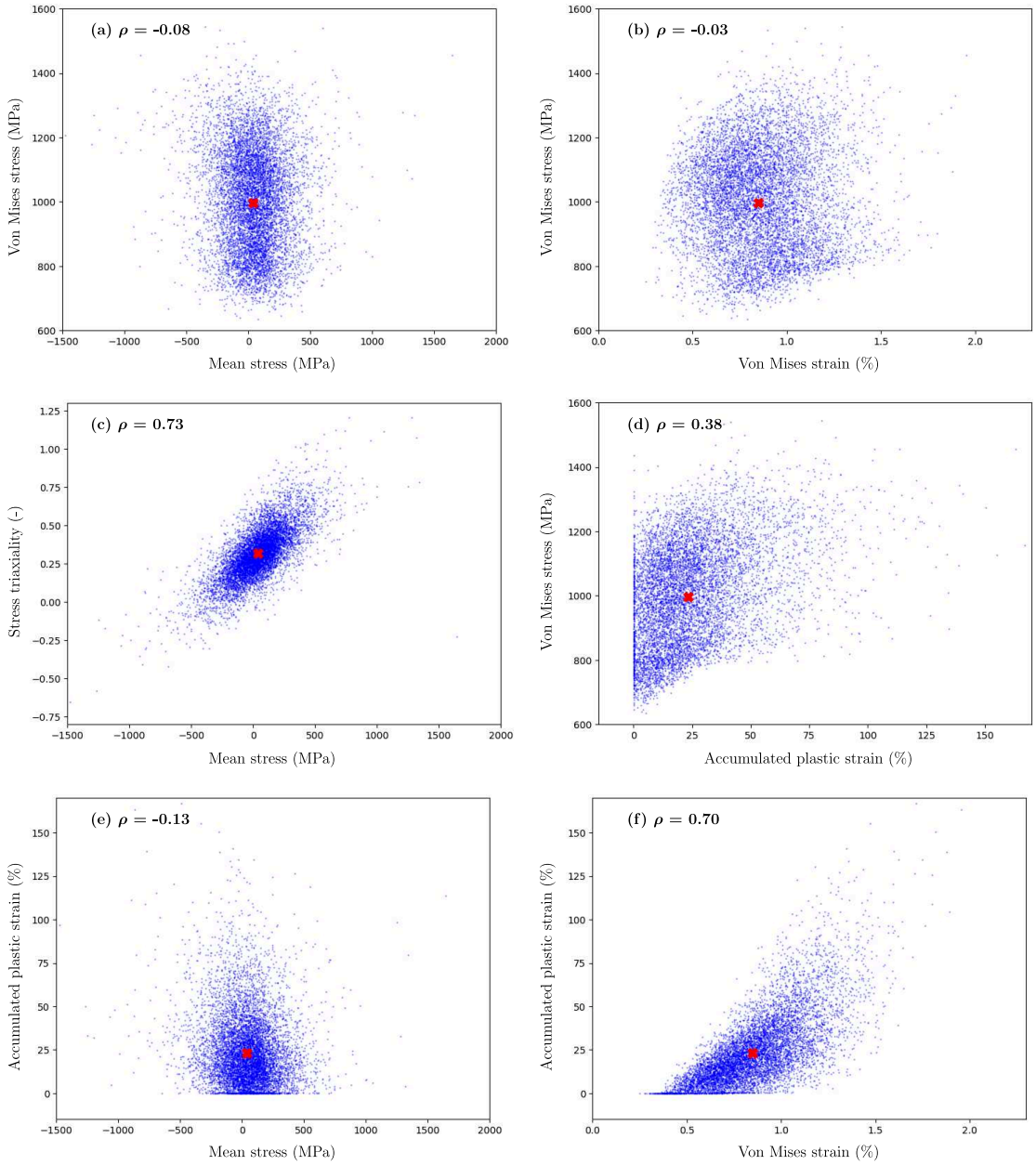

Figure 2.20: Scatter plots of Gauss point variables for an asymmetric strain controlled test using parameter set LK and VE 1, R_E = -0.2 and E_{11} = 0.85%. The variables shown are (a) von Mises stress vs mean stress, (b) von Mises stress vs von Mises strain, (c) stress triaxiality vs mean stress, (d) von Mises stress vs accumulated plastic strain, (e) accumulated plastic strain vs mean stress, and (f) accumulated plastic strain vs von Mises strain. Each plot also shows the average macroscopic value of the variables with a red cross. The Pearson correlation coefficient (ρ) is also stated for each scatter plot.

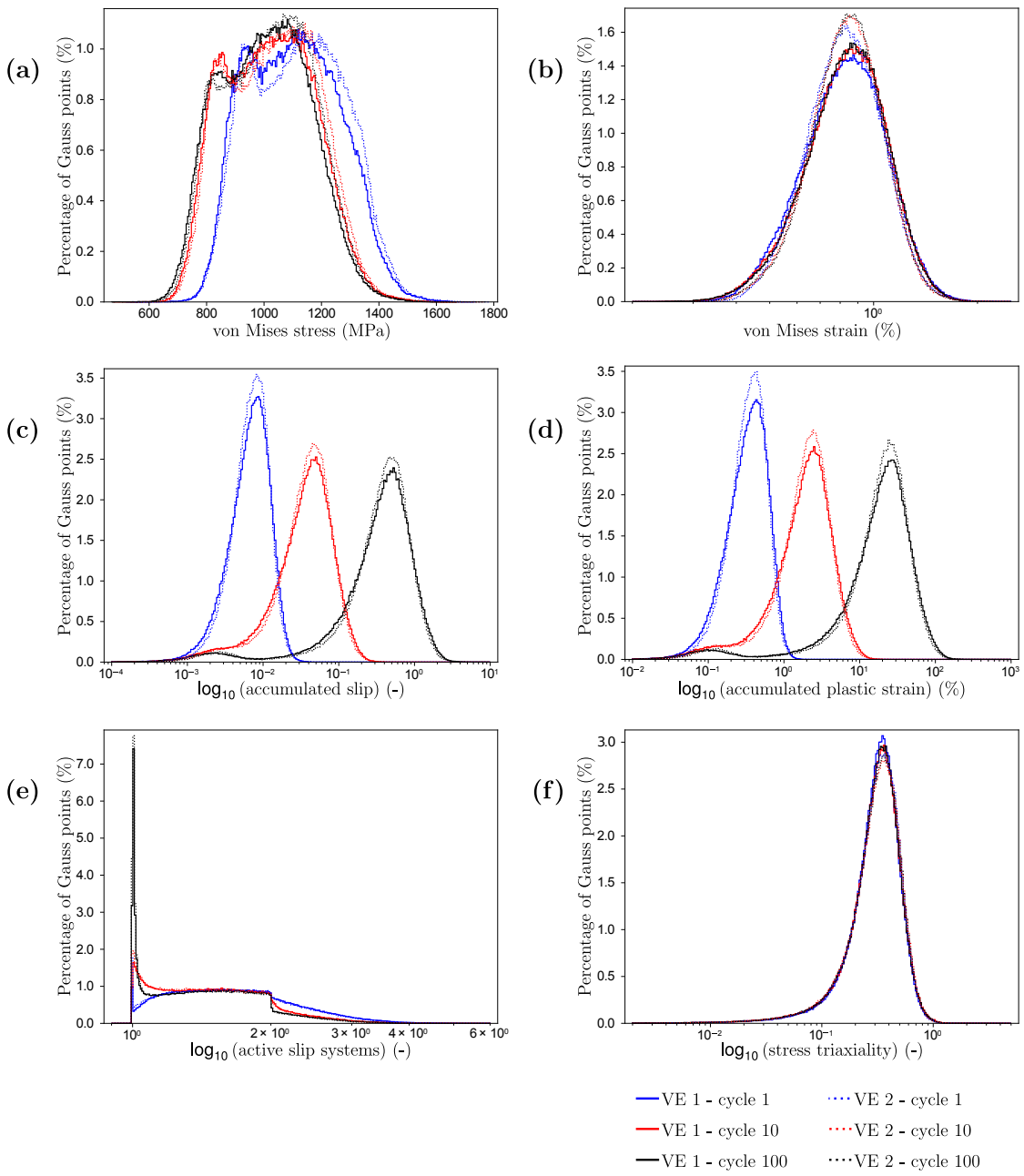

Figure 2.21: Distribution curves of Gauss point variables for an asymmetric strain controlled test using parameter set LK, R_E = -0.2 and $E_{11} = 0.85\%$. The variables shown are (a) von Mises stress (b) von Mises strain, (c) accumulated slip, (d) accumulated plastic strain, and (e) stress triaxiality.

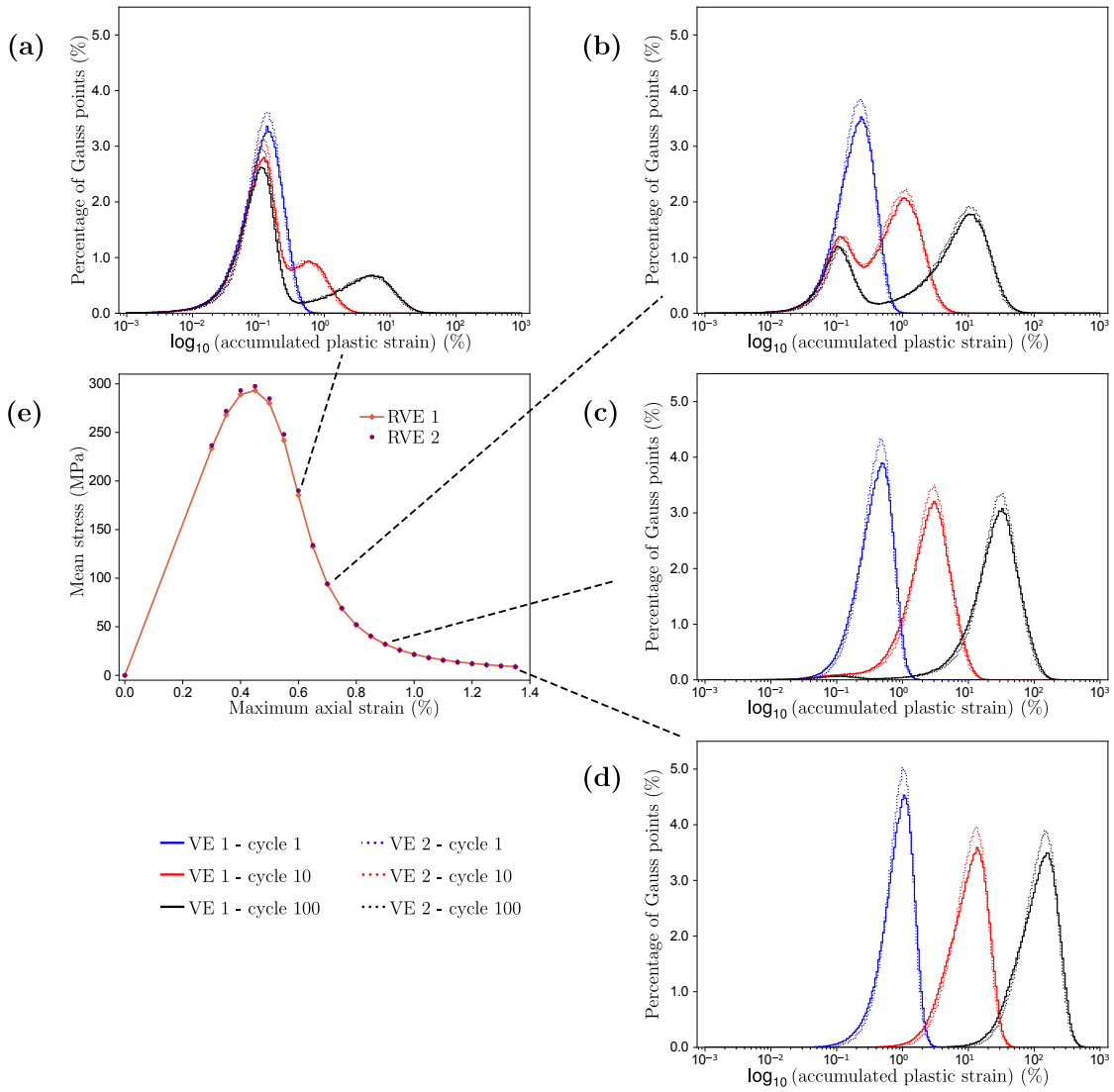

Figure 2.22: For VE 1 and 2, parameter set LK, distribution curves for the accumulated plastic strain per Gauss point for four maximum axial strain values. (a), (b) and (c) show a bimodal while (d) shows a unimodal distribution. (e) gives the mean stress for different maximum axial strains at cycle 100.

for low cycle fatigue, some authors have already simulated thousands of cycles (Joseph et al., 2010; Zhang et al., 2015), but the results provided here for the first time pertain to a finely meshed polycrystal aggregate under asymmetric loading conditions. The mesh is fine enough to provide detailed distribution of local stress and strain fields as illustrated in the previous sections. For instance the present finite element meshes contain almost 600000 degrees of freedom (DOFs) for 300 grains to be compared with 150000 d.o.f. and 250 grains considered by Colas et al. (2019) where more than 1000 cycles were simulated. Two cases are reported in this section where the first case pertains to one simulation on VE 1 under asymmetric strain controlled periodic boundary conditions with R_E = -0.2, and E_{11} = 0.7 % run for 1500 cycles. Fig. 2.23 (a) and (b) illustrate the global mean stress relaxation over the 1500 cycles. It can be seen that the cyclic mean stress does not relax to zero even after 1500 cycles, and seems to have reached a saturated value signified by the saturating curve of mean stress in (b). The accumulated plastic strain plot of Fig. 2.23 (c) further confirms the bimodal distribution with one part of the aggregate experiencing further plastic activity whereas the first peak corresponds to an elastically accommodated region of the crystal. The same trend was observed after 100 cycles and is continuing further after 1500 cycles.

It is instructive to compare the obtained results with a simulation involving a larger number of grains at the expense of a coarse mesh. The objective is to confirm the representativity of the presented results even though this feature was supported by the consideration of VE 1 and 2. A new VE with $15^3 = 3375$ grains and with one single hexahedral quadratic element per grain is generated, see Fig. 2.24(a). Using parameter set LK, asymmetric periodic strain loading of 0.6% and R_E = -0.2 is imposed. The simulation is run for 6000 cycles. Fig. 2.24(b) shows the macroscopic stress strain response while (c) shows the accumulated plastic strain at the first, hundredth and six thousandth cycles. It can be seen that the macroscopic stress strain response does not change from the hundredth to the thousandth cycle but the accumulated slip has the same bimodal response as observed in the previous simulations. Just as before, the microstructure divides into two distinct regions: one that stops accumulating plasticity, and the other which takes all the plastic deformation indicating that these results are consistent with the study presented in this chapter.

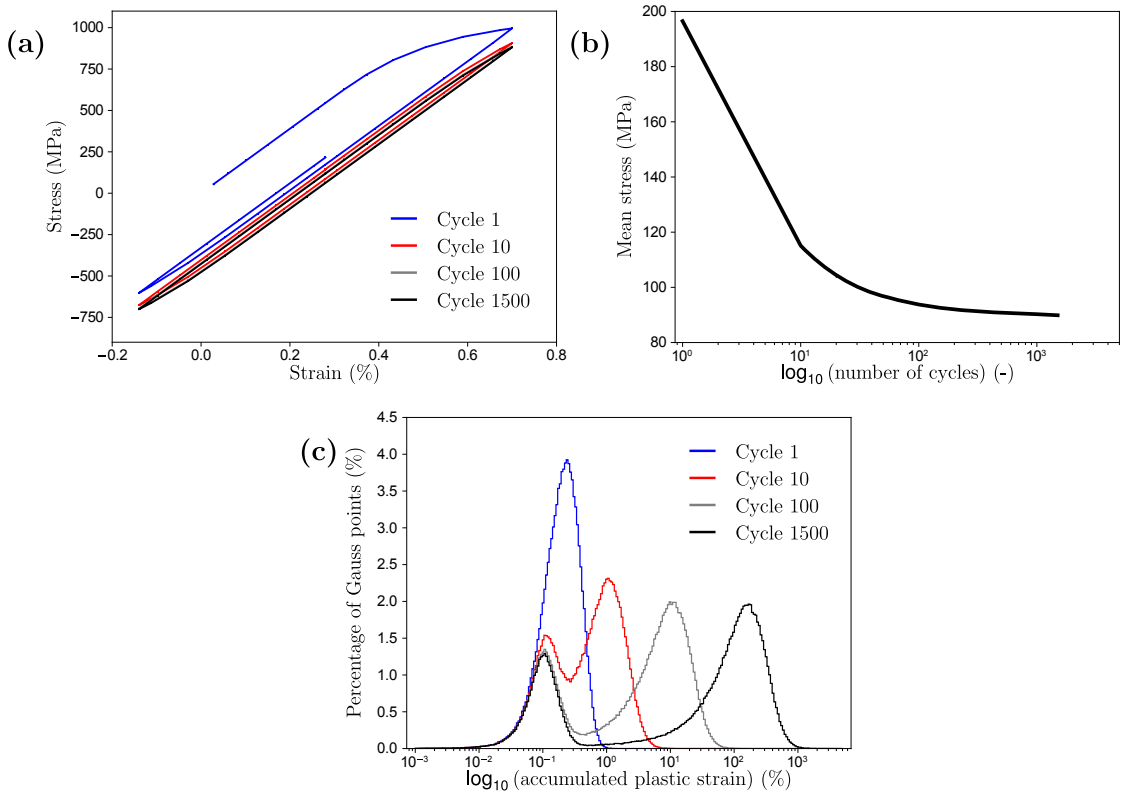

Figure 2.23: Long cyclic simulation with asymmetric strain controlled boundary conditions for VE 1, parameter set LK: E_{11} = 0.7 %, R_E = -0.2. (a) The stress strain hysteresis loops for cycles 1, 10, 100 and 1500. (b) Macroscopic mean stress plotted against the number of cycles. (c) Gauss point distribution of the accumulated plastic strain for different cycles.

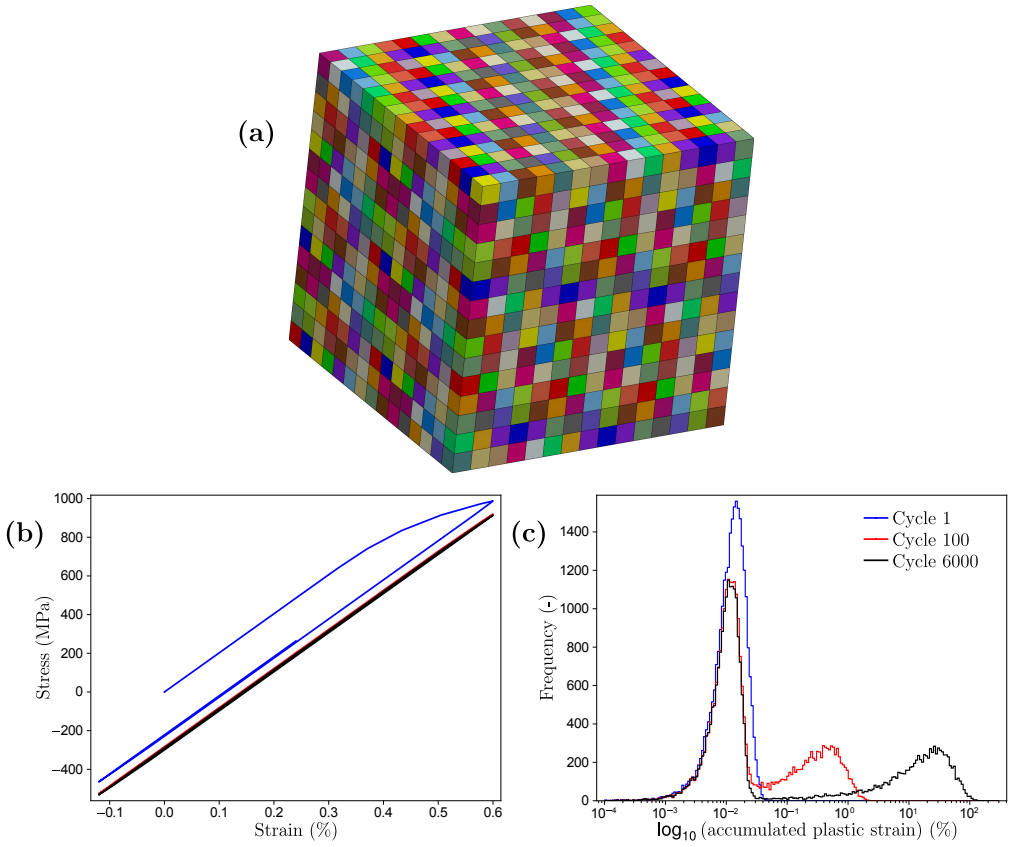

Figure 2.24: Using asymmetric strain controlled boundary conditions, with E_{11} = 0.6% and R_E = -0.2 and parameter set LK: (a) a coarse meshed volume element with 3375 grains and one quadratic element per grain, (b) The macroscopic stress vs strain loops for cycles 1, 100 and 6000. (c) Accumulated plastic strain after the three cyclic instances.

2.7 Discussion

The motivation behind this article was to present the capabilities of the crystal plasticity model to reproduce asymmetric cyclic responses of engineering metallic materials. The phenomenon behind complex behavior was studied numerically and links to the mechanics behind them were established. The idea was not to match macroscopic curves but to represent that the different zones produced in asymmetric cyclic experimental tests i.e. ratcheting, elastic shakedown, plastic shakedown, and a complete or incomplete mean stress relaxation are obtainable with the model.

In context to asymmetric stress controlled simulations, figure 2.6 presented different cyclic regimes experienced by polycrystals. These regimes i.e. ratcheting, plastic shakedown and elastic shakedown, depend on the applied stress amplitude and mean stress. For 316 stainless steel Pellissier-Tanon et al. (1982) have presented experimental evidence for plastic shakedown and ratcheting. Similarly, with an increasing mean stress, Park et al. (2007) presents experimental data for ratcheting in Inconel 718, and Lim et al. (2009); Das and Chakraborti (2011) for ratcheting in copper. For 316 and 304 steels, an important discovery by Goodman (1984); Taleb and Keller (2018) was that increasing the stress amplitude under a constant non-zero mean stress or increasing the applied mean stress under a given stress amplitude, both increase the rate of ratcheting. Figure 2.6 in the present article numerically characterizes these complex cyclic phenomena and gives an insight of how a little variation in the applied stress can result in a switch between shakedown or ratcheting. Of course, no explicit experimental comparisons were been done but from the aforementioned literature sources it can be anticipated that using the present model such mechanical regimes are reproducible.

In contrast, under asymmetric strain controlled loadings, depending on the applied strain amplitude, experiments usually present a non-zero cyclic mean stress. For Inconel 718, this has been demonstrated experimentally by Prithivirajan and Sangid (2018); Gribbin et al. (2016) whereas for steels Wehner and Fatemi (1991); Nikulin et al. (2019) have shown such behaviour. In compliment, asymmetric strain controlled experiments show that the mean stress relaxes to progressively lower values with an increasing strain amplitude as shown for Inconel 718 by Chaboche et al. (2012) and aluminum by Hao et al. (2015). Figures 2.10 and 2.11 showed a qualitative replication of such behaviors where increasing the applied strain amplitude, the mean stress smoothly lowered until finally vanishing. Using literature findings to validate the results on mean stress relaxation, two simulations were run using parameter set LK and compared with the experimental findings reported by

Gribbin et al. (2016). These plots are shown in figure 2.25 where no explicit parameter calibration was done but still the macroscopic mean stress evolved to a value close to the one observed in IN718 alloys.

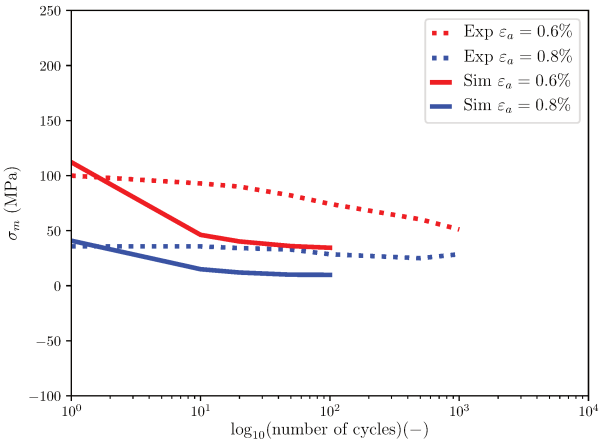

Figure 2.25: Using asymmetric strain controlled tests, evolution of mean stress for two different strain amplitudes: $\varepsilon_a = 0.6$ and 0.8 %. Simulation are presented with solid lines while experiments are shown with dotted lines. The experimental curves are taken from Gribbin et al. (2016)

After establishing that the crystal plasticity model can reproduce macroscopic responses, a step was taken to see what had happened inside the microstructure. The motivation behind this scrutiny was that in a full field crystal plasticity model, local heterogeneities restrict the evolution of plasticity to a highly nonlinear fashion, which leads to a characteristic mechanical response. Various authors have already been able to model asymmetric cyclic responses using self-consistent schemes (Krishna et al., 2009; Sai and Cailletaud, 2007; Zecevic and Knezevic, 2018; Zecevic et al., 2016), but the advantage of using full field techniques is that local heterogeneities can be discovered, where the driving force for the onset of different macroscopic phenomena may be analyzed.

At the local level, two types of results were presented, i.e. contour maps as well as probability distribution plots of several constitutive equation variables. For strain localization several experimental findings are available either using in-situ SEM DIC (Stinville et al., 2016; Stein et al., 2014; Walley et al., 2012), or for sub-grain strain fields (Di Gioacchino and Quinta da Fonseca, 2013; Kammers and Daly, 2013). These findings though important are mostly reported after applying monotonic tensile loadings. A finding by Abuzaid et al. (2012) shows the experimental

distribution of the accumulated plastic strain but only after a monotonic tensile load. A major finding, as shown in figures 2.15 and 2.21, is that under asymmetric cyclic loads, the accumulated plastic strain splits into a bimodal distribution, which helps materials exhibit plastic shakedown in the case of stress controlled loadings, or retain a mean stress in the case of strain controlled loadings. Also the distribution curves in the paper pertain to the bulk of the polycrystal whereas experimental findings usually adhere to surface measurements. Interestingly, evidence of crack size distributions in a nickel-based superalloy under high cycle fatigue loading conditions was found by Shenoy et al. (2007). Such damage distributions can be correlated with the distribution of Fatigue Indicator Parameters (FIPs) directly linked to plastic activity in the grains. Extensive work has been done by Castelluccio et al. (2016) for the development of FIPs extracted from full field CPFEM statistical volume element simulations. However, such papers deal with symmetric loading conditions which also in computations result in a unimodal plastic strain distribution. To this extent, no evidence of bimodal strain distributions has been found in literature.

As a final comment the motivation of this study was to address the open question of how local hardening effects the macroscopic response of metallic materials. Although the parameter sets are close to copper and nickel based superalloys, they were not quantitatively calibrated because the intention was not to adhere to a particular material but to focus on what can be extracted from the polycrystal model using the scale transition rule. A qualitative analysis was done for the origin of different mechanisms when a single crystal transitions into a polycrystal.

2.8 Conclusion and ongoing work

2.8.1 Conclusion

Using rate-independent crystal plasticity with kinematic hardening, the cyclic response of FCC polycrystalline materials has been characterized both at the macroscopic and local levels. The macroscopic response was summarized by appropriate mean stress / stress amplitude maps whereas the mechanisms underlying each type of material response were explored using local statistics. For these two crystal plasticity. Two sets of materials parameters with various amounts of yield stress and hardening were considered in order to illustrate the capability of the polycrystal model to capture complex loading behavior under strain or stress loading control.

All simulations were run for a hundred cycles each, and more than 1000 cycles for some of them, and then the response was analyzed. The single crystal material model was kept as simple as possible because it is sufficient to explain, at least qualitatively, most features of the observed polycrystal behavior. Evaluation of the results reveals the following major findings:

- For stress controlled asymmetric simulations:
  1. Strain ratcheting in a single (resp. poly) crystal is characterized into three (resp. four) regimes. Elastic accommodation, elastic shakedown and ratcheting regimes are common to single and polycrystals. In contrast, plastic shakedown takes place only in polycrystals.
  2. A series comparison test as well as the bimodality of accumulated plastic strain distribution criterion were proposed to detect ratcheting or plastic shakedown. A remarkable result of the analysis is the evidence of a correlation between the existence of a bimodal distribution and overall plastic shake down.
  3. A theoretical diagram for ratcheting in single crystals is built in terms of the stress amplitude versus mean stress. Several simulations were run and a similar diagram was filled for the polycrystal showing different regimes of elastic and plastic shakedown as well as ratcheting.
  4. Gauss point statistics indicate that the von Mises stress in polycrystals is bimodal. These two modes become more prominent under progressive cyclic loading and they correspond to different regions of the polycrystal respectively made of soft and hard grains in the sense of Schmid factor.
  5. Local ratcheting events were observed in polycrystals experiencing plastic shakedown at the macroscopic scale.
  6. Evolution of the number of activated slip systems during cycling shows a trend towards single slip occurring the core of the grains while multislip is observed mostly at grain boundaries.
- For strain controlled asymmetric simulations:
  1. Cyclic mean stress relaxation in a single crystal can be broken down into three distinct regimes: Purely elastic response, elastic accommodation after a first elastoplastic period and plastic shakedown with vanishing mean stress. Instead, in a polycrystal, a smooth transition between these scenarios is observed. Mean stress relaxation towards stabilized finite values was observed for polycrystals.

2. Cyclic mean stress relaxes to near zero for parameter set HK (high kinematic hardening), whereas it does not relax to zero for parameter set LK (high yield strength).
3. Distribution curves of the accumulated plastic strain are found to be bimodal under some loading conditions. One part of the microstructure undergoes purely elastic accommodation whereas the remaining part of the polycrystal experiences continuing plastic activity. From the observations, it is conjectured that the mean stress in a polycrystal will relax to zero when the distribution becomes unimodal.
4. Contour plots reveal that the high cyclic mean stress is more susceptible to concentrate at grain boundaries or at triple junctions and this local interaction causes a nonzero mean stress in a polycrystal.

These results show that the grain to grain interactions induce cyclic responses that strongly differ from that of the single crystal. In particular these interactions are responsible for the existence of plastic shakedown regimes under stress control and of incomplete mean stress relaxation under strain control. These results contribute to the understanding of complex stress-strain redistribution phenomena at work in cyclically loaded polycrystals using computer based phenomenological models. These crystal plasticity models are already extensively in use and their capability to mimic real polycrystals has been scrutinized in this article. The macroscopic responses of both load and strain controlled tests are in good agreement with experimental results for engineering FCC alloys where a plastic shakedown as well as a non-zero mean stress are frequently observed.

Other methods of statistical analysis could be used to dig into the huge amount of data produced in this work. Machine learning techniques have also been used in recent works to find out some meta-models for fatigue crack initiation. The potential of such methods is considered by Rovinelli et al. (2018) to examine correlations of various parameters near small fatigue cracks in polycrystals.

Chapter 3

Hybrid hyper-reduction in crystal plasticity

Résumé

Les simulations par éléments finis de plasticité cristalline à haute résolution exigent d'énormes ressources informatiques, en particulier dans les cas où des centaines de cycles de charge sont impliqués dans les prédictions du phénomène de rochet. Plus important encore, en raison de la nature cyclique du problème, l'erreur d'approximation peut s'accumuler au fil des cycles. Cela nécessite que les erreurs d'approximation soient minimes. Dans ce contexte, nous proposons une méthode de réduction de l'ordre fondée sur un modèle de projection qui couple les approximations locales par éléments finis dans un domaine d'intégration réduite à une approximation de base par ordre réduit. Il s'agit d'un schéma hybride d'hyperréduction. De plus, comme les prédictions complètes par éléments finis du rochet sont hors de portée, les données de simulation non complétées sont utilisées pour former la base d'ordre réduit via une analyse en composantes principales non centrée. Seuls quelques cycles de charge sont prévus dans l'étape d'apprentissage. La méthode hybride d'hyper-réduction est utilisée et comparée à l'approche conventionnelle de l'hyper-réduction pour un agrégat polycristallin de grande taille. Par exemple, on simule un ensemble d'informations statistiques suffisamment important pour que la réponse matérielle locale puisse être analysée à l'aide de la méthode proposée, comme si les simulations par éléments finis habituelles avaient été effectuées.

3.1 Introduction

In its most general definition, model order reduction aims at proposing a model whose number of DOFs are reduced, reduced order model (ROM), compared to a full order model (FOM), obtained by a classical approximation method. To reduce the number of DOFs, the idea is to look for the solution of the problem in as small an approximation space as possible. The domain covered by the term model order reduction is very broad which is why an inventory of existing methods will not be made, but those methods which will directly affect this work will be stated. Also, the methods employed here are part of the framework of unsupervised machine learning methods, where empirical knowledge of feature space is extracted from simulation data that is not annotated. In practice, this is usually done using matrix factorization methods after having grouped the data into matrices. In this regard there are two broad categories of model order reduction methods available *a priori* and *a posteriori*. The methods being used in this thesis are posteriori which approximate the behavior of the object of study using experiences or empirical evidence. For these types of methods, data is needed to construct the reduced bases (RB). The data collected are generally the result of results of calculations, obtained using the FOM, in the parametric or temporal space studied. These calculation results are commonly called snapshots according to the terminology used by Sirovich (1987). The RB is then composed of either snapshots or vectors obtained by extracting the most important information using data compression techniques. It is also possible to relate these types of methods to the non-centered principal component analysis method used in unsupervised machine learning.

Of particular interest in recent times is the method of using a RB. The strategy adopted in such methods involves projecting the FOM onto a subspace generated by some selected functions to represent the solutions of the FOM for a certain subspace. The first work concerning this type of method was carried out for mechanical problems of linear and non-linear structures Almroth et al. (1981, 1978a); Noor (1982). Later on, more work was done by several researchers for the RB method Prud'Homme et al. (2002); Maday et al. (2002); Maday and Rønquist (2002). Here it is important to clarify two terms which are generally used in posteriori methods: the *online* and *offline*. The offline part of posteriori methods consists of a learning phase where relationships are built between different parameters and an approximation subspace is constructed. In the offline phase, an estimation of the system is done using the knowledge extracted during the offline phase.

One of the best-known and most widely used posteriori technique for model order

reduction is the POD-Galerkin method, which is based on the proper orthogonal decomposition (POD), and is known to help obtain an optimal RB. Its first use for model order reduction was done by Aubry et al. (1988) while more recent studies can be found in Akkari et al. (2014); Liberge and Hamdouni (2010). An overview of the POD technique as well as snapshots will be given in the following subsections. For understanding purposes, hyper-reduction in elasticity will be presented in Section 3.2 which will be followed by the hyper-reduction formulation for non-linear mechanics of materials in Section 3.3. The finite element mesh description will be detailed in Section 3.4, and the numerical setup in Section 3.5. Results and conclusions will be given in Sections 3.6 and 3.7

3.1.1 Model order reduction using POD

POD, originally developed by Pearson (1901) for graphical analyses, is a widely used method for low rank approximations of high dimensional processes. A start can be taken by supposing that there exists a function $\underline{\underline{G}}(x)$ over some domain of interest. This function can be written as a linear combination of some basis functions $\underline{\zeta}^i(x)$ such that:

$$\underline{\underline{G}}(x) \approx \sum_{i=1}^{M} a_i . \underline{\zeta}_i(x) \tag{3.1}$$

where the solution tends to get better as M is increased. The amplitudes of the expansion, a_i are chosen after the basis function and are determined by a minimization process, which for the approximation in the least square sense can be stated as the minimum of:

$$\left\| \underline{\underline{G}}(x) - \sum_{i=1}^{M} a_i \underline{\zeta}_i(x) \right\|_{L^2} \tag{3.2}$$

From equation 3.1 it can be anticipated that its representation will not be unique because the choice of basis functions $\underline{\zeta}^i(x)$ to approximate $\underline{\underline{G}}(x)$ is arbitrary. Hence, the objective is to create a basis for a relatively small number M to approximate the function $\underline{\underline{G}}(x)$. POD is used as a tool to choose and construct the optimal basis for the function in question.

In the POD formulation, basis selection is done keeping in view orthonormality of

these functions such that:

$$\int_{\Omega} \underline{\zeta}_i(x).\underline{\zeta}_j(x)dx = \begin{cases} 1 \text{ if } i = j \\ 0 \text{ if } i \neq j \end{cases} \tag{3.3}$$

The amplitude then takes the form:

$$a_i = \int_{\Omega} \underline{\underline{G}}(x).\underline{\zeta}_i(x)d\Omega \tag{3.4}$$

signifying that each amplitude depends only on its own basis vector and not on those of the others. Also, the basis vectors are optimized in such a way that for any value of M the approximation is optimal. In other words, our goal is to find a sequence of orthonormal functions such that the first n basis vectors give the best n-term approximation. These ordered orthogonal functions are called the proper orthogonal modes for the function $\underline{\underline{G}}(x)$ and equation 3.1 is known as the POD of $\underline{\underline{G}}(x)$. Now putting in time dependence of the problem such that $\underline{u}(x, t_j)$ is a function of time and x, equation 3.1 can be reformulated to look like:

$$\min_{\underline{\zeta}_k(x)} \sum_{j=1}^{m} \left|\left| \underline{u}(x, t_j) - \sum_{k=1}^{M} \underline{\zeta}_k(x) \int_{\Omega} \underline{u}(x, t_j)\underline{\zeta}_k(x)dx \right|\right|^2_{L^2(\Omega\times[0,time])} \tag{3.5}$$

such that $||\underline{\zeta}_k||^2_{L^2(\Omega\times[0,time])} = 1$ i.e. the L^2 norm is equal to 1. Then, it can be supposed that

$$\underline{u}(x, t_j) = \sum_{i=1}^{\mathcal{N}} \psi_i(x)Q_{ij}, \tag{3.6}$$

such that ψ_i is a finite element shape function and $\underline{\underline{Q}}$ is a matrix containing simulation results and

$$\underline{\zeta}_k = \sum_{i=1}^{\mathcal{N}} \psi_i(x)V_{ik}. \tag{3.7}$$

The integral of their product over the whole domain (Ω) leads to:

$$\begin{aligned}\int_\Omega \underline{u}(x,t_j)\underline{\zeta}_k d\Omega &= \sum_\alpha \sum_\beta \int_\Omega \psi_\alpha(x)\psi_\beta(x)dx \underline{\underline{Q}}_\alpha \underline{\underline{V}}_\beta \\ &= \underline{\underline{Q}}_j^T \underline{\underline{\underline{\mathcal{M}}}} \underline{\underline{V}}_k \\ &= \underline{\underline{Q}}_j^T \underline{\underline{\underline{L}}} \underline{\underline{\underline{L}}}^T \underline{\underline{V}}_k\end{aligned} \tag{3.8}$$

where α and β are two variables in space. Also $\underline{\underline{Q}}^T \underline{\underline{L}} = \underline{\underline{\tilde{Q}}}^T$ and $\underline{\underline{L}}^T \underline{\underline{V}}_k = \underline{\underline{\tilde{V}}}$, and $\underline{\underline{\tilde{Q}}} = \underline{\underline{L}}^T \underline{\underline{Q}}, \underline{\underline{\tilde{V}}} = \underline{\underline{L}}^T \underline{\underline{V}}$ where $\underline{\underline{L}}$ is a lower triangular matrix with real and positive diagonal entries, and the mass matrix $\underline{\underline{\underline{\mathcal{M}}}}_{\alpha\beta}$ equates to:

$$\underline{\underline{\underline{\mathcal{M}}}}_{\alpha\beta} = \int_\Omega \psi_\alpha(x)\psi_\beta(x)d\Omega \tag{3.9}$$

The Cholesky decompositon of the positive definite mass matrix reads:

$$\underline{\underline{\underline{\mathcal{M}}}} = \underline{\underline{\underline{L}}} \underline{\underline{\underline{L}}}^T \tag{3.10}$$

Then the minimization problem of equation 3.5 reads:

$$\min_{\underline{\underline{V}}, \underline{\underline{V}}^T \underline{\underline{V}} = \underline{\underline{I}}} ||\underline{\underline{Q}} - \underline{\underline{\underline{V}}} \underline{\underline{\underline{V}}}^T \underline{\underline{\underline{L}}} \underline{\underline{\underline{L}}}^T \underline{\underline{Q}}||_{\underline{\underline{\underline{\mathcal{M}}}}} \tag{3.11}$$

or:

$$\min_{\underline{\underline{\tilde{V}}}, \underline{\underline{\tilde{V}}}^T \underline{\underline{\tilde{V}}} = \underline{\underline{I}}} ||\underline{\underline{\tilde{Q}}} - \underline{\underline{\underline{\tilde{V}}}} \underline{\underline{\underline{\tilde{V}}}}^T \underline{\underline{\tilde{Q}}}|| \tag{3.12}$$

where:

$$\begin{cases} \underline{\underline{V}}^T \underline{\underline{V}} = \underline{\underline{I}} \\ \underline{\underline{\tilde{Q}}} = \underline{\underline{L}}^T \underline{\underline{Q}} \\ \underline{\underline{\tilde{V}}} = \underline{\underline{L}}^T \underline{\underline{V}} \end{cases} \tag{3.13}$$

signify that the columns of $\underline{\underline{V}}$ are orthogonal to each other i.e. they are orthogonal basis vectors.

3.1.2 Discrete POD theory

Discrete POD theory, also referred to as principal component analysis (PCA) or Karhunen-Loeve decomposition(K. Karhunen, 1947), is a method that deals with random variables and is of a discrete nature. Our goal in PCA is to reduce the dimensionality of the dataset consisting of a large number of correlated variables, while keeping the variation in the dataset. Data can be transformed to a new set of variables called the principal components, which are uncorrelated, and ordered such that the first few contain the most information. After identifying the principal components, the dimension of the original space is reduced by keeping just the first few components. In essence, the PCA finds the solution of the minimization problem in equation 3.12.

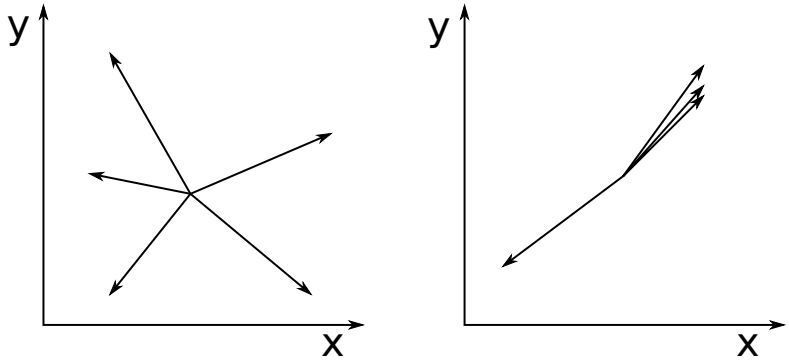

Figure 3.1: Uncorrelated and closely co-related vectors

Considering a simple case of 2-dimensional space where the number of variables is just two, PCA can be geometrically visualized. Variables here are the components of each 2-D vector. Figure 3.1 shows such an interpretation where the left plot shows uncorrelated variables while the plot on the right shows highly correlated variables. In such a case, the reduction of dimensionality means that the resulting vectors can be expressed with just one component (instead of two).

Figure 3.2 considers the orientations of the vectors, where it can be seen that in the current setting a one component approximation will lead to considerable approximation errors. But a new coordinate system can be introduced which is able to approximate the data using just one component (x'). Principal component analysis defines a new coordinate system to minimize this loss of data. In this case the new axis (x') is chosen in such a way that it gives the best one component approximation, and this new basis is the proper orthogonal basis for the vectors set. This concept can be extended to higher dimensions where the goal is to find

orthogonal directions in a n-dimensional space; n being the original dimensionality of the vectors in set. Two ways to construct this POD basis are shown below.

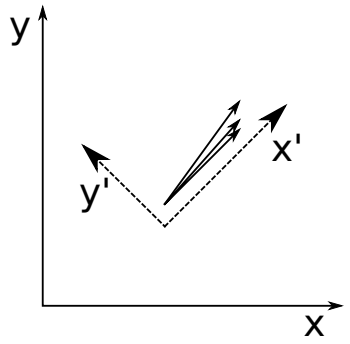

Figure 3.2: One component approximation of a two-variable space

3.1.3 PCA by minimizing the error approximation

A set containing M, n-dimensional vectors in a matrix $\underline{\underline{Q}}$ are assumed. The goal is to find a set of orthonormal basis vectors that minimizes this error but first a covariance matrix is defined such that:

$$\underline{\underline{C}} = \underline{\underline{\tilde{Q}\tilde{Q}^T}}. \tag{3.14}$$

A detailed derivation of the error minimization procedure is given in Buljak (2012). The crux is that a set of M, n-dimensional vectors are stored in $\underline{\underline{Q}}$. Then the covariance matrix is computed, which is followed by the computation of the eigenvectors of the covariance matrix stored in the matrix $\underline{\underline{\Phi}}_{\underline{\underline{V}}}$ and it is declared that the error of approximation is minimized if the new basis is constructed of k eigenvectors that correspond to the first k largest eigenvalues of the covariance matrix $\underline{\underline{C}}$. If all the eigenvectors of matrix $\underline{\underline{C}}$ are taken into account, there will be no error when projecting available data on eigenvectors; the only difference being that all the vectors $\underline{v}_i$ will be expressed in a different coordinate basis.

3.1.4 Construction of the POD basis using the SVD approach

Singular value decompositon (SVD) can be viewed as an extension of the eigenvalue decomposition for the case of nonsquare matrices. SVD states that for any $N \times M$ matrix $\underline{\underline{Q}}$ there exist two orthonormal matrices i.e. $\underline{\underline{\tilde{V}}}$ which is $N \times N$ and $\underline{\underline{W}}$ which is $M \times M$ such that

$$\underline{\underline{\tilde{Q}}} = \underline{\underline{\tilde{V}SW}}^T, \tag{3.15}$$

then:

$$\underline{\underline{Q}} = \underline{\underline{VSW}}^T, \text{ with } \underline{\underline{V}}^T\underline{\underline{V}} = \underline{\underline{I}}, \ \underline{\underline{W}}^T\underline{\underline{W}} = \underline{\underline{I}} \tag{3.16}$$

where $\underline{\underline{S}}$ is a rectangular $N \times M$ matrix with $\underline{\underline{S}} = diag(\sigma_1, ..., \sigma_p) \in \mathbb{R}^{N \times M}$ and $\sigma_1 \geq \sigma_2 \geq ... \geq \sigma_p > 0, p = \min(M, N)$. σ_is are the singular values of the matrix $\underline{\underline{Q}}$. Then, the idea is to keep the first k singular values in a square $k \times k$ diagonal matrix $\underline{\underline{S}}_k$ and collect the corresponding columns from $\underline{\underline{V}}$ and $\underline{\underline{W}}$. Hence, the k^{th} approximation of $\underline{\underline{Q}}$ is given by:

$$\underline{\underline{Q}} \approx \underline{\underline{V}}_k\underline{\underline{S}}_k\underline{\underline{W}}_k^T. \tag{3.17}$$

This scheme is optimized by the fact that the singular values are arranged in descending order along the diagonal of matrix $\underline{\underline{S}}$ which signifies that any k singular values will give the best rank k approximation of $\underline{\underline{Q}}$. As stated before, SVD can be applied to rectangular matrices as opposed to orthogonal decomposition which deals with square matrices. But the relation between the two can be quantified in what follows. As defined before, the covariance matrix is $\underline{\underline{C}} = \underline{\underline{QQ}}^T$, and substituting the singular value decomposed components into it will lead to:

$$\begin{aligned}
\underline{\underline{QQ}}^T &= \underline{\underline{VSQ}}^T(\underline{\underline{VSQ}}^T)^T \\
&= \underline{\underline{VSW}}^T\underline{\underline{WVS}}^T \\
&= \underline{\underline{VS}}(\underline{\underline{VS}})^T \\
&= \underline{\underline{VSS}}^T\underline{\underline{V}}^T \\
&= \underline{\underline{VS}}^2\underline{\underline{V}}^T
\end{aligned}$$

and since $\underline{\underline{V}}$ is orthogonal, the following is obtained:

$$\underline{\underline{CV}} = \underline{\underline{VS^2}} \tag{3.18}$$

Equation 3.18 shows that the columns of $\underline{\underline{V}}$ are the eigenvectors of matrix $\underline{\underline{C}}$ and that the singular values of matrix $\underline{\underline{Q}}$ are the square roots of the eigenvalues of matrix $\underline{\underline{C}}$. Similarly, if a modified covariance matrix is defined such that:

$$\underline{\underline{C}}_{modified} = \underline{\underline{Q}}^T \underline{\underline{Q}}, \tag{3.19}$$

after doing the same procedure, it can be found that $\underline{\underline{C}}_{modified}\underline{\underline{W}} = \underline{\underline{WS^2}}$, which signifies that the columns of $\underline{\underline{W}}$ are the eigenvectors of $\underline{\underline{C}}_{modified}$. Therefore, it can be seen that there is a full equivalence between the approximation given by SVD and POD basis such that:

$$\underline{\underline{Q}} \approx \underline{\underline{V}}_k \underline{\underline{S}}_k \underline{\underline{W}}_k^T$$

For posteriori methods, a RB is constructed which generates the subspace of approximation. The data is collected from simulation results obtained using the FOM. A ROM is then obtained by a Galerkin type projection from the FOM on to the RB. In the context of finite element method, continuum problems are solved on discretized domains, where as a resulting response discrete fields are obtained, represented by values at the nodes and integration points. This suggests that the results of these simulations can be treated by the aforementioned discrete POD theory. For this the concept of a snapshot is introduced (Sirovich, 1987).

A snapshot represents some output of a system corresponding to some input. It is a collection of n discrete values of a certain state variable evolving at each time increment. In the present case, snapshots of nodal displacement and flux at certain time increments are saved. In other words, snapshots are a collection of instances taken from a simulation. A set of s_i snapshots, corresponding to different time instances are collected in a matrix $\underline{\underline{Q}}$, the snapshot matrix (see figure 3.3). Hence, the matrix represents the responses of one system corresponding to different parameter values. It should also be anticipated that there will be a strong correlation between the snapshots as they are just the outputs of a system where certain parameters are varying. This correlation gives the opportunity to implement the aforementioned POD theory and construct a new low dimensional basis. For instance, as the displacement field of some body is considered, all nodal

displacements may be collected at any instance in a snapshot $\underline{S_i}$. Lets assume that the simulation used a linear material model, and the increase in displacement field (from one snapshot to another) is linear. Then all the snapshots can be expressed, without any loss of information, in a reduced space containing just one empirical mode.

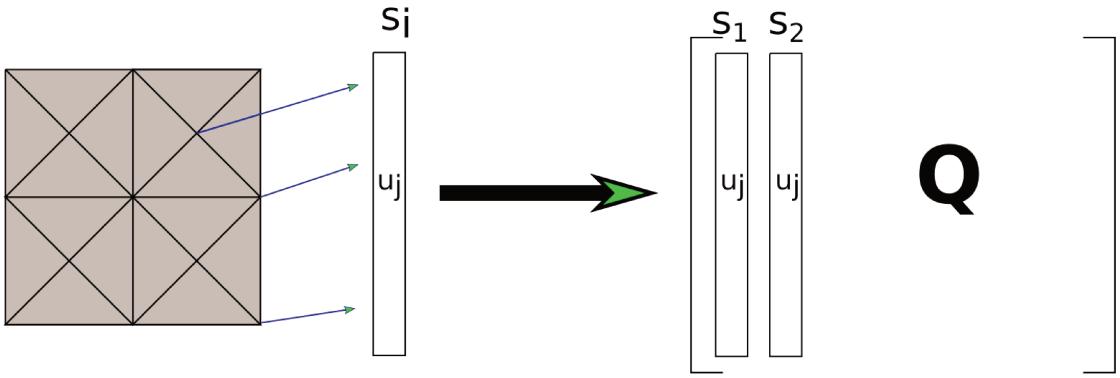

Figure 3.3: The concept of a snapshot in finite elements

3.1.5 Hyper-reduction type methods

In the context of non-linear PDEs, linearizion is usually done using Newton-type iterative methods. The standard projection for building a ROM, in the case of methods based on the projection of the equations on a RB, in this case is not effective because the evaluation of large nonlinear terms and the products they involve, at each iteration are too expensive. For this reason, hyper-reduction methods have been introduced which make it possible to limit the complexity of the non-linear problem to a certain number of inputs which do not depend on the complete FE mesh.

Approximation of the nonlinear term by interpolation

The idea of model order reduction methods approximating the nonlinear term by interpolation is similar to the Gappy-POD principle applied by Everson and Sirovich (1995) to image processing. It says that let I be a column vector containing the values of the pixels of an image, known only on a set $\mathcal{F}$, and $\underline{\underline{V}}$ a RB of l columns constructed by POD. The Gappy-POD proposes a prediction I_l of the

values of the image:

$$I_l = \underline{\underline{V}}(\underline{\underline{V}}[\mathcal{F},:]^T\underline{\underline{V}}[\mathcal{F},:])^{-1}\underline{\underline{V}}[\mathcal{F},:]^T I[\mathcal{F}] \tag{3.20}$$

In the framework of model order reduction used in this thesis, this is the non-linear term which will be approximated from a few DOFs. What varies is the method with which the RB was built and the choice of interpolation points. One of the first propositions of such techniques was the Empirical Interpolation Method (EIM) (Barrault et al., 2004). The points coming out of empirical interpolation, also called "magic points" according to Maday et al. (2007) are obtained using a greedy algorithm (Edmonds, 1971; Vince, 2002) where at each iteration the point selected is the one that maximizes the error between the $(i+1)$-th function of the RB and its reconstruction using i interpolation points already calculated.

The discrete version of EIM (Chaturantabut and Sorensen, 2010) abbreviated DEIM is applied to a RB preferably built by POD. Similar to the EIM, while doing DEIM, the selection of interpolation points is done using a greedy algorithm. The benefit of providing a RB obtained by POD with the DEIM algorithm is that the column vectors are ordered by importance. The interpolation points are then selected iteratively so as to approximate the vectors in order of importance. A depiction of the hyper-reduction approach is done in figure 3.4 where all simulation results are stored in a matrix $\underline{\underline{Q}} \in \mathbb{R}^{N\times m}$. A RB $\underline{\underline{V}}$ is then extracted using a POD approximation. If the POD approximation is exact then there exists a reduced coordinate $\underline{\underline{\gamma}}$, such that:

$$\underline{\underline{Q}} = \underline{\underline{V}}\underline{\underline{\gamma}} \tag{3.21}$$

$$\underline{\underline{\gamma}} = \arg\min_{\underline{\underline{\gamma}}^*} ||\underline{\underline{Q}}[\mathcal{F},:] - \underline{\underline{V}}[\mathcal{F},:]\underline{\underline{\gamma}}^*||_2 \tag{3.22}$$

where $\underline{\underline{\gamma}}$ the reduced coordinate. This reduced coordinate is minimum only when the following holds:

$$\underline{\underline{\gamma}} = (\underline{\underline{V}}^T[\mathcal{F},:]\underline{\underline{V}}[\mathcal{F},:])^{-1}\underline{\underline{V}}^T[\mathcal{F},:] \tag{3.23}$$

Plugging this value of $\underline{\underline{\gamma}}$ into equation 3.21 the following formulation for the gappy

POD is obtained:

$$\underline{\underline{Q}}_{Gappy} = \underline{\underline{V}}(\underline{\underline{V}}^T[\mathcal{F},:]\underline{\underline{V}}[\mathcal{F},:])^{-1}\underline{\underline{V}}^T[\mathcal{F},:] \tag{3.24}$$

The term *gappy* signifies that incomplete data sets are used for the predictions. This term stems from the postulation of Everson and Sirovich (1995) which states that if a field has a RB approximation, it is possible to measure this field at a few points Everson and Sirovich (1995). It should also be noted that the rows of the matrix $\underline{\underline{V}}$ correspond to the DOFs of the system, while the columns are the empirical modes used to estimate $\underline{\underline{Q}}$. In this thesis hyper-reduction (Ryckelynck, 2009) will be based on a reduced integration domain (RID). For nonlinear mechanics, the method greatly reduces the calculation time because at each iteration the reduced system of equations has to be solved. Also, this method is non-intrusive for material behavior, which means that the constitutive equation stays the same in the reduced setting. Such an approach enables transfer learning (Pan and Yang, 2010) from mechanics of materials to machine learning in solid mechanics. In the next section hyper-reduction is detailed for an elastic problem.

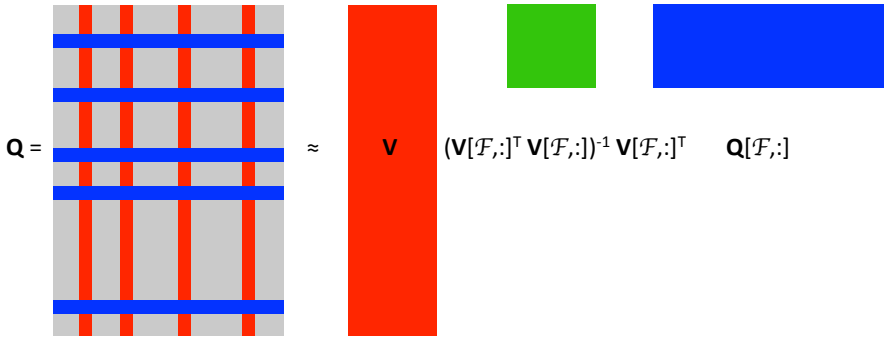

Figure 3.4: The gappy POD procedure applied to simulation results where $\underline{\underline{Q}}$ holds all simulation results and $\underline{\underline{V}}$ is the extracted reduced basis

3.2 Hyper-reduction in elasticity

Although HR has been introduced to deal with materials with non-linear behavior, to get a better understanding of topic, the equations formulated below are for a classical problem of elasto-static mechanics.

3.2.1 Strong formulation of the elastic problem

Let $\Omega \in \mathbb{R}^D$ be a bounded domain representing the reference configuration of a solid of dimension D. The static equilibrium equation of solids says that all forces on the body should sum to zero:

$$div\underline{\underline{\sigma}} + \underline{f} = 0 \text{ in } \Omega \tag{3.25}$$

where $\underline{\underline{\sigma}}$ is the second order symmetric Cauchy stress tensor and $\underline{f}$ the body forces per unit volume. Assuming that the material is linear elastic and under the assumption of small perturbations, the behavior law is written as:

$$\underline{\underline{\sigma}} = \underline{\underline{\underline{\underline{C}}}} : \underline{\underline{\varepsilon}} \text{ in } \Omega \tag{3.26}$$

where the strain tensor $\underline{\underline{\varepsilon}}$ is defined using the displacement field $\underline{u}$ according to the equation:

$$\underline{\underline{\varepsilon}} = \frac{1}{2}(\text{grad}\underline{u} + (\text{grad}\underline{u})^T) \text{ in } \Omega \tag{3.27}$$

The fourth order tensor for the modulus of elasticity $\underline{\underline{\underline{\underline{C}}}}$ has the following symmetries:

$$\underline{\underline{\underline{\underline{C}}}}_{ijkl} = \underline{\underline{\underline{\underline{C}}}}_{jikl} = \underline{\underline{\underline{\underline{C}}}}_{klij} \tag{3.28}$$

Two types of boundary conditions are imposed on the body i.e. either a displacement $\underline{u}_0$ imposed on Γ^D (Dirichlet) or surface forces $\underline{g}$ on Γ^N (Neumann), where Γ denotes the piecewise smooth boundary of the body:

$$\underline{u} = \underline{u}_0 \text{ over } \Gamma^D \tag{3.29}$$

$$\underline{g} = \underline{\underline{\sigma}}\underline{n} \text{ over } \Gamma^N \tag{3.30}$$

where $\underline{n}$ denotes the normal outgoing unit vector. Moreover, it is necessary that the surfaces Γ^D and Γ^N form a partition of $\partial\Omega$, the edge of Ω. That is, the surfaces Γ^D and Γ^N on which the boundary conditions 3.29 and 3.30 are imposed should obey $\partial\Omega = \Gamma^D \cup \Gamma^N$ and $\Gamma^D \cap \Gamma^N = \emptyset$. The problem is then well posed in the sense that boundary conditions guarantee the existence and uniqueness of the solution in displacements and stresses. If Γ^D is non-zero, the solution of displacement $\underline{u}$ is unique to rigid body movement.

In a more condensed way, the strong formulation of the elasto-static problem under the assumption of small deformations is written as the following system of equations:

$$\begin{aligned} -div\underline{\underline{\sigma}} &= \underline{f} \text{ in } \Omega \\ \underline{\underline{\sigma}} &= \underline{\underline{\underline{\underline{C}}}} : \underline{\underline{\varepsilon}} \text{ in } \Omega \\ \underline{\underline{\varepsilon}} &= \frac{1}{2}(\text{grad}(\underline{u}) + (\text{grad}(\underline{u}))^T) \text{ in } \Omega \\ \underline{u} &= \underline{u}_0 \text{ over } \Gamma^D \\ \underline{\underline{\sigma}}.\underline{n} &= \underline{g} \text{ over } \Gamma^N \end{aligned} \tag{3.31}$$

3.2.2 Formulation of a weak from for the elastic problem

Let $\mathcal{V}_0$ be the vector space of a kinematically admissible displacement field such that:

$$\mathcal{V}_0 = \{\underline{v} \in (H^1(\Omega))^D | \underline{v} = \underline{0} \text{ over } \Gamma^D\} \tag{3.32}$$

Here $H^1(\Omega)$ is the space of scalar functions with genelarized partial derivatives of order ≤ 1 i.e. square integrable, in other words $u \in H^1(\Omega)$ if

$$||u||^2_{H^1(\Omega)} = \int_\Omega \frac{\partial u}{\partial x_j}\frac{\partial u}{\partial x_j} d\Omega + \int_\Omega u u d\Omega \leq \infty \tag{3.33}$$

The integral formulation equivalent to the static equilibrium equation 3.25, obtained by making the scalar product $L^2(\Omega)$ with an application $\underline{v} \in \mathcal{V}_0$ is written:

$$-\int_\Omega div(\underline{\underline{\sigma}}^T)\underline{v}d\Omega = \int_\Omega \underline{f}^T\underline{v}d\Omega \ \ \forall \underline{v} \in \mathcal{V}_0 \tag{3.34}$$

By replacing the term under the integral of the first term of equation 3.34 by its equivalent in the relation:

$$div(\underline{\underline{\sigma}}^T\underline{v}) = div(\underline{\underline{\sigma}})^T\underline{v} + \underline{\underline{\sigma}} : \text{grad}(\underline{v}) \tag{3.35}$$

equation 3.34 becomes:

$$-\int_\Omega div(\underline{\underline{\sigma}}^T\underline{v})d\Omega + \int_\Omega \underline{\underline{\sigma}} : \text{grad}(\underline{v})d\Omega = \int_\Omega \underline{f}^T\underline{\underline{v}}d\Omega, \ \ \forall \underline{v} \in \mathcal{V}_0 \tag{3.36}$$

By applying the divergence theorem, to the first term of equation 3.36, the latter is written:

$$-\int_{\partial\Omega}(\underline{\underline{\sigma}}\underline{v})^T\underline{n}d\Gamma + \int_\Omega \underline{\underline{\sigma}} : \text{grad}(\underline{v})d\Omega = \int_\Omega \underline{f}^T\underline{v}d\Omega \ \ \forall \underline{v} \in \mathcal{V}_0 \tag{3.37}$$

Since $\underline{\underline{\sigma}}$ is symmetric, the following relation is used on the first term of equation 3.37.

$$(\underline{\underline{\sigma}}\underline{v})^T\underline{n} = (\underline{\underline{\sigma}}\underline{n})^T\underline{v} \tag{3.38}$$

The symmetry of $\underline{\underline{\sigma}}$ also makes it possible to simplify the second term of equation 3.37 by noting that the product doubly contracted between $\underline{\underline{\sigma}}$ and the antisymmetric part of grad$\underline{v}$ in equation 3.39 is zero. The decomposition of grad$\underline{v}$ as a sum of a symmetric tensor and an antisymmetric tensor, taking into account that the symmetrical part is the linearized strain tensor 3.27, is written as:

$$\text{grad}(\underline{v}) = \underline{\underline{\varepsilon}}(\underline{v}) + \frac{1}{2}(\text{grad}(\underline{v}) - (\text{grad}(\underline{v}))^T) \tag{3.39}$$

With these two modifications taken into account in equation 3.37, the weak form of the equilibrium local equation 3.25 is obtained as follows:

$$\int_\Omega \underline{\underline{\sigma}} : \underline{\underline{\varepsilon}}(\underline{v})d\Omega = \int_\Omega \underline{f}^T\underline{v}d\Omega + \int_{\partial\Omega}(\underline{\underline{\sigma}}\underline{n})^T d\Gamma \ \ \forall \underline{v} \in \mathcal{V}_0 \tag{3.40}$$

In equation 3.40 taking into account the elastic behavior 3.26 and the doubly contracted product definition, and the Neumann boundary condition (3.30), the primitive variational formulation of the problem (3.31) is written under these conditions:

$$\begin{gathered} \text{Find } \underline{u} \in \mathcal{V} \text{ such that} \\ a(\underline{u}, \underline{v}) = l(\underline{v}), \ \ \forall \underline{v} \in \mathcal{V}_0 \end{gathered} \tag{3.41}$$

where a and l are defined as:

$$a(\underline{u}, \underline{v}) = \int_\Omega \underline{\underline{\varepsilon}}(\underline{v}) : \underline{\underline{\underline{\underline{C}}}} : \underline{\underline{\varepsilon}}(\underline{u}) d\Omega \tag{3.42}$$

$$l(\underline{v}) = \int_\Omega \underline{f}^T \underline{v} d\Omega + \int_{\Gamma^N} \underline{g}^T \underline{v} d\Gamma \tag{3.43}$$

3.2.3 Finite element method for a material with elastic behavior

The domain Ω is discretized into a set of K_i elements such that $\cup_i \bar{K}_i = \bar{\Omega}$. This spatial discretization is called the mesh. The finite element shape functions are denoted by $(\underline{\psi}_j)_{j=1}^m$, with m the number of nodes of the mesh to which those belonging to Γ^D are removed. The shape functions $(\underline{\psi}_i)_{i=1}^N, N = mD$ are introduced as they verify:

$$\underline{\psi}_i = \psi_j \underline{e}_k \ \text{ with } \ i = (j-1)D + k, \ \ j \in [1, m], \ \ k \in [1, D] \tag{3.44}$$

and $(\underline{e}_k)_{k=1}^D$ the vectors associated with Cartesian coordinates. $(\underline{\underline{\psi}})_{i=1}^N$ defined by 3.44 form a basis for the finite-dimensional subspace $\mathcal{V}_j \subset \mathcal{V}_0$. The Galerkin's method then consists of looking for a field of displacement of the form:

$$\underline{u}_h(\underline{x}) = \underline{u}_0(\underline{x}) + \sum_{i=1}^N \underline{\psi}_i(\underline{x}) a_i, \ \ \forall \underline{x} \in \Omega \tag{3.45}$$

By applying the finite element method, the discretized problem is achieved using the weak formulation 3.41:

$$\begin{aligned} &\text{Find } \underline{a} \in \mathbb{R}^N \text{ such that} \\ &\underline{\underline{K}}\,\underline{a} = \underline{F} \end{aligned} \tag{3.46}$$

where $\underline{\underline{K}}$ is the stiffness matrix and $\underline{F}$ the vector of generalized forces. Both quantities are defined below as:

$$(\underline{\underline{K}})_{ij} = a(\underline{\psi}_j, \underline{\psi}_i), \ \ \forall i, j \in [1, N]^2 \tag{3.47}$$

$$(\underline{F}_i) = l(\underline{\psi}_i) - \int_\Omega \underline{\underline{\varepsilon}}(\underline{u}_0) : \underline{\underline{\underline{C}}} : \underline{\underline{\varepsilon}}(\underline{\psi}_i) d\Omega, \ \ \forall i \in [1, N] \tag{3.48}$$

3.3 Hybrid hyper-reduction in mechanics of materials

The displacement field can be decomposed over a set of basis functions $\psi_i(x)$ which correspond to the shape functions of an FE model defined on domain Ω.

$$\underline{u}(\underline{x}, t) = \sum_{i=1}^{N_d} a_i(t)\psi_i(x) \tag{3.49}$$

where N_d corresponds to the number of DOFs of the mesh and a_i the i^{th} nodal DOFs of the FE model. Hyper reduction methods have already been proposed in literature (Ryckelynck et al., 2010) and are capable of reducing the need of large computational resources. Hyper-reduced models restrict a set of Finite Element (FE) equations for a RID and using a RB, seek an approximate solution of these FE equations. In essence, to set up the reduced equations for a given FE model, this approach accounts for a low rank of the reduced approximation. This can be elaborated using a linear elastic finite element model where the FE balance equation reads:

$$\underline{\underline{K}}\,\underline{a}^{FE} = \underline{F} \tag{3.50}$$

where $\underline{a}^{FE} \in \mathbb{R}^{N_d}$, and $\underline{\underline{K}} \in \mathbb{R}^{N_d \times N_d}$ is the stiffness matrix of the FE model, whereas $\underline{c} \in \mathbb{R}^{N_d}$ the right hand side term of the FE equation. For a given RB of rank $N_R \underline{\underline{V}} \in \mathbb{R}^{N_d \times N_d}$, the approximate reduced solution of the balance equations is denoted by $\underline{a}^R$ as follows:

$$\underline{a}^R = \underline{\underline{V}} \underline{b}^R \tag{3.51}$$

where $\underline{b}^R \in \mathbb{R}^{N_R}$ are ROM variables. To find a unique solution $\underline{b}^R$ the rank of $\underline{\underline{KV}}$ needs to only be N_R. Since N_d is usually larger than N_R, a few rows of $\underline{\underline{KV}}$ can be selected to preserve the rank of the submatrix. The set of selected rows is denoted as $\mathcal{F}$. This row selection is achieved by considering balance equations set up on the RID. This RID is denoted by Ω_R which is a subset of the whole domain. For a given RID, the set $\mathcal{F}$ is defined as:

$$\mathcal{F} = \{i \in \{0, ..., N_d\}, \int_{\Omega \setminus \Omega_R} \psi_i^2(x) dx = 0\} \tag{3.52}$$

These hyper reduced balance equations are restricted to the RID using convenient test functions such that:

$$(\underline{\underline{V}}[\mathcal{F}, :])^T \underline{\underline{K}}[\mathcal{F}, :] \underline{\underline{V}} \underline{b}^R = (\underline{\underline{V}}[\mathcal{F}, :])^T \underline{F}[\mathcal{F}] \tag{3.53}$$

Also, the RID must be large enough to have $\text{rank}(\underline{\underline{K}}[\mathcal{F}, :]\underline{\underline{V}}) = N_R$ and $\text{rank}(\underline{\underline{V}}[\mathcal{F}, :]) = N_R$; hence cardinality of the number of DOFs in the RID should be greater than or equal to N_R. The current reduced setting uses a hybrid hyper-reduction approach which signifies that a FE correction function is also added to the reduced domain (Baiges et al., 2013). In the hybrid hyper-reduction method the RID is generated using the assembly of elements containing the interpolation points related to the reduced bases of stresses and displacements. Hence, Ω_R, the reduced integration domain, has four sub-domains, i.e. the sub-domains provided by the displacement and stress fields (Ω_R^u , Ω_R^σ), the sub-domain provided by the user (Ω_z^{user}) and an additional domain Ω_+ which corresponds to a set of neighboring elements of the previous sub-domains. The first two sub-domains are automatically provided by the appropriately selected modes while the third sub-domain is called the *zone of interest*. This zone is provided wherever in which region the user perceives to be important. This zone can be taken anywhere in the geometry and can range from clusters of grains to whole free surfaces.

$$\Omega_R = \Omega_R^u \cup \Omega_R^\sigma \cup \Omega_R^{user} \cup \Omega_R^+ \tag{3.54}$$

$\mathcal{I}$ is the set of DOFs connected to $\mathcal{F}$ and is not in $\mathcal{F}$

$$\mathcal{I} = \{i \notin \mathcal{F}\,,\ \exists j \in \mathcal{F} \quad K_{ij} \neq 0\} \tag{3.55}$$

By construction, $\mathcal{I} \cup \mathcal{F}$ is the set of all the DOFs of the RID.

The reduced mesh and hybrid hyper-reduction

Finite element shape functions of the reduced mesh are denoted by $(\bar{\psi}_i)_{i=1,...\text{card}(\bar{\mathcal{F}})}$ such that:

$$\bar{\psi}_i(x) = \psi_{\bar{\mathcal{F}}}(x) \forall x \in \Omega_R \tag{3.56}$$

where $\bar{\mathcal{F}}_i$ is the i^{th} index in the set $\bar{\mathcal{F}}$ of the DOFs in RID. A new set $\mathcal{F}^*$ is defined which contains the indices of the reduced mesh such that:

$$\mathcal{F}^* = \{i \in \{1, .., \text{card}(\bar{\mathcal{F}})\} | \bar{\mathcal{F}}_i \in \mathcal{F}\} \tag{3.57}$$

The complement set of $\mathcal{F}^*$ is denoted by $\mathcal{I}$. It contains the DOFs in Ω_R that are connected to $\Omega \backslash \Omega_R$ in the original mesh. Also, for a given RB $\underline{\underline{V}}$, $\underline{\underline{\bar{V}}} \in \mathbb{R}^{\text{card}(\bar{\mathcal{F}} \times \bar{N})}$ is its restriction to the RID:

$$\underline{\underline{\bar{V}}} = \underline{\underline{V}}[\mathcal{F}, :] \tag{3.58}$$

The hybrid hyper-reduced approximation is acquired by adding a few columns of the identity matrix to $\underline{\underline{\bar{V}}}$. Figure 3.5 depicts the scenario clearly where in (a) a 2D linear quadilateral mesh is shown and in (b) the reduced mesh is portrayed. The grey part is where the solely a POD approximation will be done. FE DOFs are added to the part of the mesh which is not connected to the set $\mathcal{I}$ i.e. the red region. Hence, the resulting set of DOFs is denoted by $\mathcal{R}$. Strong coupling ensues in the resulting hybrid approximation and the sub-domain connected to $\mathcal{I}$ is defined as follows:

$$\Omega_{\mathcal{I}} = \cup_{i \in \mathcal{I}} \text{supp}(\bar{\psi}_i) \tag{3.59}$$

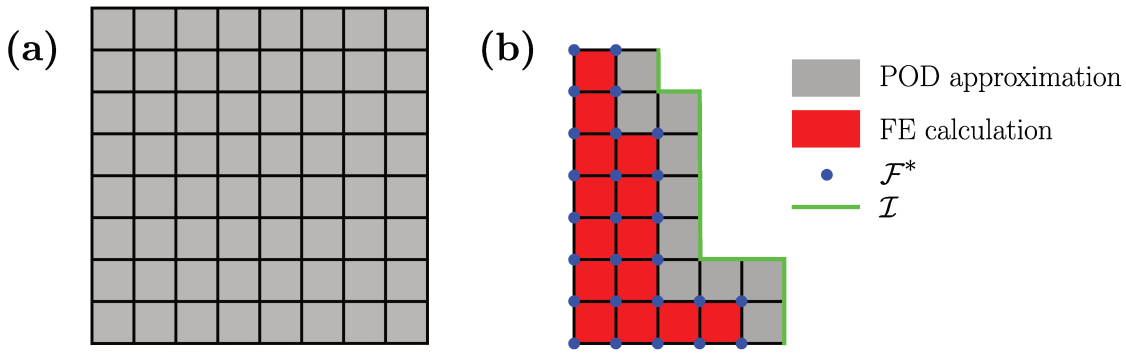

Figure 3.5: (a) A finite element mesh with linear quadilateral elements. (b) The reduced mesh where the green line, the grey and the red part of the mesh, and the blue nodes are related to $\mathcal{I}$, POD approximation, FE calculation, $\mathcal{F}^*$

Then the reduced set of DOFs that is connected to $\mathcal{I}$ takes the form:

$$\mathcal{R} = \left\{ i \in \{1, ..., \text{card}(\bar{\mathcal{F}})\} | \int_{\Omega_{\mathcal{I}}} \bar{\psi}_i^2(x) dx = 0 \right\} \tag{3.60}$$

In the sequel, for the sake of simplicity, it is assumed that the DOFs are ordered such that $\mathcal{R} = \{1, \ldots, \text{card}(\mathcal{R})\}$. The hybrid RB is now denoted by $\underline{\underline{V}}^H$. Using the Kronecker delta (δ_{ij}), it reads:

$$\underline{\underline{V}}^H[i,k] = \delta_{\mathcal{R}_k i} \quad k = 1, ..., \text{card}(\mathcal{R}) \tag{3.61}$$

and

$$\underline{\underline{V}}^H[:, \text{card}(\mathcal{R}) + 1 : \text{card}(\mathcal{R}) + N] = \underline{\underline{V}} \tag{3.62}$$

$\underline{\underline{V}}^H$ couples a FE correction function with the usual POD such that the new RB reads:

$$\underline{\underline{V}}^H = \begin{bmatrix} \begin{bmatrix} \underline{\underline{I}} \\ 0 \end{bmatrix} & \underline{\underline{V}} \end{bmatrix} \tag{3.63}$$

It is assumed that $\text{rank}(\underline{\underline{V}}^H) = N + \text{card}(\mathcal{R})$ is a full column rank matrix. If this is not the case, then in equation 3.62 a smaller N has to be considered to select fewer POD modes until a full column rank matrix is obtained. Hence, it can be

deduced that the hybrid hyper-reduced equations for a linear problem read:

$$(\underline{\underline{V}}^H[\mathcal{F},:])^T\,\underline{\underline{K}}[\mathcal{F},:]\,\underline{\underline{V}}^H\,\underline{b}^R = (\underline{\underline{V}}^H[\mathcal{F},:])^T\,\underline{F}[\mathcal{F}] \tag{3.64}$$

where $\underline{\underline{K}}$ is the tangent stiffness matrix computed on the reduced mesh and $\underline{F}$ is the right hand side of the FE balance equation. An important thing to note here is that when $\Omega_R = \Omega$, then the hybrid hyper reduction formulation is the same as the FE on the full mesh. This can be deduced by the following proof: If $\Omega_R = \Omega$, then $\mathcal{I} = \emptyset$, $\mathcal{F}^* = \mathcal{R} = \{1, ..., N_d\}$ then the reduced mesh is the full field mesh and there is no reduction. Also, all the empirical modes have to be removed from $\underline{\underline{V}}^H$ to get a full rank system of equations, making $\underline{\underline{V}}^H$ an identity matrix. Hence, the hybrid hyper reduction equations are the same as the original FE equations. As a consequence there is no dimensionality reduction.

3.4 Crystal plasticity model and finite element mesh description

The crystal plasticity model is the same as detailed in Chapter 2. The details of the finite element mesh as well as the boundary conditions and computational requirements are stated in the next section.

FE model description

The numerical model was implemented in the implicit finite element solver Z–set package (2013). Literature findings show that the macroscopic representation of a micro-heterogeneous metallic material can be achieved with as few as one hundred grains (Kanit et al., 2003), but matching macroscopic properties is not the goal. The goal here is to have a large enough statistical pool of information so that local material response can be analyzed. Of course computational limitations have to be acknowledged and extremely large polycrystals cannot be used. An aggregate containing equiaxed 1000 grains was generated using the Voronoi tessellation technique with the help of the software VORO++ (Rycroft, 2009). Gmsh was used to mesh the geometry containing 1.1 million nodes and 850,000 reduced quadratic elements 3.6. Each finite element had four Gauss points respectively. The crystal plasticity parameter set employed in this chapter is given in table 3.1

Cubic elasticity	$C_{1111} = 259600$ MPa $C_{1122} = 179000$ MPa $C_{1212} = 109600$ MPa
Critical resolved shear stress	$R_0 = 320$ MPa
Kinematic hardening	C = 100000 MPa D = 1000
Overstress	P = 9 MPa

Table 3.1: The crystal plasticity parameter set being used

Computational requirements

An implicit finite element code (Z–set package, 2013) is used to solve the problem where the global equilibrium is solved using a Newton-Raphson algorithm. Integration of constitutive equations at the Gauss points is performed using the second order Runge-Kutta method with automatic time stepping (Besson et al., 2009). For a crystal plasticity simulation, loading one job of the size being used requires more than 220 gigabytes of RAM. The MPI parallel computing algorithm implemented in Zebulon is used with 24 processors when solving constitutive equations.

Boundary conditions and material parameters for the offline phase

Stress controlled mixed boundary conditions are applied such that the traction vector $\underline{\underline{\sigma}}.\underline{n}$ is prescribed over the whole face:

$$\Sigma_{11} = \text{constant on } Face_1^+$$
$$u_1 = 0 \ \forall x \in Face_1^-$$

Trivial boundary conditions (free boundary conditions) are imposed on all opposing faces i.e.

$$\sigma_{21}n_1 = \sigma_{31}n_1 = 0 \ \forall x \in Face_1^+ \cup Face_1^-$$
$$\sigma_{12}n_2 = \sigma_{22}n_2 = \sigma_{32}n_2 = 0 \ \forall x \in Face_2^+ \cup Face_2^-$$
$$\sigma_{13}n_3 = \sigma_{23}n_3 = \sigma_{33}n_3 = 0 \ \forall x \in Face_3^+ \cup Face_3^-$$

3.5 Setup

A thousand grain polycrystal was chosen as an example where figure 3.6 shows a meshed finite element geometry with mixed traction boundary conditions. The finite element mesh consists of 1.1 million nodes and 860000 reduced C8D10 quadratic tetrahedral elements. Each element consists of four Gauss points. The crystallographic orientations chosen were randomly distributed throughout the polycrystal. Figure 3.6 also shows the first ten stress strain cycles which were simulated using Σ_{11} = 1000 MPa and R_{Σ} = -0.7. The same ten cycles are used as the offline training phase for the hyper reduced model.

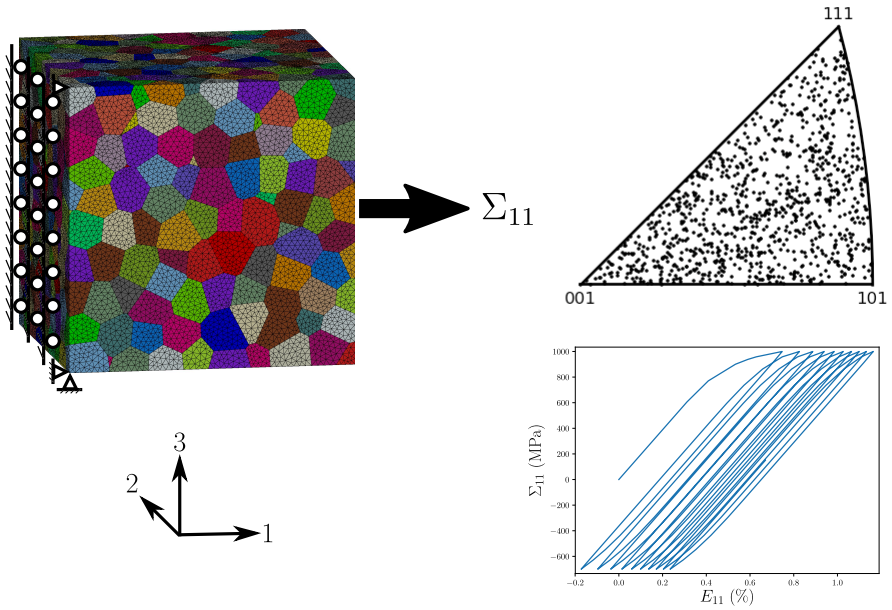

Figure 3.6: A 1000 grain meshed microstructure with prescribed boundary conditions, the inverse pole figure and the corresponding stress strain response for the first 10 cycles.

Figure 3.7 shows the proper orthogonal modes of displacement and stress. As anticipated, the magnitude of singular values exponentially decreases with the number of modes. It is also important to note that the magnitude of the singular values is displayed in a log-scale, and a dotted red line represents the cut-off for the selected POD modes. For displacement 9 and for stress, 20 modes are considered, and this cutoff is arbitrary and dependent on the user. By looking at the contour plot of the modes in both cases it can be seen that the first few modes are homogeneously distributed while the later ones are high gradient modes. Also the modes of displacement decrease in magnitude more rapidly as compared to the

modes of stress implying that most information for displacements can be retained in a few orthogonal selections. It is also precised that POD modes do not have units and their magnitudes are obtained according to an L^2 norm in space.

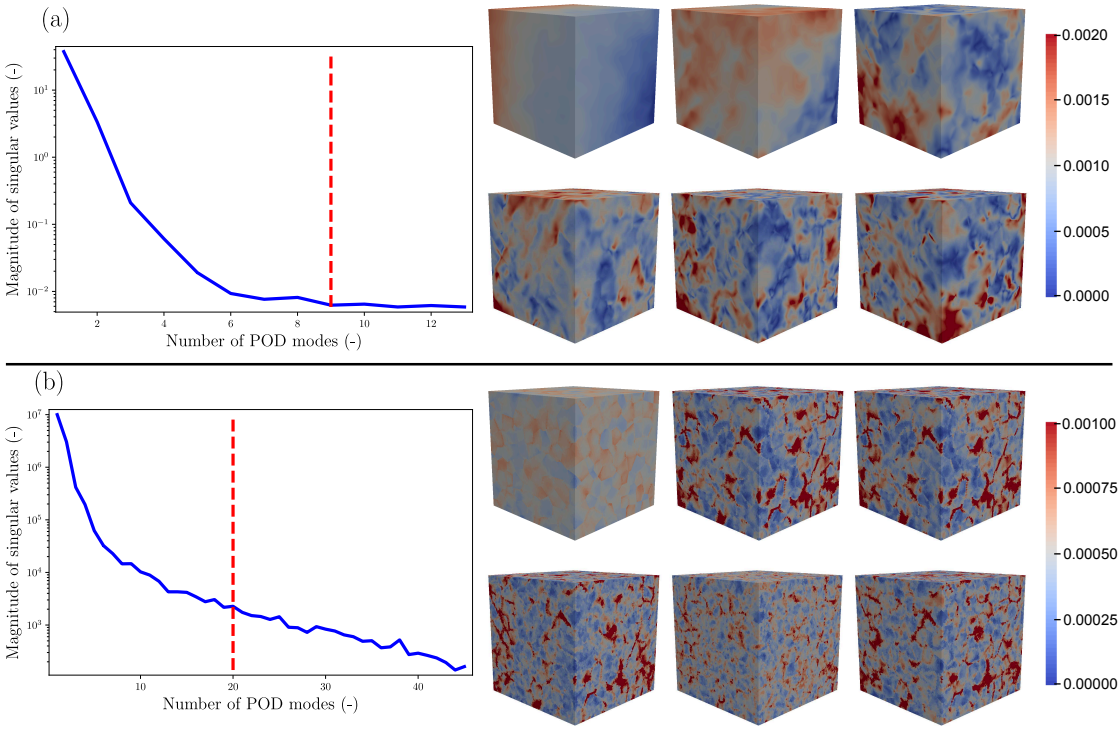

Figure 3.7: Selection of the first (a) 9 POD modes of displacement and (b) 20 POD modes of stress for the reduced basis. Only the first six modes are plotted for both cases.

Figure 3.8 (a) shows the reduced mesh constructed using the selected POD modes where the red part signifies the zone of interest which is provided by the user while the grey part is the region provided by the DEIM algorithm after considering the POD RB of displacements and stresses. The part of the finite element mesh provided in the zone of interest depends on which part of the mesh is the most critical according to the user. The hybrid HROM solution is computed on the RID and is then projected over the whole mesh. Hence, the retained region in the RID will then have the best predicted solution followed by other regions of the mesh. In the case being presented, the face of the geometry where pressure is being applied is included in the zone of interest, because this region experiences the most strain under a tensile load. Hypothetically, under a cyclic loading scenario, strain should also incrementally segregate on this part of the geometry. In figure 3.8 (b) two distinct regions can be observed in the mesh where the red part represents the

region where the usual hyper-reduction will be used while the grey part of the geometry represents the regions where a finite element correction function is computed. It should be noted that the hyper-reduced scheme enables the integration of constitutive equations only on the elements shown in figure 3.8 (both red and grey) while the results over the entire domain are recovered as a post-process by doing a product of the resulting reduced coordinate at the end of the simulation.

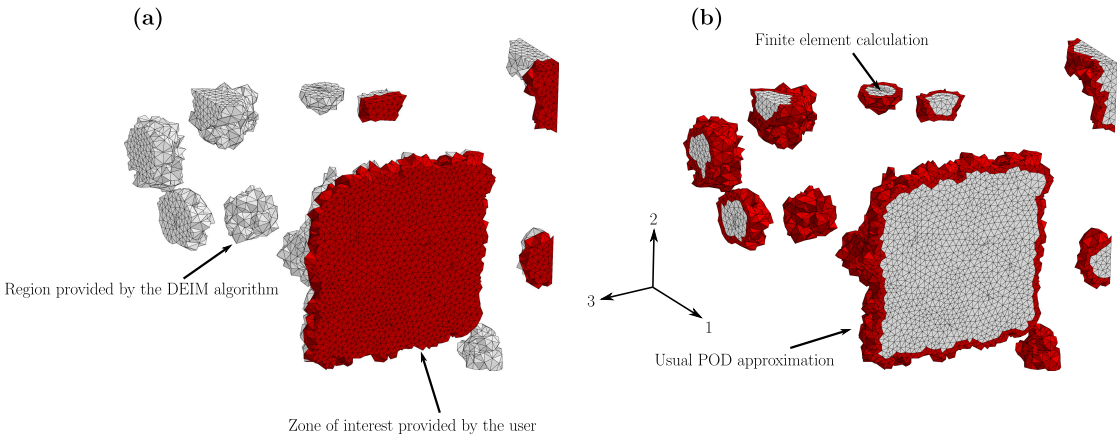

Figure 3.8: Reduced mesh showing the (a) zone of interest provided by the user (red) and the region provided by the DEIM algorithm by considering the reduced bases (grey), (b) region where the finite element calculation is done (grey), and where the usual POD is approximated (red).

3.6 Results

After constructing the RB and the gappy finite element mesh using an offline learning phase of just 10 cycles, computations were performed on the reduced domain for one hundred stress controlled cycles. The loading was kept the same at R_Σ = -0.7 and Σ_{11} = 1000 MPa. To compare the results, a full field simulation was also run for 100 cycles. Figure 3.9 shows the macroscopic stress (Σ_{11}) vs strain (E_{11}) response of the three cases, hybrid hyper-reduction, hyper-reduction and the full field for comparison. To avoid clutter, responses are plotted only at cycles 1 and 100. It can be seen that the hybrid approach is much better than the usual hyper-reduction at cycle 100. One important point to be noted is that, as seen in figure 3.8, even at cycle 1 the hybrid and HROM approximations are not the same as the full field response, although the RB has been constructed using the first ten cycles, and theoretically, in this domain the results should be exact. The reason for this phenomenon is that the RB was constructed by selecting only nine

modes; if more modes were selected, the results tend to be more precise but this also gives rise to the problem of over-fitting which penalizes the stability of the hyper-reduced order models for long cyclic simulations.

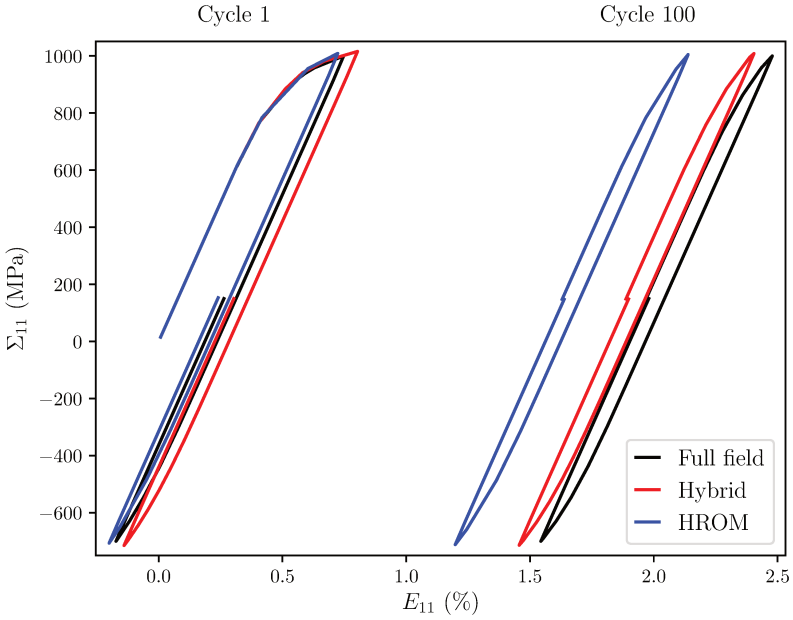

Figure 3.9: Macroscopic stress vs strain response for cycle 1 and cycle 100 for the full field as well as the Hybrid and HROM approximation

The local results presented in figures 3.10, 3.11, 3.12 and 3.13 pertain to one time step taken at the tensile peak of the hundredth cycle for all three cases i.e. the Hybrid, HROM and the full field simulation. Figure 3.10 shows the Gauss point distribution curves for ε_{11} and σ_{11}. The strain distribution plot shows that locally the hybrid approach is much better than the usual HROM. This is observed by the proximity of the red, hybrid, curve to the reference, black, curve while the blue, HROM, curve is further offset from the reference curve. A quantification of the results is also presented in figure 3.10 where the standard deviation s and the macroscopic mean μ are stated for the three cases. The standard deviation in the longitudinal strain ε_{11} at the tensile peak of the hundredth cycle is the highest in the full field simulation $s = 1.029$, closely followed by the hybrid approximation $s = 0.9932$ and then the HROM $s = 0.8548$. A similar trend can be seen in the mean values of the three cases where the full-field simulation has the highest values of $\mu = 2.5$ %, followed by the hybrid approximation $\mu = 2.4$ %, and finally the HROM estimation with $\mu = 2.1$ %. On the other hand, the probability distribution curves for σ_{11} do not have a significant difference between the three cases. This observa-

tion comes from the notion that in crystal plasticity each grain has its own stress field which is comparatively easy to approximate. Also Σ_{11} is the applied boundary condition, so its value at the macroscopic scale is already known. E_{11} on the other hand is the evolving quantity and it is much more difficult to approximate. Also, in crystal plasticity strains tend to segregate at preferred locations and the prediction of these regions is more difficult as compared to predicting stress. It is clear from figure 3.10 that the usual HROM introduces an important bias on strain predictions whereas the hybrid approach preforms way better. These results have been obtained by considering the full mesh after applying the Gappy POD reconstruction of the hyper-reduced predictions.

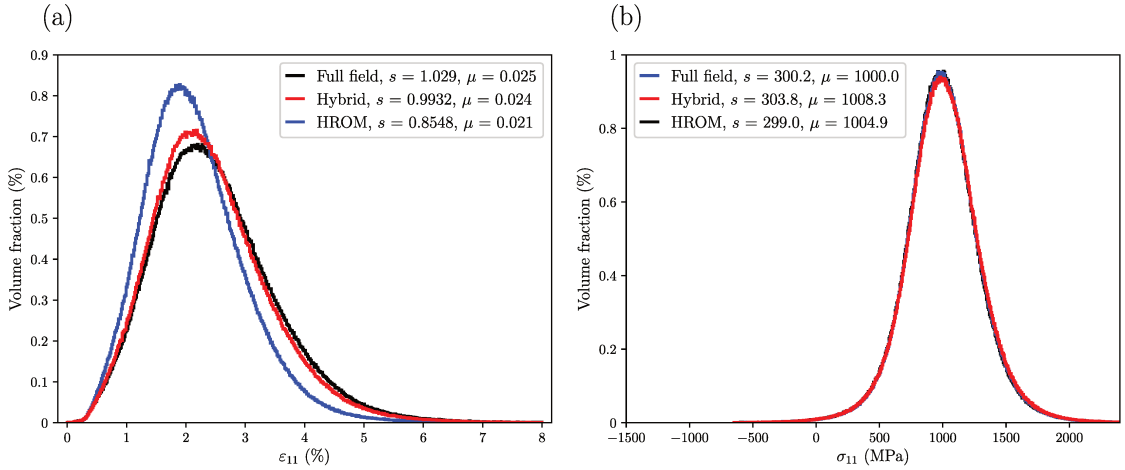

Figure 3.10: Gauss point distribution for ε_{11} and σ_{11} at the tensile peak of the 100th cycle. The standard deviation (s) and mean (μ) is also shown for each case respectively.

Figure 3.11 shows the (a) strain and (b) stress per grain collected at the tensile peak of the hundredth cycle for the predicted vs full field simulated plots for Hybrid and the usual HROM approximation. A 95 % prediction interval is also plotted for both cases. Strain shows a clear deviation from full field simulations, which can be judged by the slope of the regression line drawn between the points. For HROM this slope corresponds to 0.82 while for the Hybrid approach this slope is equal to 0.95 indicating the superiority of the later. On the other hand, stress can be seen to be easier to predict as both the HROM and the Hybrid approach give a close prediction to the full field simulation result. The slope of the regression line is 1.02 and 1.04 for HROM and Hybrid respectively. For both cases, the prediction interval generally captures most grains, as it can be seen that most points fall with the bounded shaded blue and red regions.

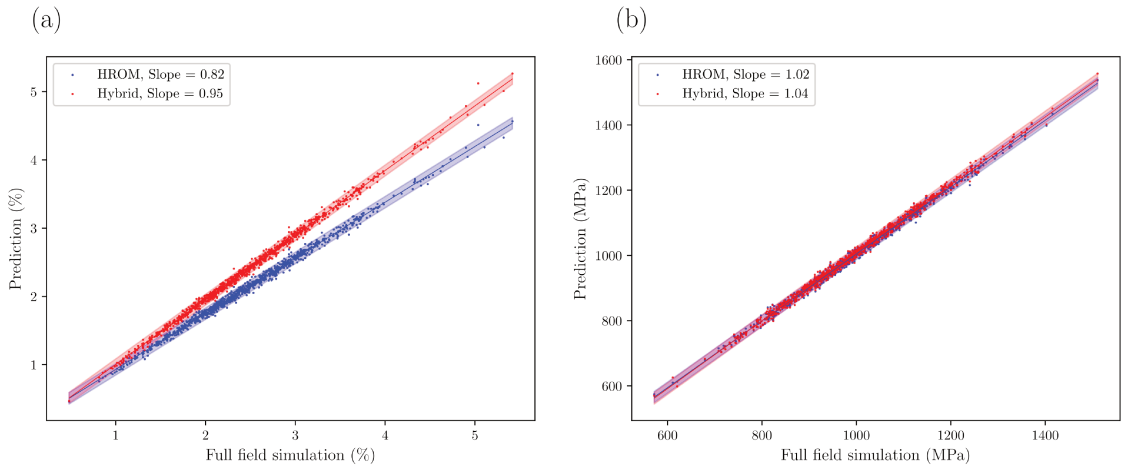

Figure 3.11: Grain level distribution for ε_{11} and σ_{11} at the tensile peak of the 100th cycle. A prediction interval of 95 % is plotted for both cases.

Figure 3.12 shows the contour plots for ε_{11}, where the first line shows the full field, HROM and Hybrid approximation. Error maps have been shown in the second line of figure 3.12, and it can be seen that HROM has a considerably higher error distribution as compared to the Hybrid approximation. Multiple regions with errors as high as 20% can be observed for the HROM simulation whereas for the Hybrid case the errors are comparatively low. Figure 3.13 shows the contour plots for σ_{11} where the Hybrid and HROM show a very close approximation to the full field simulation. Moreover, the error plots in the second line of figure 3.13 show minimal values.

The computational requirements to run 100 cycles for the three cases can be viewed in table 3.2 where the full field simulation takes 880 hours and 221.2 gigabytes of RAM to run. It should be noted that the number of parallel processors utilized in this study have been arbitrarily chosen. For the full field simulation 24 processors were selected because that is the maximum number available on each cluster node. For the HROM and Hybrid simulations, one processor was used each and the RAM required for both cases was 1.5 Gbs. The RAM required to launch a simulation is the bottle neck in terms of computational resources required, and in this case 147 times less RAM is required to run the reduced simulations. The computational time for the Hybrid case was 450 hours while for HROM it took 70 hours to complete one hundred cycles. Although the time to run the hybrid simulation was more than six times higher, much better prediction in strain was achieved by using the hybrid approach.

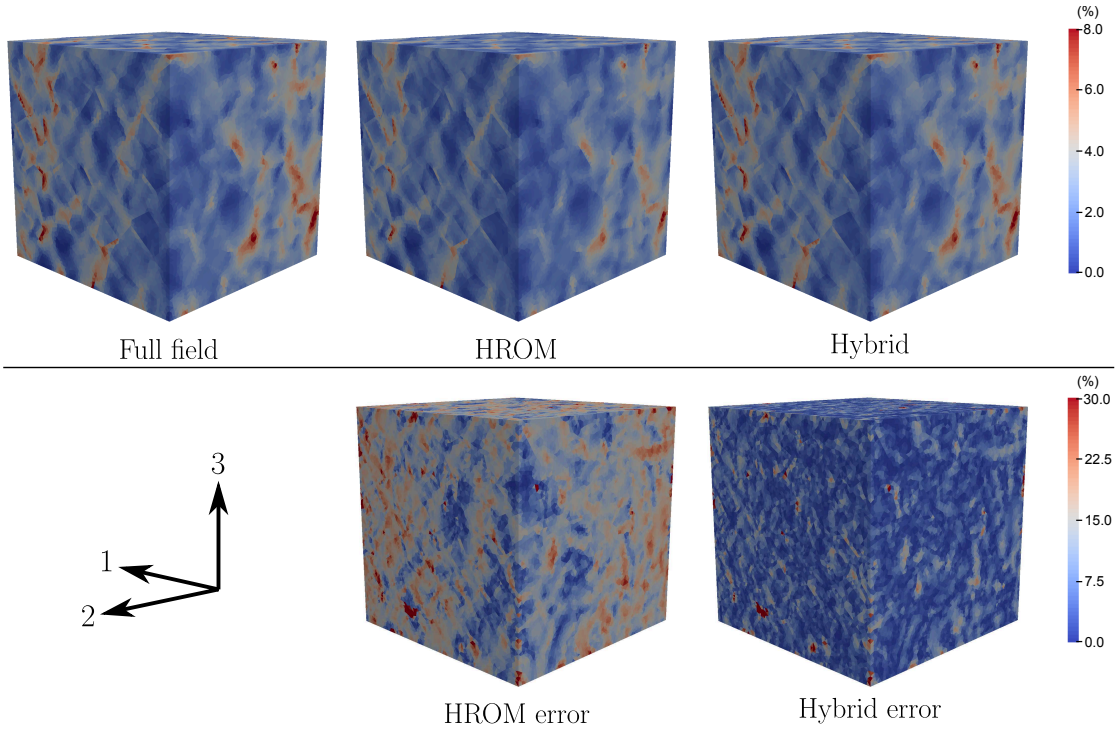

Figure 3.12: ε_{11} contour plots at the tensile peak of the 100th cycle for the full field, hyper-reduced (HROM), and hybrid hyper-reduced (hybrid) simulation. In the second line, error plots for the HROM and the Hybrid are plotted.

-	Full field	HROM	Hybrid
Nodes	1174719	57874	57874
Elements	859848	36041	36041
Computation time	880 h	70 h	450 h
Parallel processors	24	1	1
RAM	221.2 Gbs	1.5 Gbs	1.5 Gbs

Table 3.2: Finite element mesh details and the resources needed to run the full field (FF), hyper-reduced (HROM) and hybrid hyper-reduced (Hybrid) simulations

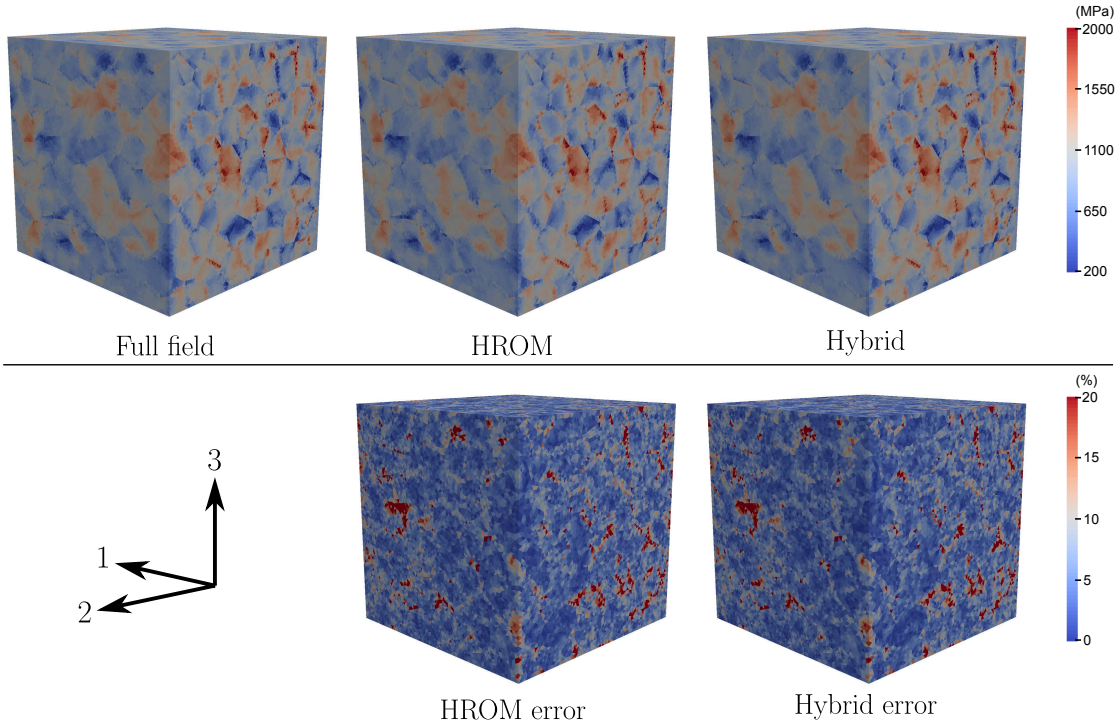

Figure 3.13: σ_{11} contour plots at the tensile peak of the 100th cycle for the full field, hyper-reduced (HROM), and hybrid hyper-reduced (hybrid) simulation. In the second line, error plots for the HROM and the Hybrid are plotted.

3.7 Conclusion

In this chapter the hybrid hyper-reduced formulation has been presented and applied to finite element polycrystal aggregate simulations. The capabilities of the reduced simulation are explored using the macroscopic stress strain plot, local materials point statistics as well as visual contour plots. Results show the superiority of the hybrid over the usual hyper-reduction method when an accurate prediction is required. In terms of computational time, the hybrid approach is six times costlier than the HROM. Resources required to launch the Hybrid and the HROM simulations are identical and around a hundred and fifty times less than their full field counter-part. Without changing the local constitutive equation, a hybrid hyper-reduced simulation is quite accurately able to characterize local nonlineaties. This type of study is beneficial when the asymptotic mechanical response, such as strain ratcheting, is under question. It is also shown that errors in stress prediction are minimal as compared to strain.

As a next step, this type of formulation may be applied to run large scale simulations with differing local constituents. This will be beneficial in assessing the preferred locations of plasticity segregation. Accurate parametric studies in polycrystal aggregates is also a direction which can be pursued. Lastly, error estimators to approximate cyclic errors can also be developed in this context.

Chapter 4

Parametric simulations in crystal plasticity

4.1 Résumé

Il est bien connu que la réponse d'un monocristal est anisotrope, même si la réponse macroscopique d'un agrégat de ces cristaux ne l'est pas. Une telle anisotropie locale oblige les simulations de plasticité cristalline à être extrêmement lourdes, tant en termes de stockage que de temps de calcul. L'hyper-réduction vise à limiter l'utilisation de ces ressources en convertissant le modèle détaillé en un modèle réduit (ROM) en supposant que les variables d'état appartiennent à un sous-espaces fonctionnel réduit et, ce faisant, de réduire le nombre de variables d'état. Le cadre de la POD qui provient de l'analyse statistique des données vectorielles est adopté. On peut l'imaginer comme la mesure d'un certain événement un nombre de fois n, chaque mesure $\underline{x}_i, i = 1, ..., n$ étant un vecteur contenant un grand nombre, m, d'entrées, c'est-à-dire $\underline{x}_i \in \mathbb{R}_n$ (Dans ce cas, m est le nombre d'incréments de la simulation par éléments finis). L'objectif est de trouver les similitudes et les interdépendances entre les données extraites et de les réduire à un nombre beaucoup plus petit. Dans le cadre de la POD, formellement, toutes les solutions possibles d'équations paramétriques devraient être considérées, pour toutes les valeurs de paramètres dans un espace paramétrique $\mathcal{D}$. Mais dans la plasticité cristalline, il n'est pas possible de prendre en compte toutes les microstructures possibles pour un élément de volume représentatif donné. Par conséquent, un protocole d'apprentissage automatique est proposé qui nous permet d'effectuer des analyses

statistiques en recourant à des ROMs très rapides.

Les paramètres sont divisés en trois ensembles, c'est-à-dire les paramètres microstructuraux utilisés pour générer des milieux aléatoires, y compris le maillage, les paramètres liés aux conditions aux limites appliquées au volume élémentaire représentatif, et tous les autres paramètres. Toutes les prédictions possibles sont considérées comme des tenseurs de second ordre ayant un rang bas. Ici, les paramètres et la variable temps sont regroupés en une seule variable multidimensionnelle. En raison des paramètres microstructuraux, on ne s'attend pas à ce que le rang de ce tenseur soit suffisamment faible pour générer des approximations de base réduite efficaces.

Dans l'approche présentée, l'espace de paramètres inclut les orientations cristallographiques, les distributions de voisinage et de taille des grains, le type de chargement, les conditions aux limites, les paramètres du modèle phénoménologique et, pour résoudre ces problèmes par éléments finis, la taille du maillage et sa densité. L'espace paramétrique implique que les informations collectées lors d'une étape hors ligne, sont valables pour une variation limitée des paramètres autour des points échantillonnés dans l'espace choisit. Cet espace peut être augmenté mais alors le domaine réduit ne sera pas "réduit" et simultanément les imprécisions d'échantillonnage augmenteront.

4.2 Introduction

It is well known that the response of a single crystal is anisotropic; even if the macroscopic response of an aggregates of these crystals is not. Such local anisotropy compels crystal plasticity simulations to be extremely heavy, both in terms of storage as well as computational time. Hyper reduction aims to limit the use of such resources by converting the detailed model into a reduced order model (ROM) assuming that the state variables belong to a restricted functional subspace; and in the process reducing the number of independent state variables. The framework of POD is adopted which originates from the statistical analysis of vector data. It can be imagined as measuring a certain incident an n number of times, each measurement $\underline{x}_i, i = 1, ..., n$ being a vector containing a large number, m, of entries i.e. $\underline{x}_i \in \mathbb{R}_n$ (In this case m is the number of increments of the finite element simulation.). The objective is to find the similarities and inter-dependencies in the extracted data and reduce it to a much smaller number. In the framework of POD, formally, all possible solutions of parametric equations should be considered, for

all parameter values in a parametric space $\mathcal{D}$. But in crystal plasticity it is not possible to account for all possible microstructures for a given representative volume element. Therefore, a machine learning protocol is proposed which enables us to run statistical analysis by resorting to fast hyper ROMs.

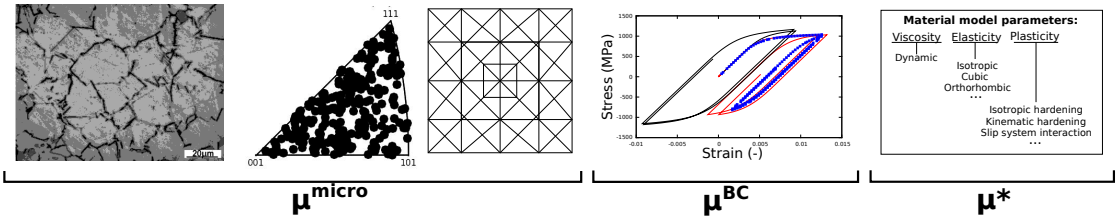

Figure 4.1: Dividing the parameter space into three components: $\underline{\underline{\mu}} = [\underline{\mu}^{micro}, \underline{\mu}^{BC}, \underline{\mu}^{\star}]$

As shown in figure 4.1, parameters are split into three sets i.e. the microstructural parameters used to generate randomized media including the mesh, the parameters related to the boundary conditions applied to the RVE, and all other parameters. Then, $\underline{\underline{\mu}} = [\underline{\mu}^{micro}, \underline{\mu}^{BC}, \underline{\mu}^{\star}]$, where $\underline{\mu}^{micro}$ is the vector of microstructural parameters, $\underline{\mu}^{BC}$ is the vector of boundary conditions parameters, and $\underline{\mu}^{\star}$ is the vector related to all the remaining parameters. All possible predictions are viewed as second order tensors having a low rank. Here parameters and the time variable are grouped in a single multidimensional variable in order to define this second order tensor: $\underline{\underline{u}}(\underline{z}, \underline{\theta}) = \underline{\underline{u}}(\underline{z}, t; \underline{\mu}), \underline{\theta} = (t, \underline{\mu})$. By sampling the possible values of $\underline{\theta}$ the rank of the tensor can be evaluated. But here, because of the microstructural parameters the rank of this tensor is not expected to be small enough to generate efficient RB approximations.

In the presented approach the parameter space includes crystallographic orientations, grain neighborhood and size distributions, loading type, boundary conditions, the phenomenological model parameters, and when solving these problems using finite elements, the mesh size and its density. The parameter space implies that the information collected during an offline stage, is valid for a limited variation of parameters around sampled points in the prescribed space. This space can be increased but then the reduced domain will fail to be "reduced" and simultaneously sampling inaccuracies will increase in the reduced setting. This chapter is organized in the following manner. Section 4.3 will present the incremental POD formulation as well as the characterization of the microstructural space ($\underline{\mu}^{\mathbf{micro}}$). Section 4.4 will explore the boundary conditions ($\underline{\mu}^{\mathbf{BC}}$), as well as the constitutive equation parameter sets ($\underline{\mu}^{*}$). This will be followed by the conclusion in Section 4.5.

4.3 Testing the microstructural space

The contents of the following part are based on the idea of an incremental POD (Brand, 2002; Ryckelynck et al., 2006), where the intention is to expand the existing subspace spanned by the basis functions. The motivation is to create a huge RB which may be able to simulate datasets without new offline trainings. As stated in the previous chapter, all simulation results are stored in a matrix $\underline{\underline{Q}}$. An existing POD done on the matrix of simulation results takes the form:

$$\underline{\underline{Q}} = \underline{\underline{V}}\underline{\underline{\gamma}} + error,\ \ \underline{\underline{V}}^T\underline{\underline{V}} = \underline{\underline{I}}_N,\ \ \max(|\lambda(error)|) < \sqrt{\epsilon_{POD}}\max(|\lambda(\underline{\underline{Q}})|), \quad (4.1)$$

where $\max(|\lambda(\underline{\underline{Q}})|)$ is the maximal singular value of $\underline{\underline{Q}}$. Now lets say that new is obtained and the RB has to be extended by adding a new snapshot at the end of each time step: $[\underline{\underline{Q}}, \underline{\underline{q}}]$. The reduced coordinate $\underline{\underline{q}}$ will read:

$$\underline{\underline{\beta}} = \underline{\underline{V}}^T\underline{\underline{q}}. \quad (4.2)$$

The orthogonal residual of the projection on $\underline{\underline{V}}$ will read:

$$\delta\underline{\underline{q}} = (\underline{\underline{I}} - \underline{\underline{VV}}^T)\underline{\underline{q}},\ \ p = \sqrt{\delta\underline{\underline{q}}^T\delta\underline{\underline{q}}}, \quad (4.3)$$

such that:

$$[\underline{\underline{V}}\underline{\underline{\gamma}}, \underline{\underline{q}}] = [\underline{\underline{V}}, \delta\underline{\underline{q}}/p]\begin{bmatrix}\underline{\underline{\gamma}} & \underline{\underline{\beta}} \\ 0 & p\end{bmatrix}. \quad (4.4)$$

Hence, if $||\delta\underline{\underline{q}}||_\infty > \epsilon_R||\underline{\underline{q}}||_\infty, \epsilon_R = 10^{-6}$, a new eigen-decompositon is performed on an $(N+1)\times(N+1)$ matrix such that:

$$\underline{\underline{B\Lambda}} = \begin{bmatrix}\underline{\underline{\gamma}} & \underline{\underline{\beta}} \\ 0 & p\end{bmatrix}\begin{bmatrix}\underline{\underline{\gamma}} & \underline{\underline{\beta}} \\ 0 & p\end{bmatrix}^T\underline{\underline{B}} + error',\ \ \max(|\lambda(error')|) < \sqrt{\epsilon_{POD}}\max(|\lambda(\underline{\underline{Q}})|), \quad (4.5)$$

the updated POD will read:

$$[\underline{\underline{Q}}, \underline{\underline{q}}] = \underline{\underline{\tilde{V}}}\underline{\underline{\tilde{\gamma}}} + \tilde{error}\underline{\underline{\tilde{V}}} = [\underline{\underline{V}}, \delta\underline{\underline{q}}/p]\underline{\underline{B}}\underline{\underline{\tilde{\gamma}}} = \underline{\underline{B}}^T\begin{bmatrix}\underline{\underline{\gamma}} & \underline{\underline{\beta}} \\ 0 & p\end{bmatrix}, \quad (4.6)$$

otherwise $||\delta \underline{q}||_\infty \leq \epsilon_R$, then the reduced matrix $\underline{\underline{V}}$ is not updated.

To test this, as shown in figure 4.2, a geometry is selected where a fixed mesh is prescribed with 330,000 DOFs and 256 equiaxed grains. One face of the geometry is constrained while imposing mixed strain controlled boundary conditions on the opposite face. A macroscopic strain of is 1.5 % is applied to the geometry. The following procedure is employed:

1. begin with a parameter space containing one fixed mesh and geometry containing 256 grains
2. run one hundred tensile finite element simulations, each with a different set of 256 crystallographic orientations
3. extract the reduced basis from each simulation and merge them

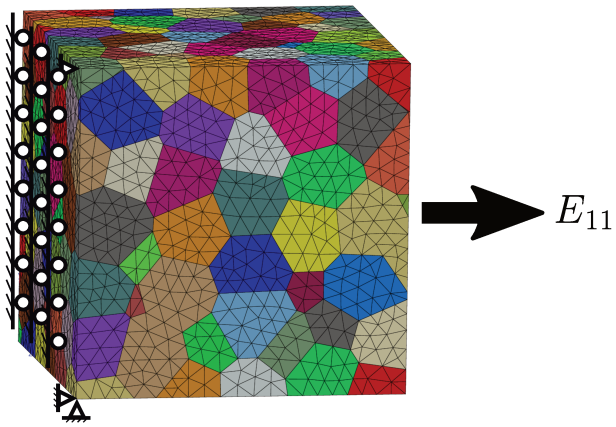

Figure 4.2: The starting mesh containing 256 equiaxed grains, 110,000 nodes and quadratic elements

In theory, this should give a reduced basis which contains information from a hundred microstructures, capable of predicting at least the one hundred microstructures fed to it. Figure 4.3 shows the whole process where this information is added from microstructures with different local orientations. The right hand plot shows the stress vs strain curves for all one hundred microstructures.

One important feature to note in figure 4.3 is that the RB $\underline{\underline{V}}$ gets bigger with the addition of more microstructural information. As can be recalled from the previous chapter, the RB determines the least number of nodes which may exist in

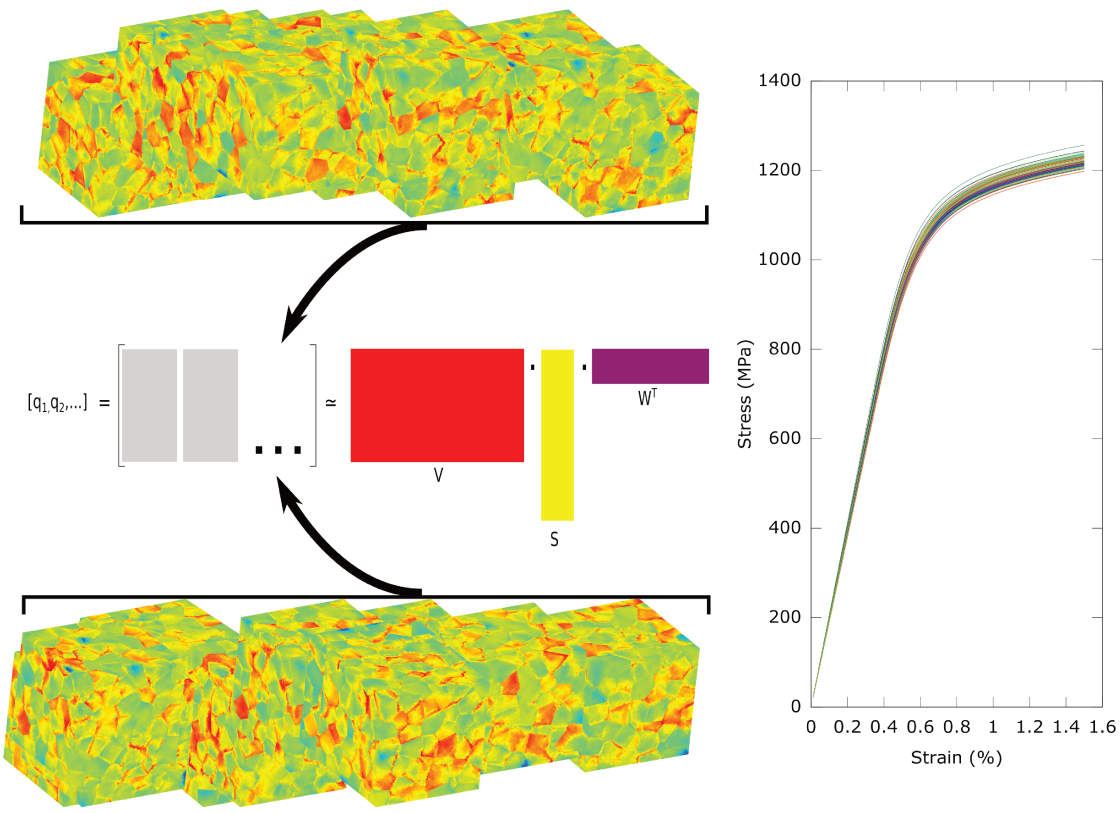

Figure 4.3: Extracting a reduced basis from several microstructures. The stress strain curves resulting after testing each RVE are shown on the right.

One microstructure

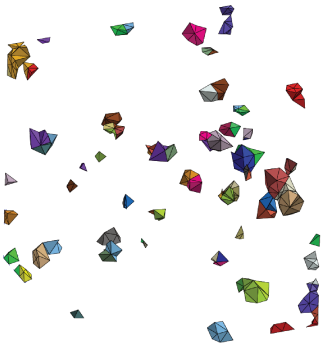

Two microstructures

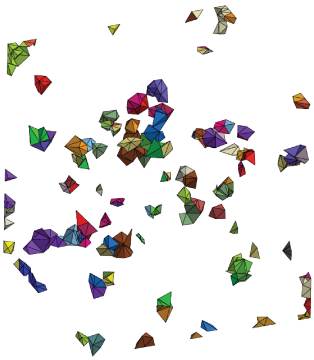

Five microstructures

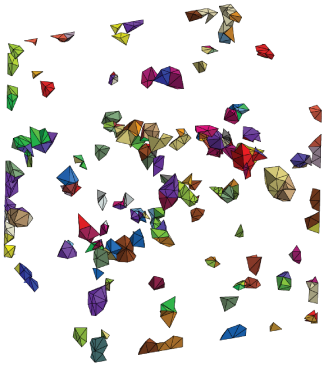

Ten microstructures

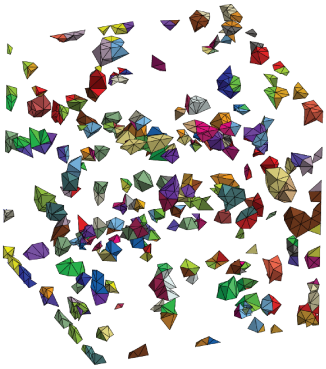

Twenty-five microstructures

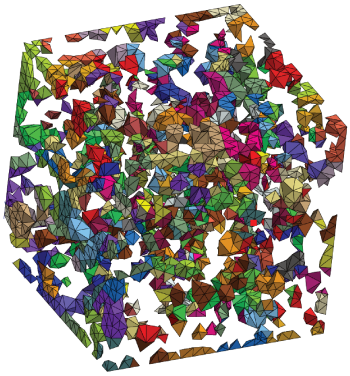

One hundred microstructures

Figure 4.4: Reduced integration domains (RIDs) after merging different numbers of reduced bases.

the reduced mesh. Figure 4.4 illustrates this where reduced meshes after merging different numbers of computation are shown.

After the creation of such reduced meshes, shown in figure 4.4, an orientation set is taken which exists in all the RB and its tensile response is simulated. Figure 4.5 shows the results where it can be clearly observed that with an increase in parameter space, the simulations, even in the elastic region do not give correct predictions. More importantly, with more parameters, the calculations tend to diverge and the RID becomes large. In essence, an important discovery is that with such a huge parameter space, not only does the RB get bigger, it also gives extremely inaccurate results. The conclusion of this section is that microstructural parameters ($\underline{\mu}^{\mathbf{micro}}$) are not reducible using the current setting of hyper reduction,

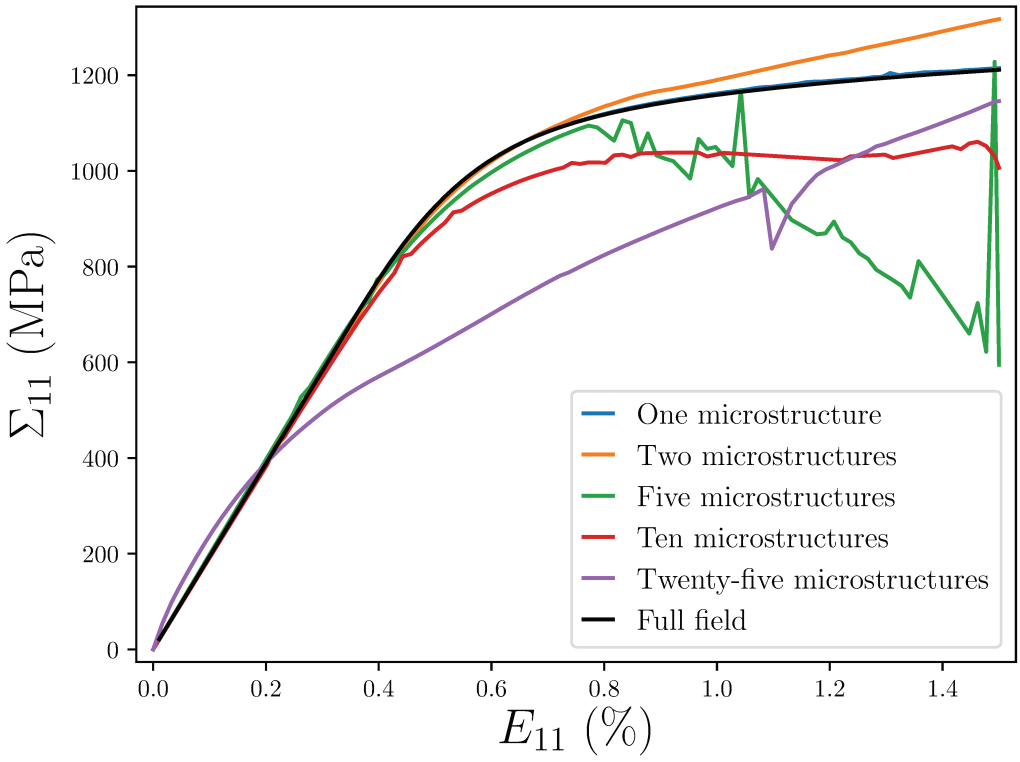

Figure 4.5: Stress vs strain response of the reduced simulations after merging different reduced basis. A full field simulation is also plotted for comparison purposes.

4.4 Testing boundary conditions and parameter sets

In the following three examples are shown which explore the capabilities of the ROM for crystal plasticity finite element simulations. A thousand grain polycrystal is chosen as an example where figure 4.6 shows a meshed finite element geometry with mixed displacement based boundary conditions. The finite element mesh consists of 1174719 nodes and 859848 reduced C8D10 quadratic tetrahedral elements. Each element consists of four Gauss points. The crystallographic orientations chosen were randomly distributed throughout the polycrystal. Figure 4.6 also shows the first ten stress vs strain cycles which were simulated using $E_{11} = 1.0$ % and $R_\Sigma = 0.0$. The same ten cycles were used as the offline training phase for the hyper-reduced model.

4.4.1 Case 1: Changing the macroscopic boundary conditions

In structural simulations often different types of boundary conditions have to be simulated. Especially in context to micro-heterogeneous materials different macroscopic boundary conditions give a different local response because of the nonlinear evolution of micro hardening variables. In this example a different macroscopic load is applied as compared to the offline phase i.e both simulations had $R_E = 0.0$, while the maximum strain for the online phase was 0.8% as compared to the offline phase of 1.0%. Figure 4.7 shows the results where the offline and online case are presented. For comparison purposes a full field simulation for the online phase is also shown. The online simulation can be seen to be in good conformance with the full field result.

4.4.2 Case 2: Changing the constitutive parameters

Constitutive parameters of phenomenological equations governing the behavior of a single crystal are difficult to calibrate. Adding to that is the fact that after a certain crystal plasticity parameter set has been employed, changing even a single parameter can lead to a different evolution of local hardening. Especially when running cyclic simulation, a change in parameter set can lead to great variations

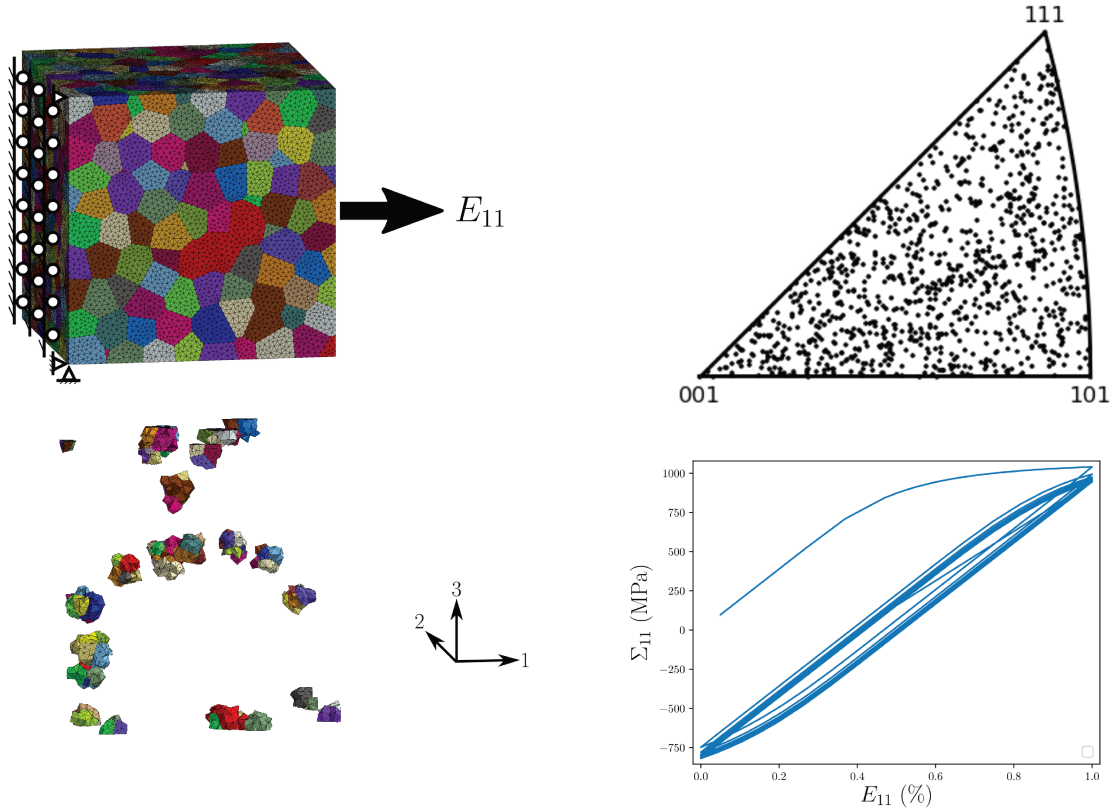

Figure 4.6: A 1000 grain meshed microstructure with prescribed boundary conditions, the inverse pole figure and the corresponding stress strain response for the first 10 cycles. 10 POD modes of displacement and 20 POD modes of stress were considered and the resulting reduced mesh is shown on the bottom left.

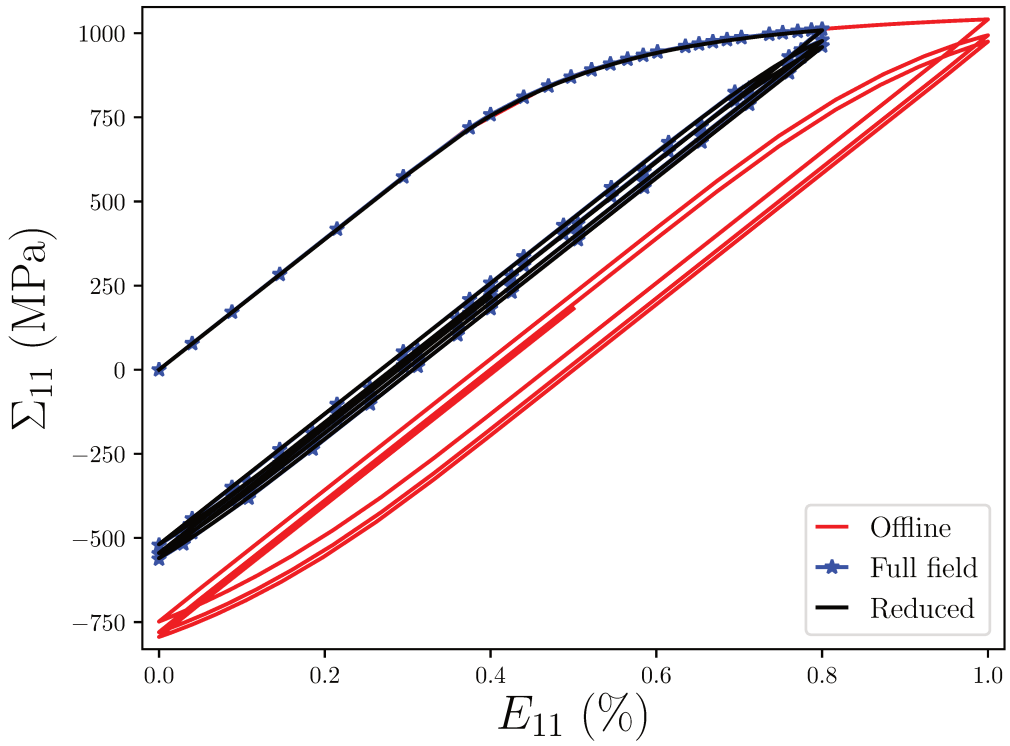

Figure 4.7: Stress strain response for a reduced and full field simulation using a different amplitude and loading ratio than the offline phase. The first three cycles are shown for all cases.

in the nonlinear evolution of plasticity. Another point is that in the context of crystal plasticity where complex phenomenological laws are used at the local scale, different constitutive parameter sets may yield the same macroscopic response. This can lead to a completely different interpretation of local mechanics resulting in macroscopic hardening. In light of this motivation, table 4.1 shows the parameters used in the offline stage as well as those used in the online stage. The initial resolved shear stress and the kinematic hardening parameter of the online case are changed by about 30 %. Figure 4.8 shows the stress vs strain response of the online and offline simulations. The simulations show good conformance and it is concluded that the reduced domain is valid for a large change in constitutive parameters.

Offline parameters	Online parameters
C_{1111} = 259600.0 MPa	C_{1111} = 259600.0 MPa
C_{1122} = 179000.0 MPa	C_{1122} = 179000.0 MPa
C_{1212} = 109600.0 MPa	C_{1212} = 109600.0 MPa
R_0 = 320.0 MPa	R_0 = 220.0 MPa
C = 100000.0 MPa	C = 80000.0 MPa
D = 1000.0	D = 1000.0
K = 9	K = 9

Table 4.1: Parameters used for extracting the reduced basis (offline parameters), and those used to predict the material response (online parameters).

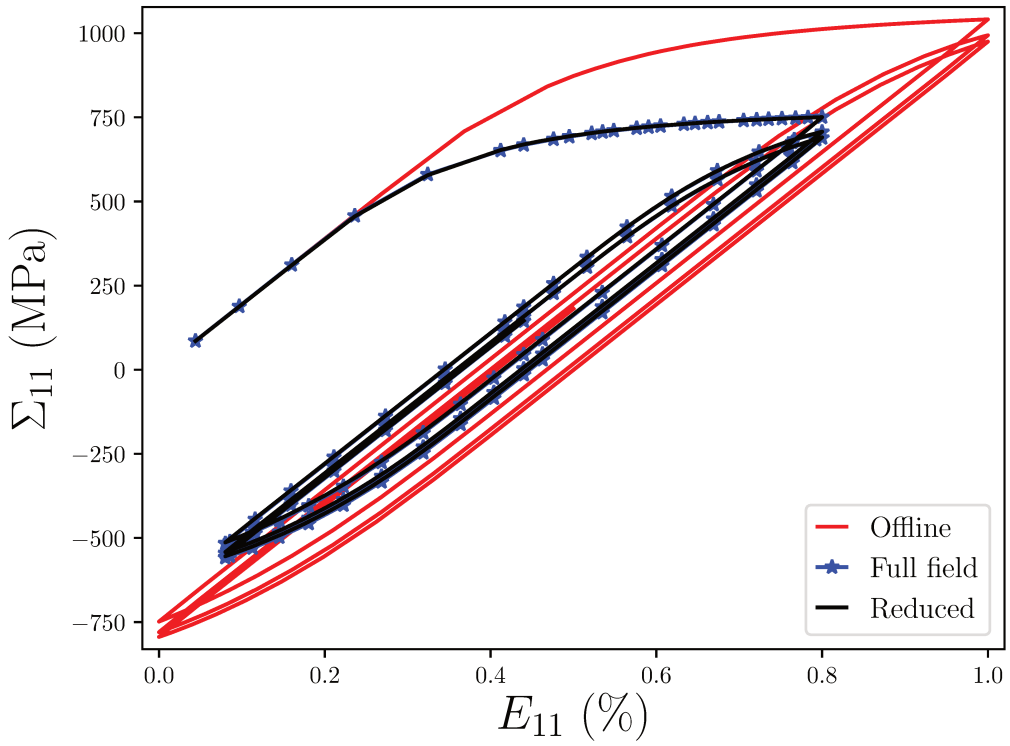

Figure 4.8: Stress vs strain response for a reduced and full field simulation using a different constitutive parameter set than the offline phase. The first three cycles are shown for all cases.

4.4.3 Case 3: Model reduction of large scale simulations

In low cycle fatigue long cyclic simulations are sometimes necessary to check the stabilized response of the material. This example shows one practical need for running parametric simulations in crystal plasticity. As shown in chapter 2, under asymmetric cyclic strain boundary conditions, different strain amplitudes give differing stabilized mean stress regimes. As reported by multiple authors (Morrow et al., 1974; Kwofie and Chandler, 2001; Christ et al., 1997; Xia et al., 1996; Yuan et al., 2016), the retention of mean stress in a cyclically loaded component causes an early onset of failure. Modeling such a response using crystal plasticity FEM enables the elaboration of local effects which lead to a retention of mean stress.

The offline phase is shown in figure 4.6 where training is done on the first ten cycles of an asymmetric strain controlled simulation with $E_{\max} = 1.0\%$ and $R_E = 0.0$. In the online phase, twenty reduced cyclic simulations were run, as shown in figure 4.9, between $E_{\max} = 0.2 - 1.0\%$ for one thousand cycles each. The computational cost for running multiple full field simulations would be at least 800 hours each. But in a reduced setting each simulation costs less than 170 hours. More importantly, each reduced simulation needs less than 125 megabytes of memory, and is run using just one processor. The idea being portrayed here is that without neglecting the physics, the deformation behavior resulting from long cyclic simulations can be studied. This is of great importance because the high fidelity approach presented in chapter 2 cost thousands of hours of computational time and the reduction of such a system leads to an accelerated analysis of the physics of deformation.

-	Full field	Reduced
Nodes	1174719	18408
Elements	859848	10299
Computation time	800 h	70 h
Parallel processors	24	1
RAM	221.2 Gbs	125 Mbs

Table 4.2: Finite element mesh details and the resources needed to run one full field and one reduced simulations

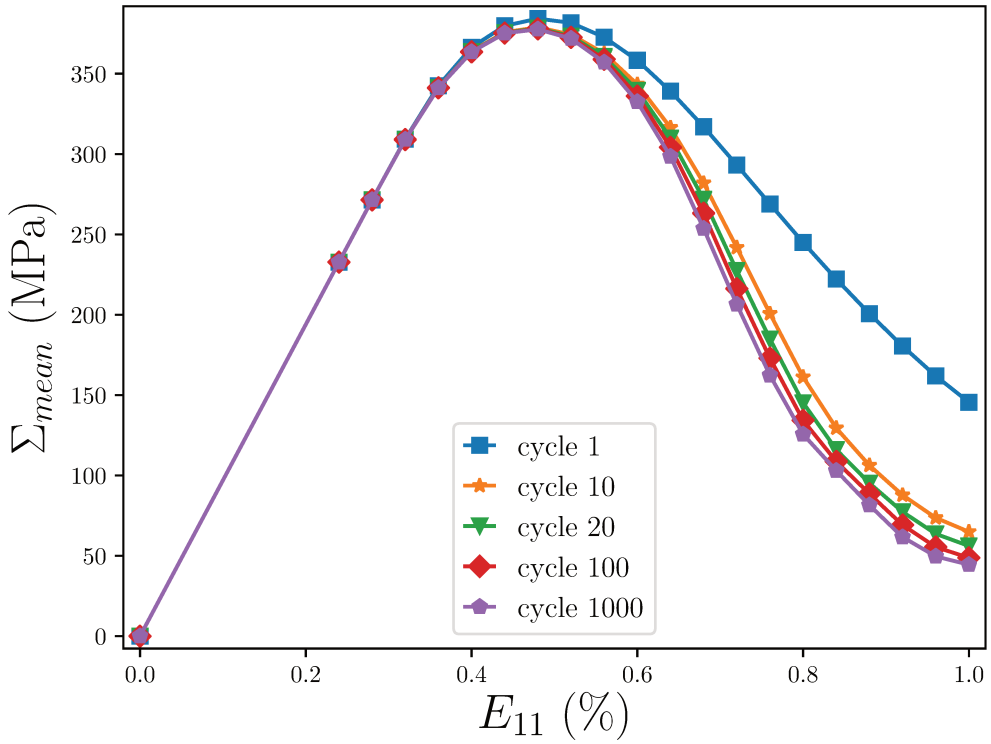

Figure 4.9: Cyclic mean stress vs maximum applied strain using a reduced basis constructed from the offline phase shown in figure 4.6.

4.5 Conclusion

Some cases have been demonstrated showing the capabilities of hyper-reduction for finite element simulations in crystal plasticity. The selection of a suitable parameter space is important to anticipate what can be extracted from a ROM. The conclusion with this regard is that the microstructural parameter space has to be sampled before starting the reduction process, whereas the macroscopic boundary conditions and phenomenological model parameters may serve as a good parameter space. This was demonstrated by testing the given parameter space constituents as well as by giving a practical test for crystal plasticity. It was also demonstrated that adding more information to the RB does not necessarily mean that it will get better. As a future outlook more work may be done in this context by working on the potential improvement of the RB by anticipating which parameter space may be fed to it, to have a large enough information pool for online simulations.

Chapter 5

Conclusion and outlook

5.1 Conclusions

Le premier objectif de cette thèse était de caractériser les charges cycliques non symétriques dans le cas de matériaux métalliques polycristallins. L'approche utilisée était une méthode par éléments finis en prenant en compte la plasticité Cristalline à l'échelle mésoscopique couplée à des éléments de volume représentatifs (VER). En raison de la complexité de la méthode, le deuxième objectif était d'appliquer la réduction de modèle au problème pour accélérer les calculs ainsi que pour explorer l'espace des paramètres pour des simulations de plasticité cristalline de façon extrêmement rapide. Pour atteindre ces objectifs, la thèse a été divisée en plusieurs parties:

- Caractérisation détaillée de simulations cycliques non symétriques selon la méthode CPFE pour les monocristaux et les polycristaux
- Réduction de modèle appliquée au problème cyclique CPFE
- Caractérisation de l'espace des paramètres utilisable pour la réduction de modèle

La première partie a commencé par la prise de deux agrégats polycristallins avec des grains équiaxes et une distribution d'orientation cristallographique isotrope aléatoire.

Cela a été fait dans le but d'étudier les effets locaux fondamentaux qui produisent différents phénomènes macroscopiques. On ne souhaitait pas s'en tenir à une microstructure matérielle spécifique; bien que les ensembles de paramètres de plasticité cristalline aient été établis à proximité de deux matériaux techniques : Inconel 718 et cuivre. Ensuite, on a commencé par observer la réponse mécanique cyclique saturée d'un monocristal. Il a été noté que pour les monocristaux, des régimes discrets de plasticité cyclique ont été observés aussi bien pour les contraintes asymétriques que pour les déformations asymétriques. Dans l'étape suivante, une transition vers un polycristal représentatif a montré que les régimes macroscopiques distincts observés dans les monocristaux disparaissent et des réponses macroscopiques lisses ont été obtenues. Ceci a également conduit à la caractérisation de différents régimes qui sont typiquement observés dans les expériences de cliquetis de souche. Pour résoudre le problème de la caractérisation du cliquettage de déformation, on a mis au point un test comparatif en série qui permet de discriminer le shakedown mécanique du cliquetis. Pour les simulations de relaxation des contraintes moyennes, le polycristal a montré une diminution en douceur de la contrainte moyenne saturée avec une augmentation de la déformation appliquée. Ces résultats sont importants car ils montrent que sans changer les lois constitutives, les résultats expérimentaux peuvent être reproduits à l'aide du CPFEM, à l'échelle macroscopique.

Les résultats obtenus sur un point de Gauss ont ensuite été analysés et deux résultats majeurs ont été élaborés, à savoir la bimodalité de la contrainte et la bimodalité de la contrainte plastique accumulée. On a observé que la contrainte à l'intérieur d'un agrégat polycristallin se divisait progressivement en deux parties avec une augmentation du nombre de cycles simulés ; et ces deux parties concernaient les grains durs et mous. On a émis l'hypothèse que, dans des conditions de charge cyclique, les contraintes migrent des grains durs vers les grains mous, où les grains durs et mous sont caractérisés par leur facteur de Schmid axial total. On a constaté que les déformations plastiques accumulées n'étaient bimodales que dans certaines conditions mécaniques et que cela ne se produisait que lorsque le polycristal subissait un choc plastique ou qu'il avait conservé une contrainte moyenne cyclique. Ces constatations supposaient que dans des conditions asymétriques de contrainte ou de charge de traction, une microstructure se divise en deux parties: une partie qui prend en charge toute la plasticité et l'autre qui stagne, c'est-à-dire arrête l'accumulation de la plasticité.

Le coût de calcul de ces simulations était également très élevé, c'est-à-dire que des téraoctets de données étaient produits chaque semaine, et chaque simulation coûtait 32 gigaoctets de RAM à charger. Pour ce faire, un cluster dédié "Cristal"

a été mis en place pour exécuter ces simulations qui comportaient 18 nœuds avec 256 gigaoctets de RAM et 24 unités de traitement par nœud. Les données issues de ces calculs seront également bientôt disponibles gratuitement sur un serveur dédié.

L'objectif de la deuxième partie de la thèse était de réduire l'ordre du modèle de plasticité cristalline à l'aide d'une approche Gappy POD, puis d'effectuer des simulations cycliques sur le modèle réduit. Le premier problème rencontré dans cette partie est que les simulations par cliquet de déformation ont une très faible tolérance d'erreur et que celle-ci peut être réduite en ajoutant une fonction de correction par éléments finis dans l'estimation. Ceci a été illustré par l'exécution de simulations d'écrouissage de déformation sur un granulat de mille grains, puis la comparaison du résultat de la commande réduite à l'aide de la méthode HROM conventionnelle et de la méthode hybride. Néanmoins, l'approximation hybride s'est avérée meilleure tant au niveau macroscopique qu'au niveau local. Une observation importante dans les simulations d'ordre réduit est que, tout en utilisant la plasticité cristalline, il est beaucoup plus facile d'estimer les contraintes que de prédire les déformations parce que les déformations se localisent.

Après avoir démontré la supériorité de l'approche hyperréduction hybride, l'espace de paramètres a été caractérisé. Il a été démontré que les caractéristiques microstructurales telles que les distributions d'orientation ou la géométrie ne peuvent être réduites dans la procédure actuelle de réduction de l'ordre des modèles. D'autre part, une bonne conformité a été constatée tout en variant les paramètres constitutifs de l'équation. Ceci est d'une grande importance car il est nécessaire de tester différents paramètres de plasticité cristalline pour établir une première estimation des propriétés des matériaux. Il a également été démontré que les paramètres des conditions limites peuvent être modifiés une fois qu'une base réduite a été construite.

5.2 Conclusion

The first objective of this thesis was to characterize non-symmetric cyclic loadings in polycrystalline metallic materials. The approach used was a mesoscale scale crystal plasticity finite element method coupled with representative volume elements. Due to the complexity of the method, the second objective was to apply model order reduction techniques to the problem in the anticipation to accelerate as well as explore the parameter space in crystal plasticity simulations. To achieve

these objectives the thesis was divided into the following parts:

1. Detailed characterization of non-symmetric cyclic simulations using the CPFE method for single as well as polycrystals.
2. Model order reduction applied to the cyclic CPFE problem.
3. Characterization of the parameter space associated to the employed model order reduction technique.

The first part began by taking two polycrystal aggregates with equiaxed grains and a random isotropic crystallographic orientation distribution. This was done because the intention was to study the fundamental local effects which produce different macroscopic phenomena, and not to stick to a particular material microstructure; although, the crystal plasticity parameter sets were set close to two engineering materials: Inconel 718 and copper. Then a start was taken by observing the saturated cyclic mechanical response of a single crystal. It was noted that for single crystals, discrete regimes of cyclic plasticity were observed for both asymmetric stress as well as asymmetric strain. In the next step, a transition to a representative polycrystal showed that the distinct macroscopic regimes observed in single crystals disappear and smooth macroscopic responses were obtained. This also led to the characterization of different regimes which are typically observed in strain ratcheting experiments. To cater for the problem of characterizing strain ratcheting, a series comparison test was devised which discriminated mechanical shakedown from ratcheting. For mean stress relaxation simulations the polycrystal showed a smooth decrease in the saturated mean stress with an increase in the applied strain. These findings are important because they show that without changing the constitutive laws, experimental findings can be reproduced using CPFEM, at the macroscopic scale.

Gauss point results were then analyzed where two major findings were elaborated i.e. the bimodality of stress and the bimodality of accumulated plastic strain. The stress inside a polycrystal aggregate was observed to progressively split into two parts with an increase in the number of simulated cycles; and these two parts pertained to hard and soft grains. This hypothesized that under cyclic loading conditions stresses migrate from hard to soft grains where hard and soft grains were characterized by their total axial Schmid factors. Accumulated plastic strains were seen to be only bimodal under certain mechanical conditions and it was observed that this happened only when the polycrystal experiences plastic shakedown or has retained a cyclic mean stress. These findings hypothesized that under asymmetric

stress or strain loading conditions, a microstructure splits into two parts; one part which takes over all the plasticity and the other which stagnates i.e. stops accumulating plasticity.

The computational cost of these simulations was also very high i.e. terabytes of data was produced on a weekly basis, and each simulation cost 32 gigabytes of RAM to load. To cater for this, a dedicated cluster "Cristal" was set up to run these simulations which had 18 nodes with 256 gigabytes of RAM and 24 processing units per node. Data from these computations will also be freely available soon on a dedicated server.

The objective of the second part of the thesis was to reduce the order of the crystal plasticity model using a gappy POD approach and then to run cyclic simulations on the reduced setting. The first problem encountered in this part was that strain ratcheting simulations have a very low error tolerance and this can be lowered by adding a finite element correction function in the estimation. This was portrayed by running strain ratcheting simulations on a thousand grain aggregate and then comparing the reduced order result using the conventional HROM as well as the hybrid approach. Nevertheless, the hybrid approximation came out to be better both at the macrosopic as well as the local level. One important observation in the reduced order simulations was that while using crystal plasticity estimating stresses is much easier as compared to predicting strains because strains localize.

After demonstrating the superiority of the hybrid hyper-reduction approach, the parameter space was characterized. It was shown that microstructural features such as orientation distributions or the geometry cannot be reduced in the current model order reduction procedure. On the other hand, good conformity was seen while varying the constitutive equation parameters. This is of great importance because testing different crystal plasticity parameters is necessary to establish a first estimate of the properties of materials. It was also shown that the boundary condition parameters can be changed once a RB has been constructed. This also carries significance, as shown by a practical example in figure 4.9 where a RB is constructed using just one simulation and then a large number of results are recovered using the hyper-reduction technique. This merge of model order reduction with large scale crystal plasticity simulations is extremely beneficial in assessing the response of huge aggregates and designing new materials for a better world.

5.3 Perspectives

Dans un premier temps, cette thèse a présenté certains aspects de la physique de la déformation dans les polycristaux chargés cycliquement et dans un second temps, un couplage de simulations par éléments finis avec des techniques de réduction de modèles a été élaboré. Certaines orientations, telles que proposées ci-dessous, peuvent être suivies pour les travaux futurs.

Pour la partie physique, les stratégies suivantes sont proposées :

- Dans la présente étude, le modèle de plasticité cristalline n'a eu qu'une contribution de durcissement cinématique qui a ignoré l'effet de la matrice d'interaction sur la relaxation des contraintes moyennes ainsi que le phénomène de rochet. L'intégration de ces données dans de nouvelles études peut permettre d'élaborer les effets de l'interaction entre les systèmes de glissement et la façon dont ils affectent la réponse macroscopique dans les structures chargées cycliquement.
- On a également supposé que la texture cristallographique était distribuée aléatoirement. Il est également nécessaire de comprendre comment le phénomène de rochet évolue dans les agrégats à forte texture cristallographique ou pour les matériaux multiphasiques à inclusions et vides.
- Des études expérimentales à l'échelle locale peuvent être effectuées pour valider les résultats de la simulation, mais à cette fin, il est difficile de reproduire des champs pour des variables telles que la déformation plastique cumulée. Néanmoins, pour la relaxation des contraintes moyennes, il est possible de mesurer le champ des contraintes locales au moyen d'expériences synchrotron afin de comprendre les phénomènes locaux.
- Les techniques d'apprentissage automatique pour corréler les tendances des données peuvent être utilisées pour stimuler l'évolution non linéaire de la plasticité tout en calculant des centaines de cycles.
- Il est également possible d'étudier des voies de chargement multiaxiales et complexes, ce qui est généralement le cas en pratique.

En ce qui concerne la réduction de modèle, les recherches futures suivantes sont proposées :

- La base réduite peut être enrichie pour incorporer différentes conditions aux limites multiaxiales.
- La méthode d'analyse par composante principale linéaire actuellement utilisée peut être remplacée par l'analyse par composante principale du noyau pour développer des relations non linéaires dans la base réduite.
- Dans la présente formulation, la base réduite utilisée pour les estimations ne tient compte que des champs de déplacement. Cette base réduite peut également être enrichie par l'ajout d'autres variables constitutives.
- Des estimateurs d'erreurs robustes peuvent être formulés dans le contexte de la plasticité cristalline.
- Une extension peut être faite pour modéliser les fissures et les vides dans les matériaux polycristallins.

Ici ont été présentés quelques points qui pourraient être développés dans des études futures, mais de multiples autres directions peuvent également être prises pour comprendre la physique de la déformation des matériaux ainsi que pour développer les techniques de réduction de modèle.

5.4 Outlook

In the frst phase, the thesis presented some aspects of the physics of deformation in cyclically loaded polycrystals and in the second phase a coupling of finite element simulations with model order reduction techniques was elaborated. Some directions, as proposed below, can be followed for future works.

For the physics part the following strategies are proposed:

- In the current study, the crystal plasticity model only had a contribution of kinematic hardening which ignored the effect of the hardening matrix on mean stress relaxation as well as ratcheting. Incorporating this in new studies can elaborate the effects of the interaction between slip systems and how they affect the macroscopic response in cyclically loaded structures.

- It was also assumed that the crystallographic texture was randomly distributed. Understanding how ratcheting evolves in aggregates with strong crystallographic texture or for multiphase materials with inclusions and voids is also necessary.
- Experimental investigations at the local scale can be done to validate the simulation results but to this end it is difficult to reproduce fields for variables such as the accumulated plastic strain. Nevertheless, for mean stress relaxation, local stress field measurements through synchrotron experiments can be done to understand local phenomena.
- Machine learning techniques to correlate data trends can be used for the estimation of nonlinear evolution of plasticity while computing hundreds of cycles.
- Multiaxial and complex loading paths can also be studied which are usually the case in a practical engineering environment

With regards to model order reduction the following future research is proposed:

- The RB can be enriched to incorporate different multiaxial boundary conditions.
- The linear PCA method currently being used can be substituted by kernel PCA to develop nonlinear relationships in the RB.
- In the present formulation, the RB used for the estimations incorporates only displacement fields. This RB may also be enriched by adding data from plastic strains or other constitutive equation variables.
- Robust error estimators can be formulated in the context of crystal plasticity.
- An extension can be done to model cracks and voids in polycrystalline materials.

Multiple other directions can also be taken to understand the physics of material deformation as well as develop the model order reduction technique, but this was just a set of few points which could be elaborated in future studies

Appendix A

Ongoing work

The current ongoing work deals with multiaxial boundary conditions, which is to a large extent, an understudied topic especially using micromechanical techniques. This is one of the requirements of the industry because in-service engineering components are more often subjected to varying types of boundary conditions which combine both stress and strain at the same time. A type of scenario, as presented in A.1 pertains to stress controlled loadings where different combinations of traction and shear are postulated. The problem is portrayed in figure A.1 (a) where three different boundary conditions are applied as follows[1]:

- Traction and shear: a traction of 900 MPa is applied on Σ_{11} which is followed by a shear of 200 MPa on component Σ_{12} (blue curve)
- Shear and traction: a shear of 200 MPa is applied on Σ_{12} and then a traction of 900 MPa in Σ_{11} (red curve)
- Shear and traction together: Both Σ_{12} (200 MPa) and Σ_{11} (900 MPa) are applied together (black curve)

Marked by a gray cross in figure A.1 (a) the final macroscopic stress state is the same in all three cases but the difference lies only in the path taken. Figures A.1 (b) and (c) show the macroscopic axial strain and the accumulated plastic strain for all three scenarios. It can be seen that when first traction and then shear is

[1] As a test case VE 1 with parameter set LK was used.

applied, the resulting accumulated plastic strain is higher than the other two cases. Also, the von Mises stress and von Mises strain curves can be seen in figure A.1 (d), where the traction and shear case has more von Mises strain associated to it.

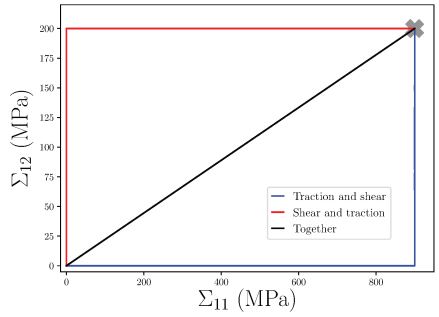

(a) Prescribed boundary conditions

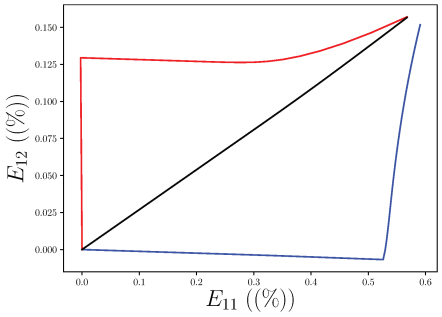

(b) Macroscopic axial strains

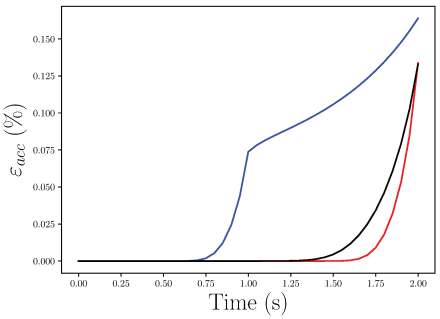

(c) Accumulated plastic strain

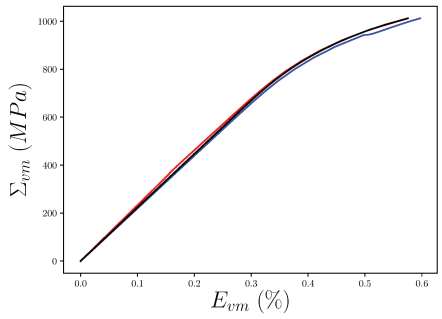

(d) Von Mises stress vs von Mises strain

Figure A.1: Mechanical response of the three scenarios with different combinations of traction and shear boundary conditions. Parameter set LK and VE 1 was used for this test.

The second example shown here pertains to 2-dimensional stress and strain boundary conditions which lead to 1-dimensional strain ratcheting. The applied boundary conditions are presented in figure A.2 (a) and (b) where first a constant axial stress $\Sigma_{11} = 200$ MPa is applied and held constant throughout the test, after which a cyclic shear of $E_{23} = \pm 0.6\%$ is applied. These 2-dimensional boundary conditions lead to a ratcheting strain in direction E_{11} as shown in figure A.2 (c). Similarly, figure A.3 shows the local distribution of the von Mises strain, von Mises stress, and the accumulated plastic strain. Detailed analysis are needed both at the local and macroscopic level to characterize such multiaxial responses and this is one of the research directions currently being pursued.

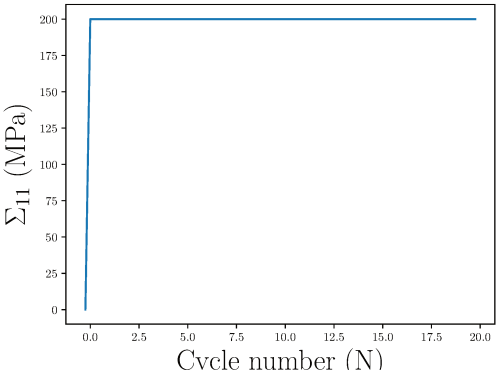

(a) Applied stress Σ_{11}

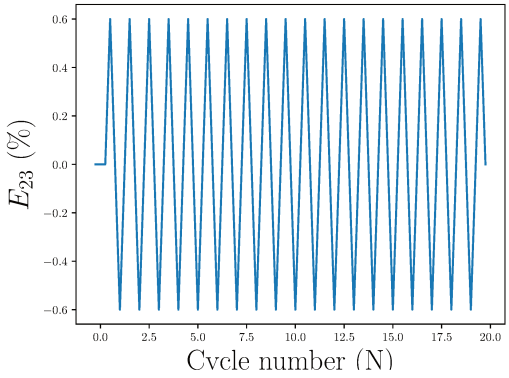

(b) Applied shear strain E_{23}

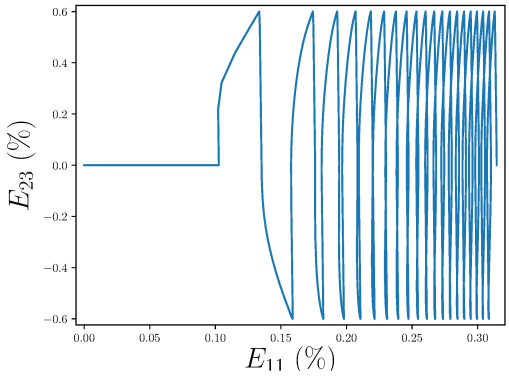

(c) Axial ratcheting in direction E_{11}

Figure A.2: Axial ratcheting response (E_{11}) by applying multiaxial stress and shear boundary conditions. Parameter set LK and VE 1 was used for this test.

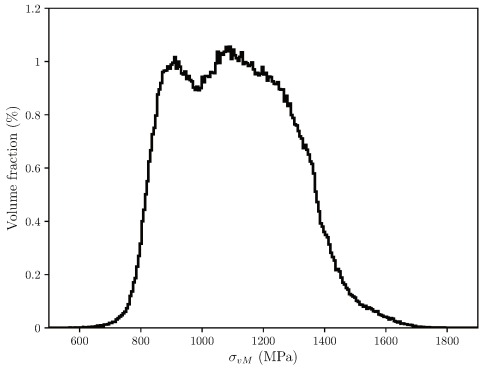

(a) Local von Mises stress (σ_{vM})

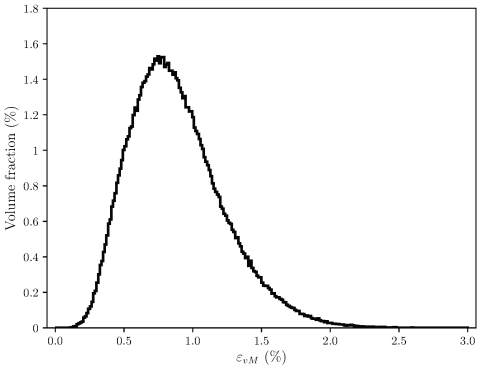

(b) Local von Mises strain (ε_{vM})

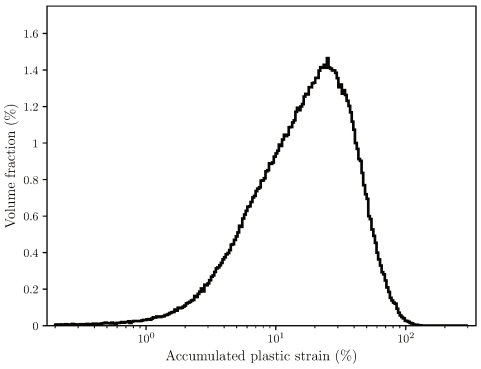

(c) Local accumulated plastic strain

Figure A.3: Local distribution curves for the multiaxial ratcheting simulation. All results were extracted at the tensile peak of the twentieth cycle. Parameter set LK and VE 1 was used for this test.

Appendix B

Analysis of mesh sensitivity

Selecting the appropriate mesh density for finite element polycrystal simulations is not straightforward. A start can be taken by refining the mesh until a converged macroscopic tensile curve is obtained but finding macroscopic properties is not the only goal of the work. If macroscopic properties were the main goal, then macroscopic models could have been used or even mean field models which take into account a lot of local information and are much faster to perform as well as require considerably less computational resources. The goal here is also to assess local responses inside the grains. This requires large number of DOFs in each grain. Also there is considerable difference in the solutions obtained using different boundary conditions. In this article two types of boundary conditions are used: Periodic strain control or periodic stress control. Periodic stress boundary conditions are anticipated to produce more convergence issues as compared to periodic strain because in metal plasticity, a small increment in stress produces a large increment in strain. This effect is even more pronounced at the local level because of severe heterogeneity in crystal plasticity simulations. With regards to VE 1 which contains 300 grains, three mesh densities were tested for this chapter:

1. coarse mesh with 112565 nodes and 74270 quadratic elements
2. mesh in use with 194903 nodes and 130171 quadratic elements
3. fine mesh with 270670 nodes and 181905 quadratic elements

This appendix sheds light on the choice of mesh density in Chapter 2

A tensile test on these meshes was performed and three responses were compared i.e. the macroscopic averaged stress strain response, the von Mises equivalent stress and strain at each Gauss point at the maximum traction/displacement. For periodic strain control a 2% macroscopic strain was imposed while for periodic stress a macroscopic stress of 1110 MPa was imposed in the tensile direction. Figures B.1 and B.2 show the three responses for both loading conditions. For strain controlled loading, all three meshes provide a somewhat converged solution, both at the macroscopic level and at the local level. Apart from some mismatch in the local von Mises stress distribution curve there even the coarse mesh seems to do the job. This is not the case for stress based loading conditions. At the macroscopic scale, the three meshes do not lead to the same value of the mean strain at the final loading point, see Fig. B.2(a). The largest discrepancies are found for the equivalent stress distribution, Fig. B.2(b). This shows that load controlled asymmetric simulations require a very fine mesh to obtain converged local strain distributions. Also, even if there is a small error in the applied stress at each increment, it can result in a significant error in the calculated strains. Using 24 parallel cores for each job, the time needed to run one tensile load controlled test on each mesh was 10, 33 and 60 hours respectively. Although differences can be observed in the load controlled simulation, hundreds of tests were required for this study and hence the intermediate mesh size with 130171 elements was selected.

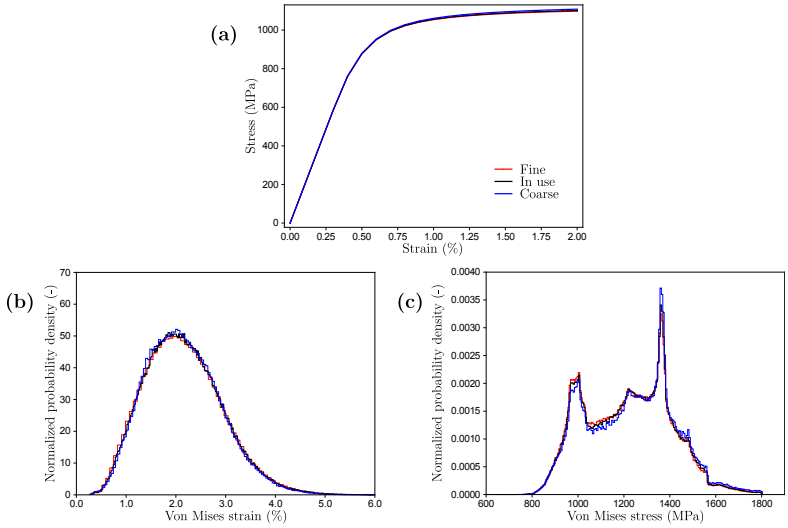

Figure B.1: Using parameter set LK, tensile test simulations for three finite element meshes under a macroscopic periodic strain of 2%: (a) macroscopic averaged stress strain plot,(b) and (c) von Mises equivalent strain and stress distributions at the peak macroscopic strain.

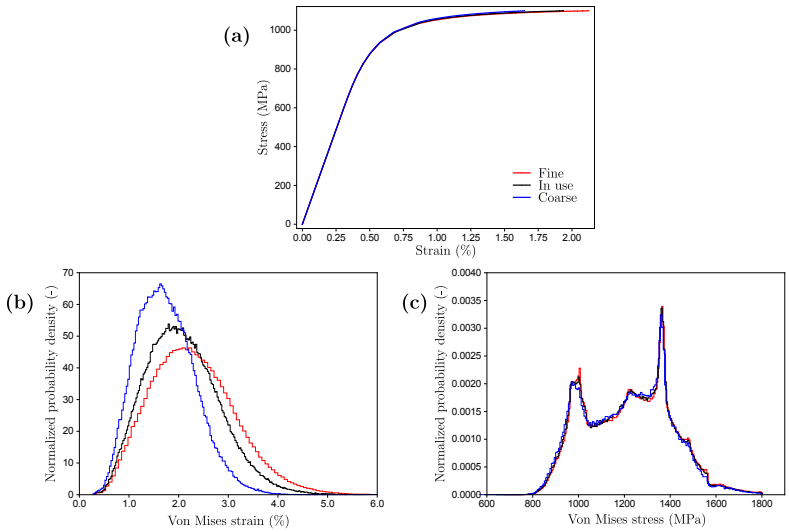

Figure B.2: Using parameter set LK, tensile test simulations for three finite element meshes under a macroscopic periodic load of 1100 MPa: (a) macroscopic averaged stress strain plot, (b) and (c) show the von Mises equivalent strain and stress at the peak macroscopic stress.

Appendix C

Grain size distribution

This appendix shows the investigation of grain sizes and shapes for a polycrystal with an isotropic crystallographic texture distribution. Figure C.1 shows three different polycrystal geometries, each having 1000 grains. The difference lies in their grain size distribution as well as finite element mesh. The three geometries contain:

- Cubic grains with identical sizes and a hexahedral mesh
- Voronoi tessellated geometry with a tetrahedral mesh
- A different Voronoi tessellated geometry with a tetrahedral mesh

The grain size of the cubic geometry was constant i.e. 10 μm while the grain size distribution for the other two geometries is shown in figure C.2.

The three geometries were subjected to a 2% macroscopic strain and the corresponding mechanical responses may be viewed in figure C.3. All three geometries regardless of their grain size distribution or finite element mesh type show very similar macroscopic as well as local responses. One plus for using an irregular mesh as compared to brick elements is the ease with which grain boundaries can be represented i.e. with regular elements, a staircase type of grain boundary emerges rather than a smooth layer.

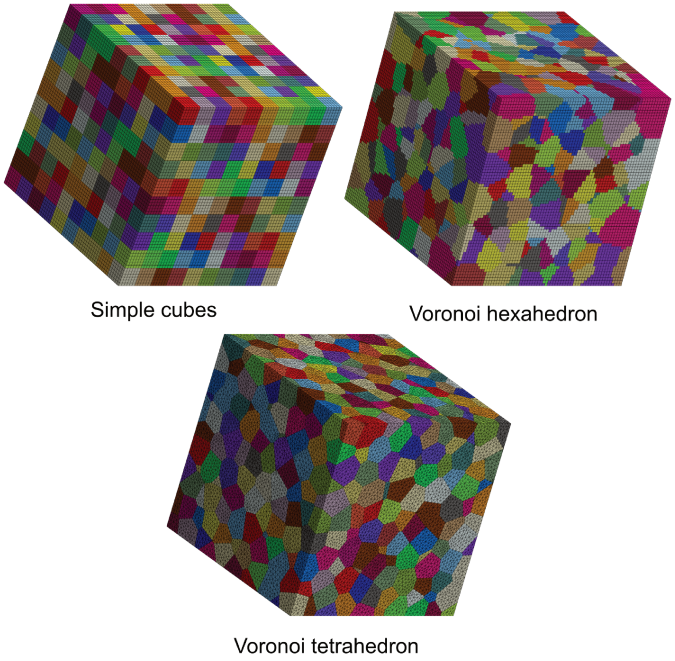

Figure C.1: The three geometries used to test mechanical properties i.e. a simple cubic geometry with a hexahedral mesh, Voronoi with a hexahedral mesh, and a Voronoi geometry with a tetrahedral mesh. All geometries contain 1000 grains.

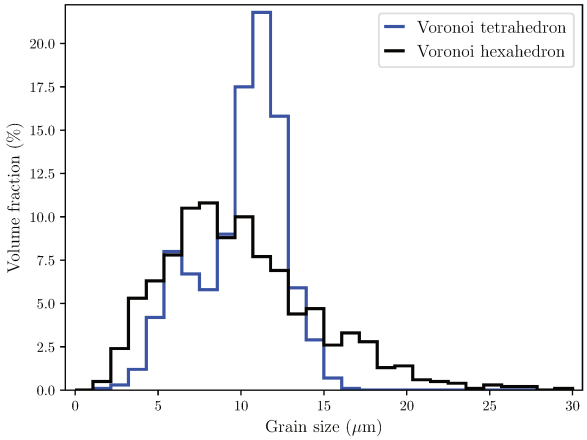

Figure C.2: Grain size distribution for the geometries with Voronoi meshes

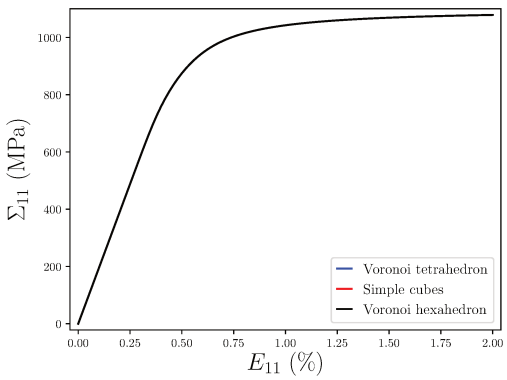

Macroscopic stress strain response

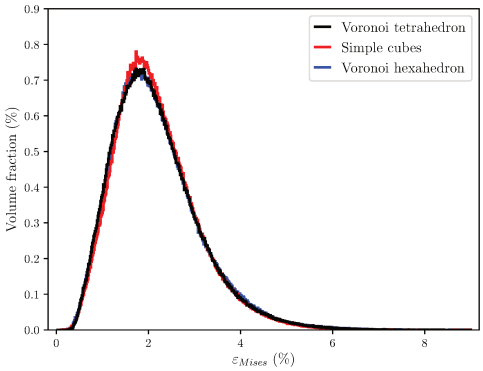

Von Mises strain distribution

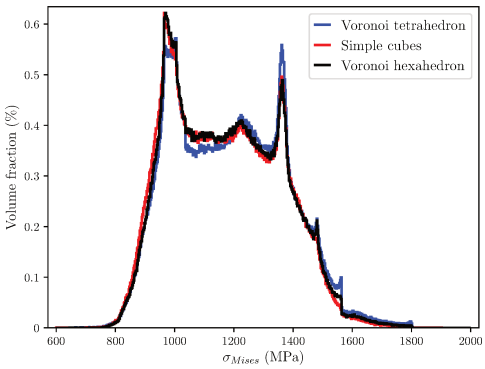

Von Mises stress distribution

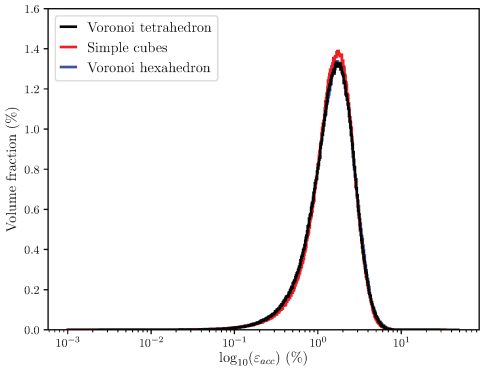

Accumulated plastic strain distribution

Figure C.3: Mechanical response of the three geometries strained up to 2%. The Gauss point distributions are extracted at the peak applied strain.

Bibliography

Abuzaid, W. Z., Sangid, M. D., Carroll, J. D., Sehitoglu, H., Lambros, J., 2012. Slip transfer and plastic strain accumulation across grain boundaries in Hastelloy X. Journal of the Mechanics and Physics of Solids 60 (6), 1201 – 1220.

Akkari, N., Hamdouni, A., Liberge, E., Jazar, M., 2014. On the sensitivity of the POD technique for a parameterized quasi-nonlinear parabolic equation. Advanced Modeling and Simulation in Engineering Sciences 1 (1), 14.

Almroth, B., Stehling, P., Brogan, F., 1981. Global function approach in structural analysis: Basic approach, numerical results.

Almroth, B., Stern, P., Brogan, F. A., 1978a. Automatic choice of global shape functions in structural analysis. Aiaa Journal 16 (5), 525–528.

Almroth, B. O., Stern, P., Brogan, F. A., 1978b. Automatic choice of global shape functions in structural analysis. AIAA Journal 16 (5), 525–528.

Arcari, A., Vita, R. D., Dowling, N. E., 2009. Mean stress relaxation during cyclic straining of high strength aluminum alloys. International Journal of Fatigue 31 (11), 1742 – 1750.

Arsenlis, A., Parks, D., 1999. Crystallographic aspects of geometrically-necessary and statistically–stored dislocation density. Acta materialia 47 (5), 1597–1611.

Arsenlis, A., Parks, D. M., Becker, R., Bulatov, V. V., 2004. On the evolution of crystallographic dislocation density in non–homogeneously deforming crystals. Journal of the Mechanics and Physics of Solids 52 (6), 1213–1246.

Asaro, R., Rice, J., 1977. Strain localization in ductile single crystals. Journal of the Mechanics and Physics of Solids 25 (5), 309 – 338.

Aubry, N., Holmes, P., Lumley, J. L., Stone, E., 1988. The dynamics of coherent structures in the wall region of a turbulent boundary layer. Journal of Fluid Mechanics 192, 115–173.

Azzouz, F., Cailletaud, G., Chaboche, J. L., Ostoja-Kuczynski, E., Quilici, S., 2010. Cyclic calculations and life estimation in thermomechanical fatigue. In: 9th International conference on multiaxial fatigue and fracture. pp. 785–793.

Baiges, J., Codina, R., Idelsohn, S., 2013. A domain decomposition strategy for reduced order models. application to the incompressible Navier–Stokes equations. Computer Methods in Applied Mechanics and Engineering 267, 23 – 42.

Barbe, F., Forest, S., Cailletaud, G., 2001. Intergranular and intragranular behavior of polycrystalline aggregates. Part 2: Results. International Journal of Plasticity 17 (4), 537 – 563.

Barrault, M., Maday, Y., Nguyen, N. C., Patera, A. T., 2004. An 'empirical interpolation' method: application to efficient reduced-basis discretization of partial differential equations. Comptes Rendus Mathematique 339 (9), 667–672.

Becker, R., Butler, J., Hu, H., Lalli, L., 1991. Analysis of an aluminum single crystal with unstable initial orientation (001)[110] in channel die compression. Metallurgical Transactions A 22 (1), 45–58.

Bennett, V., McDowell, D., 2003. Polycrystal orientation distribution effects on microslip in high cycle fatigue. International Journal of Fatigue 25 (1), 27 – 39.

Besson, J., Cailletaud, G., Chaboche, J.-L., Forest, S., 2009. Non-linear mechanics of materials. Vol. 167. Springer Science & Business Media.

Bieler, T., Eisenlohr, P., Roters, F., Kumar, D., Mason, D., Crimp, M., Raabe, D., 2009. The role of heterogeneous deformation on damage nucleation at grain boundaries in single phase metals. International Journal of Plasticity 25 (9), 1655–1683.

Brand, M., 2002. Incremental singular value decomposition of uncertain data with missing values. In: European Conference on Computer Vision. Springer, pp. 707–720.

Buljak, V., 2012. Proper Orthogonal Decomposition and Radial Basis Functions for Fast Simulations. Springer Berlin Heidelberg, Berlin, Heidelberg, pp. 85–139.

Bull, J. W., 2012. Numerical analysis and modelling of composite materials. Springer Science & Business Media.

Busso, E. P., Cailletaud, G., 2005. On the selection of active slip systems in crystal plasticity. International Journal of Plasticity 21 (11), 2212 – 2231, plasticity of Heterogeneous Materials.

Cailletaud, G., et al., 1991. Single crystal modeling for structural calculations: Part 2 – finite element implementation. Journal of Engineering Materials and Technology 113 (1), 171–182.

Castelluccio, G. M., Musinski, W. D., McDowell, D. L., 2016. Computational micromechanics of fatigue of microstructures in the hcf–vhcf regimes. International Journal of Fatigue 93, 387 – 396, gigacycle Fatigue-Theory and Applications Dedicated to the Memory of Professor Claude Bathias.

Chaboche, J., 1986. Time-independent constitutive theories for cyclic plasticity. International Journal of Plasticity 2 (2), 149 – 188.

Chaboche, J., 1989. Constitutive equations for cyclic plasticity and cyclic viscoplasticity. International Journal of Plasticity 5 (3), 247 – 302.

Chaboche, J.-L., Kanouté, P., Azzouz, F., 2012. Cyclic inelastic constitutive equations and their impact on the fatigue life predictions. International Journal of Plasticity 35, 44 – 66.

Chaturantabut, S., Sorensen, D., 2010. Nonlinear model reduction via Discrete Empirical Interpolation. SIAM Journal on Scientific Computing 32 (5), 2737–2764.

Choi, Y., Groeber, M., Turner, T., Dimiduk, D., Woodward, C., Uchic, M., Parthasarathy, T., 2012. A crystal-plasticity FEM study on effects of simplified grain representation and mesh types on mesoscopic plasticity heterogeneities. Materials Science and Engineering: A 553, 37 – 44.

Christ, H.-J., Wamukwamba, C., Mughrabi, H., 1997. The effect of mean stress on the high-temperature fatigue behaviour of SAE 1045 steel. Materials Science and Engineering: A 234-236, 382 – 385.

Clark, W., Wagoner, R., Shen, Z., Lee, T., Robertson, I., Birnbaum, H., 1992. On the criteria for slip transmission across interfaces in polycrystals. Scripta Metallurgica et Materialia 26 (2), 203–206.

Colas, D., Finot, E., Flouriot, S., Forest, S., Mazière, M., Paris, T., 2019. Local ratcheting phenomena in the cyclic behavior of polycrystalline tantalum. JOM 71 (8), 2586–2599.

Cruzado, A., LLorca, J., Segurado, J., 2017. Modeling cyclic deformation of Inconel 718 superalloy by means of crystal plasticity and computational homogenization. International Journal of Solids and Structures 122-123 (Supplement C), 148 – 161.

Cruzado, A., Urchegui, M., Gómez, X., 2012. Finite element modeling and experimental validation of fretting wear scars in thin steel wires. Wear 289, 26–38.

Das, D., Chakraborti, P., 2011. Effect of stress parameters on ratcheting deformation stages of polycrystalline OFHC copper. Fatigue & Fracture of Engineering Materials & Structures 34 (9), 734–742.

Di Gioacchino, F., Quinta da Fonseca, J., 2013. Plastic strain mapping with sub-micron resolution using digital image correlation. Experimental Mechanics 53 (5), 743–754.

Dingreville, R., Battaile, C. C., Brewer, L. N., Holm, E. A., Boyce, B. L., 2010. The effect of microstructural representation on simulations of microplastic ratcheting. International Journal of Plasticity 26 (5), 617 – 633.

Dunne, F., Rugg, D., Walker, A., 2007a. Lengthscale-dependent, elastically anisotropic, physically-based hcp crystal plasticity: application to cold-dwell fatigue in ti alloys. International Journal of Plasticity 23 (6), 1061–1083.

Dunne, F., Wilkinson, A., Allen, R., 2007b. Experimental and computational studies of low cycle fatigue crack nucleation in a polycrystal. International Journal of Plasticity 23 (2), 273 – 295.

Edmonds, J., 1971. Matroids and the greedy algorithm. Mathematical programming 1 (1), 127–136.

Everson, R., Sirovich, L., 1995. Karhunen–loeve procedure for gappy data. JOSA A 12 (8), 1657–1664.

Flipon, B., Keller, C., Quey, R., Barbe, F., 2019. A full-field crystal-plasticity analysis of bimodal polycrystals. International Journal of Solids and Structures, in press.

Forest, S., Rubin, M., 2016. A rate-independent crystal plasticity model with a smooth elastic–plastic transition and no slip indeterminacy. European Journal of Mechanics - A/Solids 55, 278 – 288.

Fournier, D., Pineau, A., 1977. Low cycle fatigue behavior of Inconel 718 at 298 K and 823 K. Metallurgical Transactions A 8 (7), 1095–1105.

Frederick, C., Armstrong, P., 2007. A mathematical representation of the multiaxial Bauschinger effect. Materials at High Temperatures 24 (1), 1–26.

Fritzen, F., Hassani, M., Apr 2018. Space–time model order reduction for nonlinear viscoelastic systems subjected to long-term loading. Meccanica 53 (6), 1333–1355.

Gérard, C., Cailletaud, G., Bacroix, B., 2013. Modeling of latent hardening produced by complex loading paths in FCC alloys. International Journal of Plasticity 42, 194 – 212.

Ghorbanpour, S., Zecevic, M., Kumar, A., Jahedi, M., Bicknell, J., Jorgensen, L., Beyerlein, I. J., Knezevic, M., 2017. A crystal plasticity model incorporating the effects of precipitates in superalloys: Application to tensile, compressive, and cyclic deformation of Inconel 718. International Journal of Plasticity 99, 162 – 185.

Goh, C.-H., McDowell, D., Neu, R., 2006. Plasticity in polycrystalline fretting fatigue contacts. Journal of the Mechanics and Physics of Solids 54 (2), 340 – 367.

Goh, C.-H., Wallace, J., Neu, R., McDowell, D., 2001. Polycrystal plasticity simulations of fretting fatigue. International Journal of Fatigue 23, 423 – 435.

Goodman, A., 1984. Development of constitutive equations for computer analysis of stainless steel components. Nuclear engineering and design 83 (3), 349–354.

Gribbin, S., Bicknell, J., Jorgensen, L., Tsukrov, I., Knezevic, M., 2016. Low cycle fatigue behavior of direct metal laser sintered Inconel alloy 718. International Journal of Fatigue 93, 156 – 167.

Gu, T., Medy, J.-R., Klosek, V., Castelnau, O., Forest, S., Herve-Luanco, E., Lecouturier-Dupouy, F., Proudhon, H., Renault, P.-O., Thilly, L., et al., 2019. Multiscale modeling of the elasto–plastic behavior of architectured and nanostructured Cu-Nb composite wires and comparison with neutron diffraction experiments. International Journal of Plasticity.

Guilhem, Y., Basseville, S., Curtit, F., Stéphan, J.-M., Cailletaud, G., mar 2018. Numerical analysis of the effect of surface roughness on mechanical fields in polycrystalline aggregates. Modelling and Simulation in Materials Science and Engineering 26 (4), 045004.

Hao, H., Ye, D., Chen, Y., Feng, M., Liu, J., 2015. A study on the mean stress relaxation behavior of 2124-T851 aluminum alloy during low–cycle fatigue at different strain ratios. Materials & Design 67, 272 – 279.

Harren, S., Deve, H., Asaro, R., 1988. Shear band formation in plane strain compression. Acta Metallurgica 36 (9), 2435–2480.

Hassan, T., Kyriakides, S., 1994a. Ratcheting of cyclically hardening and softening materials: I. Uniaxial behavior. International Journal of Plasticity 10 (2), 149–184.

Hassan, T., Kyriakides, S., 1994b. Ratcheting of cyclically hardening and softening materials: II. Multiaxial behavior. International Journal of Plasticity 10 (2), 185 – 212.

Hennessey, C., Castelluccio, G. M., McDowell, D. L., 2017. Sensitivity of polycrystal plasticity to slip system kinematic hardening laws for Al 7075-T6. Materials Science and Engineering: A 687 (Supplement C), 241 – 248.

Hernàndez, J., Oliver, J., Huespe, A., Caicedo, M., Cante, J., 2014. High–performance model reduction techniques in computational multiscale homogenization. Computer Methods in Applied Mechanics and Engineering 276, 149 – 189.

Jiang, Y., Sehitoglu, H., 1994. Multiaxial cyclic ratcheting under multiple step loading. International Journal of Plasticity 10 (8), 849 – 870.

Joseph, D. S., Chakraborty, P., Ghosh, S., 2010. Wavelet transformation based multi-time scaling method for crystal plasticity FE simulations under cyclic loading. Computer Methods in Applied Mechanics and Engineering 199 (33), 2177 – 2194.

K. Karhunen, K., 1947. Über lineare Methoden in der Wahrscheinlichkeitsrechnung. Ann. Acad. Sci. Fennicae. Ser. A. I. Math.-Phys. (37), 1–79.

Kammers, A. D., Daly, S., 2013. Digital image correlation under scanning electron microscopy: Methodology and validation. Experimental Mechanics 53 (9), 1743–1761.

Kang, G., Dong, Y., Wang, H., Liu, Y., Cheng, X., 2010. Dislocation evolution in 316L stainless steel subjected to uniaxial ratchetting deformation. Materials Science and Engineering: A 527 (21), 5952 – 5961.

Kanit, T., Forest, S., Galliet, I., Mounoury, V., Jeulin, D., 2003. Determination of the size of the representative volume element for random composites: statistical and numerical approach. International Journal of Solids and Structures 40 (13), 3647 – 3679.

Kanit, T., Nguyen, F., Forest, S., Jeulin, D., Reed, M., Singleton, S., 2006. Apparent and effective physical properties of heterogeneous materials: representativity of samples of two materials from food industry. Computer Methods in Applied Mechanics and Engineering 195, 3960–3982.

Karhunen, K., 1946. Zur spektraltheorie stochastischer prozesse. Ann. Acad. Sci. Finnicae, Ser. A 1, 34.

Kotha, S., Ozturk, D., Ghosh, S., 2019. Parametrically homogenized constitutive models (phcms) from micromechanical crystal plasticity fe simulations, part I: Sensitivity analysis and parameter identification for titanium alloys. International Journal of Plasticity 120, 296 – 319.

Kraska, M., Doig, M., Tikhomirov, D., Raabe, D., Roters, F., 2009. Virtual material testing for stamping simulations based on polycrystal plasticity. Computational Materials Science 46 (2), 383–392.

Krishna, S., Hassan, T., Naceur, I. B., Sai, K., Cailletaud, G., 2009. Macro versus micro–scale constitutive models in simulating proportional and nonproportional cyclic and ratcheting responses of stainless steel 304. International Journal of Plasticity 25 (10), 1910 – 1949.

Kwofie, S., Chandler, H., 2001. Low cycle fatigue under tensile mean stresses where cyclic life extension occurs. International Journal of Fatigue 23 (4), 341 – 345.

Lee, S.-B., Lebensohn, R., Rollett, A., 2011. Modeling the viscoplastic micromechanical response of two-phase materials using Fast Fourier Transforms. International Journal of Plasticity 27 (5), 707 – 727.

Lemaitre, J., Chaboche, J.-L., 1994. Mechanics of solid materials. Cambridge university press.

Li, L., Shen, L., Proust, G., 2015. Fatigue crack initiation life prediction for aluminium alloy 7075 using crystal plasticity finite element simulations. Mechanics of Materials 81, 84–93.

Liberge, E., Hamdouni, A., 2010. Reduced order modelling method via proper orthogonal decomposition (POD) for flow around an oscillating cylinder. Journal of Fluids and Structures 26 (2), 292 – 311.

Lim, C.-B., Kim, K., Seong, J., 2009. Ratcheting and fatigue behavior of a copper alloy under uniaxial cyclic loading with mean stress. International Journal of Fatigue 31 (3), 501 – 507.

Loève, M., 1963. Probability Theory. The university series in higher mathematics, NJ, 3rd edition. Van Nosterand, Princeton.

Ma, A., Roters, F., Raabe, D., 2006. On the consideration of interactions between dislocations and grain boundaries in crystal plasticity finite element modeling–theory, experiments, and simulations. Acta Materialia 54 (8), 2181–2194.

Maday, Y., Nguyen, N. C., Patera, A. T., Pau, G. S., 2007. A general, multipurpose interpolation procedure: the magic points.

Maday, Y., Patera, A. T., Turinici, G., 2002. Global a priori convergence theory for reduced-basis approximations of single–parameter symmetric coercive elliptic partial differential equations. Comptes Rendus Mathematique 335 (3), 289–294.

Maday, Y., Rønquist, E. M., 2002. A reduced–basis element method. Journal of scientific computing 17 (1-4), 447–459.

Mary, C., Fouvry, S., 2007. Numerical prediction of fretting contact durability using energy wear approach: Optimisation of finite-element model. Wear 263 (1-6), 444–450.

Matouš, K., Geers, M. G., Kouznetsova, V. G., Gillman, A., 2017. A review of predictive nonlinear theories for multiscale modeling of heterogeneous materials. Journal of Computational Physics 330, 192 – 220.

McDowell, D., Dunne, F., 2010. Microstructure–sensitive computational modeling of fatigue crack formation. International journal of fatigue 32 (9), 1521–1542.

Méric, L., Cailletaud, G., Gaspérini, M., 1994. Fe calculations of copper bicrystal specimens submitted to tension–compression tests. Acta metallurgica et materialia 42 (3), 921–935.

Méric, L., Poubanne, P., Cailletaud, G., 1991. Single crystal modeling for structural calculations: part 1 – model presentation. Journal of Engineering Materials and Technology 113 (1), 162–170.

Michel, J., Suquet, P., 2003. Nonuniform transformation field analysis. International Journal of Solids and Structures 40 (25), 6937 – 6955.

Morgeneyer, T. F., Besson, J., Proudhon, H., Starink, M. J., Sinclair, I., 2009. Experimental and numerical analysis of toughness anisotropy in AA2139 Al-alloy sheet. Acta Materialia 57 (13), 3902 – 3915.

Morrissey, R., Goh, C.-H., McDowell, D. L., 2003. Microstructure-scale modeling of hcf deformation. Mechanics of Materials 35 (3), 295 – 311.

Morrow, J., Martin, J., Dowling, N. E., 1974. Local stress-strain approach to cumulative fatigue damage analysis. Tech. rep., ILLINOIS UNIV AT URBANA DEPT OF THEORETICAL AND APPLIED MECHANICS.

N. Lorenz, E., 01 1956. Empirical Orthogonal Functions and Statistical Weather Prediction. Statistical Forecasting 1.

Nikulin, I., Yoshinaka, F., Sawaguchi, T., 2019. Superior fatigue life of Fe-15Mn-10Cr-8Ni-4Si seismic damping alloy under asymmetric cyclic loading with tensile mean strain. Materials Science and Engineering: A 748, 371 – 378.

Noor, A. K., 1982. On making large nonlinear problems small. Computer methods in applied mechanics and engineering 34 (1-3), 955–985.

Ohno, N., Abdel-Karim, M., Kobayashi, M., Igari, T., 1998. Rattcheting characteristics of 316FR steel at high temperature, part I: Strain-controlled ratchetting experiments and simulations. International Journal of Plasticity 14 (4), 355 – 372.

Ohno, N., Wang, J.-D., 1993. Kinematic hardening rules with critical state of dynamic recovery, part II: application to experiments of ratcheting behavior. International Journal of Plasticity 9, 391–403.

Osipov, N., Gourgues-Lorenzon, A.-F., Marini, B., Mounoury, V., Nguyen, F., Cailletaud, G., 2008. FE modelling of bainitic steels using crystal plasticity. Philosophical magazine 88 (30-32), 3757–3777.

Ozturk, D., Shahba, A., Ghosh, S., 2016. Crystal plasticity fe study of the effect of thermo-mechanical loading on fatigue crack nucleation in titanium alloys. Fatigue & Fracture of Engineering Materials & Structures 39 (6), 752–769.

Pan, S. J., Yang, Q., 2010. A survey on transfer learning. IEEE Transactions on Knowledge and Data Engineering 22 (10), 1345–1359.

Park, S., Kim, K., Kim, H., 2007. Ratcheting behaviour and mean stress considerations in uniaxial low-cycle fatigue of inconel 718 at 649° C. Fatigue & Fracture of Engineering Materials & Structures 30 (11), 1076–1083.

Pearson, K., 1901. LIII. on lines and planes of closest fit to systems of points in space. The London, Edinburgh, and Dublin Philosophical Magazine and Journal of Science 2 (11), 559–572.

Peirce, D., Asaro, R., Needleman, A., 1982. An analysis of nonuniform and localized deformation in ductile single crystals. Acta metallurgica 30 (6), 1087–1119.

Pelle, J.-P., Ryckelynck, D., 2000. An efficient adaptive strategy to master the global quality of viscoplastic analysis. Computers & Structures 78 (1), 169 – 183.

Pellissier-Tanon, A., Bernard, J., Amzallag, C., Rabbe, P., 1982. Evaluation of the resistance of type 316 stainless steel against progressive deformation. In: Low-Cycle Fatigue and Life Prediction. ASTM International.

Portier, L., Calloch, S., Marquis, D., Geyer, P., 2000. Ratchetting under tension–torsion loadings: experiments and modelling. International Journal of Plasticity 16 (3), 303 – 335.

Prithivirajan, V., Sangid, M. D., 2018. The role of defects and critical pore size analysis in the fatigue response of additively manufactured IN718 via crystal plasticity. Materials & Design 150, 139 – 153.

Proudhon, H., Li, J., Wang, F., Roos, A., Chiaruttini, V., Forest, S., 2016. 3d simulation of short fatigue crack propagation by finite element crystal plasticity and remeshing. International Journal of Fatigue 82, 238 – 246.

Prud'Homme, C., Rovas, D. V., Veroy, K., Machiels, L., Maday, Y., Patera, A. T., Turinici, G., 2002. Reliable real-time solution of parametrized partial differential equations: Reduced–basis output bound methods. Journal of Fluids Engineering 124 (1), 70–80.

Raabe, D., 2004. Computational Materials Science – The Simulation of Materials Microstructures and Properties.

Raabe, D., Klose, P., Engl, B., Imlau, K.-P., Friedel, F., Roters, F., 2002. Concepts for integrating plastic anisotropy into metal forming simulations. Advanced Engineering Materials 4 (4), 169–180.

Rao, C., Deshpande, A., 2014. Modelling of Engineering Materials. Ane/Athena Books. Wiley.

Rice, J. R., 1971. Inelastic constitutive relations for solids: An internal–variable theory and its application to metal plasticity. Journal of the Mechanics and Physics of Solids 19 (6), 433 – 455.

Rodgers, J. L., Nicewander, W. A., 1988. Thirteen ways to look at the correlation coefficient. The American Statistician 42(1), 59 – 66.

Roters, F., Eisenlohr, P., Bieler, T. R., Raabe, D., 2011. Crystal plasticity finite element methods: in materials science and engineering. John Wiley & Sons.

Roters, F., Eisenlohr, P., Hantcherli, L., Tjahjanto, D. D., Bieler, T. R., Raabe, D., 2010. Overview of constitutive laws, kinematics, homogenization and multiscale methods in crystal plasticity finite–element modeling: Theory, experiments, applications. Acta Materialia 58 (4), 1152–1211.

Rovinelli, A., Sangid, M. D., Proudhon, H., Ludwig, W., 2018. Using machine learning and a data–driven approach to identify the small fatigue crack driving force in polycrystalline materials. npj Computational Materials 4 (1), 35.

Ryckelynck, D., 2009. Hyper–reduction of mechanical models involving internal variables. International Journal for Numerical Methods in Engineering 77 (1), 75–89.

Ryckelynck, D., Benziane, D. M., Musienko, A., Cailletaud, G., 2010. Toward "green" mechanical simulations in materials science: hyper–reduction of a polycrystal plasticity model. European Journal of Computational Mechanics/Revue Européenne de Mécanique Numérique 19 (4), 365–388.

Ryckelynck, D., Chinesta, F., Cueto, E., Ammar, A., 2006. On the a priori model reduction: Overview and recent developments. Archives of Computational methods in Engineering 13 (1), 91–128.

Rycroft, C., 2009. Voro++: a three-dimensional voronoi cell library in C++.

Sachtleber, M., Zhao, Z., Raabe, D., 2002. Experimental investigation of plastic grain interaction. Materials Science and Engineering: A 336 (1-2), 81–87.

Sai, K., Cailletaud, G., 2007. Multi–mechanism models for the description of ratchetting: Effect of the scale transition rule and of the coupling between hardening variables. International Journal of Plasticity 23 (9), 1589 – 1617.

Schwartz, J., Fandeur, O., Rey, C., 2013. Numerical approach of cyclic behaviour of 316LN stainless steel based on a polycrystal modelling including strain gradients. International Journal of Fatigue 55, 202 – 212.

Shantsev, D. V., Jaysaval, P., de la Kethulle de Ryhove, S., Amestoy, P. R., Buttari, A., L'Excellent, J.-Y., Mary, T., 2017. Large-scale 3-D EM modelling with a Block Low–Rank multifrontal direct solver. Geophysical Journal International 209 (3), 1558–1571.

Shenoy, M., Tjiptowidjojo, Y., McDowell, D., 2008. Microstructure–sensitive modeling of polycrystalline IN 100. International Journal of Plasticity 24 (10), 1694 – 1730, special Issue in Honor of Jean-Louis Chaboche.

Shenoy, M., ZHANG, J., McDOWELL, D., 2007. Estimating fatigue sensitivity to polycrystalline Ni-base superalloy microstructures using a computational approach. Fatigue & Fracture of Engineering Materials & Structures 30 (10), 889–904.

Sinha, S., Ghosh, S., 2006. Modeling cyclic ratcheting based fatigue life of HSLA steels using crystal plasticity FEM simulations and experiments. International Journal of Fatigue 28 (12), 1690 – 1704.

Sirovich, L., 1987. Turbulence and the dynamics of coherent structures part III: Dynamics and scaling. Quarterly of Applied Mathematics 45 (3), 583–590.

Siska, F., Forest, S., Gumbsch, P., 2007. Simulations of stress–strain heterogeneities in copper thin films: Texture and substrate effects. Computational Materials Science 39 (1), 137 – 141.

Slaughter, W. S., 2002. The linearized theory of elasticity. Birkhauser.

Smith, B., Shih, D., McDowell, D., 2018. Cyclic plasticity experiments and polycrystal plasticity modeling of three distinct Ti alloy microstructures. International Journal of Plasticity 101, 1 – 23.

Soutis, C., Beaumont, P. W., 2005. Multi–scale modelling of composite material systems: the art of predictive damage modelling. Elsevier.

Stein, C. A., Cerrone, A., Ozturk, T., Lee, S., Kenesei, P., Tucker, H., Pokharel, R., Lind, J., Hefferan, C., Suter, R. M., Ingraffea, A. R., Rollett, A. D., 2014. Fatigue crack initiation, slip localization and twin boundaries in a nickel–based superalloy. Current Opinion in Solid State and Materials Science 18 (4), 244 – 252.

Stinville, J., Echlin, M., Texier, D., Bridier, F., Bocher, P., Pollock, T., 2016. Sub–grain scale digital image correlation by electron microscopy for polycrystalline materials during elastic and plastic deformation. Experimental Mechanics 56 (2), 197–216.

Sun, F., Meade, E. D., O'Dowd, N. P., 2018. Microscale modelling of the deformation of a martensitic steel using the Voronoi tessellation method. Journal of the Mechanics and Physics of Solids 113, 35 – 55.

Taleb, L., Keller, C., 2018. Experimental contribution for better understanding of ratcheting in 304l ss. International Journal of Mechanical Sciences 146-147, 527 – 535.

Tresca, H. E., 1864. Sur l'écoulement des corps solides soumis à de fortes pressions. Imprimerie de Gauthier-Villars, successeur de Mallet-Bachelier, rue de Seine ….

Vince, A., 2002. A framework for the greedy algorithm. Discrete Applied Mathematics 121 (1-3), 247–260.

Walley, J. L., Wheeler, R., Uchic, M. D., Mills, M. J., 2012. In–Situ mechanical testing for characterizing strain localization during deformation at elevated temperatures. Experimental Mechanics 52 (4), 405–416.

Wang, Y., Raabe, D., Klüber, C., Roters, F., 2004. Orientation dependence of nanoindentation pile–up patterns and of nanoindentation microtextures in copper single crystals. Acta materialia 52 (8), 2229–2238.

Wehner, T., Fatemi, A., 1991. Effects of mean stress on fatigue behaviour of a hardened carbon steel. International Journal of Fatigue 13 (3), 241–248.

Xia, Z., Kujawski, D., Ellyin, F., 1996. Effect of mean stress and ratcheting strain on fatigue life of steel. International Journal of Fatigue 18 (5), 335 – 341.

Xie, C. L., Ghosh, S., Groeber, M., 2004. Modeling cyclic deformation of HSLA steels using crystal plasticity. Journal of Engineering Materials and Technology 126, 4.

Yagawa, G., Shioya, R., 1993. Parallel finite elements on a massively parallel computer with domain decomposition. Computing Systems in Engineering 4 (4), 495 – 503, parallel Computational Methods for Large-Scale Structural Analysis and Design.

Yu, C., Kang, G., Kan, Q., Song, D., 2013. A micromechanical constitutive model based on crystal plasticity for thermo-mechanical cyclic deformation of NiTi shape memory alloys. International Journal of Plasticity 44, 161 – 191.

Yuan, X., Yu, W., Fu, S., Yu, D., Chen, X., 2016. Effect of mean stress and ratcheting strain on the low cycle fatigue behavior of a wrought 316LN stainless steel. Materials Science and Engineering: A 677, 193 – 202.

Yvonnet, J., He, Q.-C., 2007. The reduced model multiscale method (R3M) for the non-linear homogenization of hyperelastic media at finite strains. Journal of Computational Physics 223 (1), 341 – 368.

Z–set package, 2013. Non-linear material & structure analysis suite, www.zset-software.com.

Zaafarani, N., Raabe, D., Singh, R., Roters, F., Zaefferer, S., 2006. Three-dimensional investigation of the texture and microstructure below a nanoindent in a Cu single crystal using 3D EBSD and crystal plasticity finite element simulations. Acta Materialia 54 (7), 1863 – 1876.

Zecevic, M., Knezevic, M., 2018. Latent hardening within the elasto–plastic self–consistent polycrystal homogenization to enable the prediction of anisotropy of AA6022-T4 sheets. International Journal of Plasticity 105, 141 – 163.

Zecevic, M., Korkolis, Y. P., Kuwabara, T., Knezevic, M., 2016. Dual–phase steel sheets under cyclic tension–compression to large strains: Experiments and crystal plasticity modeling. Journal of the Mechanics and Physics of Solids 96, 65 – 87.

Zhang, H., Diehl, M., Roters, F., Raabe, D., 2016. A virtual laboratory using high resolution crystal plasticity simulations to determine the initial yield surface for sheet metal forming operations. International Journal of Plasticity 80, 111 – 138.

Zhang, K.-S., Ju, J. W., Li, Z., Bai, Y.-L., Brocks, W., 2015. Micromechanics based fatigue life prediction of a polycrystalline metal applying crystal plasticity. Mechanics of Materials 85, 16 – 37.

Zhang, M., Neu, R., McDowell, D., 2009. Microstructure-sensitive modeling: Application to fretting contacts. International Journal of Fatigue 31 (8), 1397 – 1406.

Zhang, M., Zhang, J., McDowell, D., 2007. Microstructure-based crystal plasticity modeling of cyclic deformation of Ti-6Al-4V. International Journal of Plasticity 23 (8), 1328 – 1348.

Zhang, Z., Thaulow, C., Ødegård, J., 2000. A complete Gurson model approach for ductile fracture. Engineering Fracture Mechanics 67 (2), 155 – 168.

Zhao, Z., Ramesh, M., Raabe, D., Cuitiño, A., Radovitzky, R., 2008. Investigation of three-dimensional aspects of grain-scale plastic surface deformation of an aluminum oligocrystal. International Journal of Plasticity 24 (12), 2278 – 2297.

RÉSUMÉ

Le domaine de la mécanique, en particulier de la micromécanique, a connu de grands développements. Il est bien connu que l'écoulement plastique dans un monocristal est anisotrope, ce qui peut être modélisé à l'aide de lois de comportement phénoménologiques à l'échelle moyenne. Le développement de lois micromécaniques a pour objectif de relier le comportement de chaque grain, de prédire l'évolution de la plasticité et, à son tour, de rendre compte des propriétés macroscopiques de la structure.
Cette thèse a porté sur deux problèmes physiques, à savoir le comportement des matériaux soumis à un chargement asymétrique dans des conditions limites fondées soit sur des contraintes cycliques soit sur des déplacements cycliques. Ces chargements entraînent une accumulation de contrainte supplémentaire ou une relaxation de contrainte moyenne à l'échelle macroscopique. Les modèles numériques conventionnels donnent un excès des deux quantités. Dans ce travail, il est montré qu'une approche par éléments finis de plasticité cristalline de mésoéchelle peut répondre à ces deux problèmes. Différents états mécaniques existant dans des structures chargées cycliquement sont examinés et une interprétation micromécanique est donnée concernant leur comportement macroscopique caractéristique. Les résultats statistiques de différentes quantités constitutives au sein d'un polycristal sont également analysés, ce qui permet de mieux comprendre ce qui se passe au niveau local.
L'autre partie de la thèse concerne le traitement de données volumineuses dans le domaine de la science des matériaux informatique. Tout en résolvant des problèmes d'éléments finis à grande échelle, de grandes quantités de ressources de calcul sont utilisées et souvent les résultats au cours du temps sont ignorés après les études et ne sont utilisés pour les prévisions futures. Dans ce travail, il est montré qu'en utilisant des données déjà générées, de nouveaux cas de test peuvent être prédits à partir de simulations précédentes. La méthode utilisée est appelée hyper-réduction hybride. Elle utilise un protocole d'apprentissage automatique non supervisé associé à la technique gappy POD pour exécuter des simulations aux éléments finis réduits. Ces simulations réduites aident à capturer les valeurs extrêmes de plasticité. Des résultats de fatigue à faible nombre de cycles dans un superalliage à base de fer et de nickel (Inconel 718) sont utilisés comme test.

MOTS CLÉS

Plasticité cristalline, réduction de modèles, méthode des éléments finis, élément de volume représentatif, étude statistique, séparabilité des échelles

ABSTRACT

The field of mechanics, particularly micromechanics, has undergone great developments. It is well known that plastic flow in a single crystal is anisotropic which may be modeled using phenomenological constitutive laws at the mesoscale. The idea behind the development of micromechanical laws is to relate the behavior of each individual element of the geometry, predict evolving plasticity, and in turn account for the macroscopic properties of the structure.
Two physical problems have been considered is this thesis i.e. the behavior of materials when they are asymmetrically loaded under cyclic stress or strain based boundary conditions. These loadings cause incremental strain accumulation or mean stress relaxation at the macroscopic scale. Conventional numerical models give an excess of both quantities. In this work it is shown that a mesoscale crystal plasticity finite element approach can give an answer to both problems. Different mechanical states existing in cyclically loaded structures are scrutinized and a micromechanical interpretation is given about their characteristic macroscopic behavior. Statistical results of different constitutive quantities within a polycrystal are also analyzed which give a new insight into what is happening at a local level.
The other part of the thesis pertains to big data problems in computational materials science. While solving large scale finite element problems, vast amounts of computational resources are utilized and many a times the evolving results are discarded after studying; not using them for future predictions. In this work it is shown that by utilizing already generated data, new test cases may be predicted from previous simulations. The method employed is called hybrid hyper-reduction which uses an unsupervised machine learning protocol coupled with the gappy proper orthogonal decomposition technique to run reduced finite element simulations. These reduced simulations help in capturing extreme values of plasticity which are critical for component lifetime assessment. Low cycle fatigue in a nickel iron based super alloy (Inconel 718) is taken as a test case.

KEYWORDS

Crystal Plasticity, model order reduction, finite element method, representative volume elements, statistical study, separability of scales